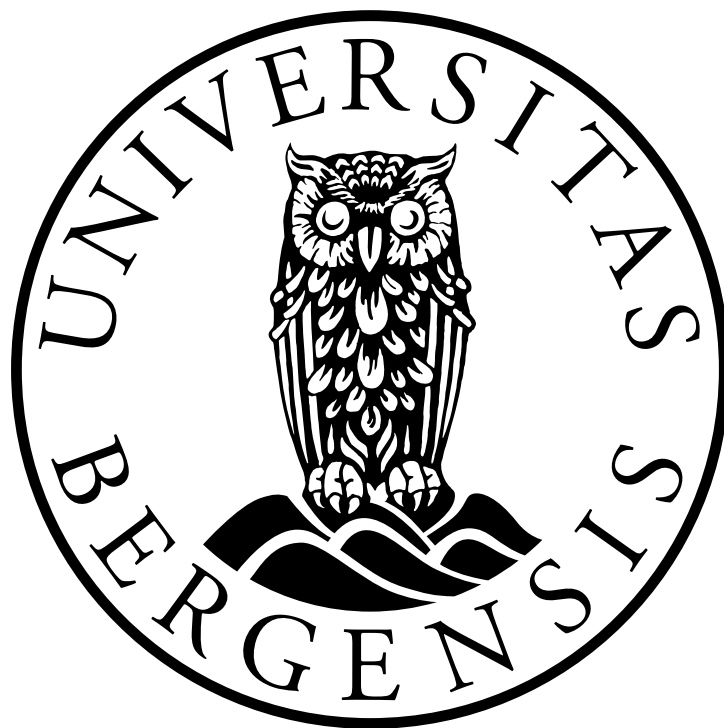# A Numerical and Experimental Study of the Dispersion of a Dust Layer by a Rarefaction Wave

Sindre Brugrand Hauge

June 1, 2017

A thesis in partial fulfilment of the requirements for the degree of *Master of Science* in the subject of Process Technology.

Acknowledgements

I would like to thank Prof. Pawel Kosinski, for being an excellent supervisor and for providing me the opportunity to work on this thesis. It has been a challenging, but exciting year.

I would also like to thank my co-supervisor, Dr. Boris Balakin, for answering questions regarding the CFD software STAR-CCM+ and providing feedback on my work.

Thanks to Charles Sebastiampillai, Roald Langøen and Werner Olsen for construction and assembly of the pressure chambers used in the experiments, and a shout-out to Wulme Dery for teaching me how to use the high-speed camera.

A big thank you to my fellow students at the university for enriching academic discussions, intense foosball games and great companionship. In the words of the late, great Dewey Cox, "It's a beautiful ride".

To my family, thank you for providing love and support for as long as I can remember.

Bergen, June 2017

Sindre Brugrand Hauge

Abstract

In recent years, dynamics of dust lifting behind a passing shock wave have been studied extensively. Few studies have focused on the problem of dust lifting by a rarefaction wave. The aim of this study was to create a three-dimensional CFD model of previously conducted experiments. A second goal was to conduct own experiments of rarefaction wave-dust interaction and try to model these using CFD.

The Eulerian-Eulerian approach was selected as the modelling technique with two different energy models studied; the segregated fluid temperature model and the segregated fluid isothermal model. The former provided a solution by solving the energy equation, while the latter kept a constant energy field. The results from the simulations were compared to results obtained using an exact Riemann solver, previous experiments and previous simulations. A "smearing" of the head and tale of the waves was observed. Other than this, the simulation solving for the energy equation was in compliance with both the Riemann solution and previous experiments. The consequence of solving using the segregated fluid isothermal model was a too low speed of propagation of the rarefaction-, contact- and shock wave and ultimately a higher air velocity behind the rarefaction wave, which in turn led to a greater dust dispersion.

Additionally, a simulation with a closed end geometry was run to investigate the effect of the reflected shock wave. The results indicated that the reflected shock wave and its accompanying flow of gas have a suppressing effect on dust dispersion caused by rarefaction waves.

As a second part of the thesis experiments with a rarefaction wave interacting with a layer of particles were recorded with a high speed camera in two pressure chambers with different diameter using a solenoid valve to initiate depressurization. The particle layer showed similarities to a fluidized particle bed when exposed to the rarefaction wave. After the rarefaction wave arrived at the particle bed, the bed expanded upwards with visible bubbles forming and expanding inside, eventually breaking through the top of the bed and spouting dust further up the chamber. The height at which the bubbles broke through the particle bed surface was defined as breakthrough height. The breakthrough height was shown to increase with smaller pressure chamber diameter, smaller particle diameter and, at times, increasing pressure. A combination of smaller particle diameter, smaller pressure chamber diameter and higher initial pressure gave the highest amount of particle dispersion following the breakthrough.

Contents

1 Introduction

Many dusts that are handled in the modern industry are made out of flammable material which, when ejected into air, could form an explosive atmosphere. Examples of such materials are aluminium, magnesium, wood, grain, pharmaceuticals, plastics and coal [6]. Corn starch is a popular material used not only for cooking, but also offers a variety of uses across various industries, including being used to manufacture bioplastics and acting as a anti-stick agent on medical products. Despite being such a popular and applicable material, corn starch is highly flammable when dispersed into the air. On June 27 2015 a coloured powder was used as a party effect at a colour festival in a water park in Taiwan [12]. People were standing "ankle-deep" in a powder that was repeatedly suspended into the air using compressed air. The cloud created from this suspension eventually ignited and a deflagration occured injuring 497 people and killing 15. The powder was later identified as corn starch.

Some of the biggest mining accidents in history were caused by dust explosions. Because of the brittle nature of coal, dust can be created from mining, transportation or handling of coal. The accidents were usually initiated by flammable gases found in coal mines that ignited and produced shock waves, which in turn dispersed coal dust from the floor into explosive atmospheres.

The problem of dust lifting by a shockwave propagating over a layer of dust deposits is of considerable interest both in theory and in practice. The practical significance is caused by the fact that the initiation of dust lifting is the first stage in a process that potentially could develop into a dust explosion. The theoretical importance is the possibility of obtaining new information about the mechanisms behind dust lifting that can be used in future research and development. Nevertheless, an equally important problem, perhaps more important because of the lack of knowledge, is the problem of dust dispersion due to a rarefaction wave.

A rarefaction wave is the antithesis of a shockwave [2]. A way to generate a shockwave and a rarefaction wave is by using a shock tube that consists of a high pressure section and a low pressure section separated by a diaphragm.
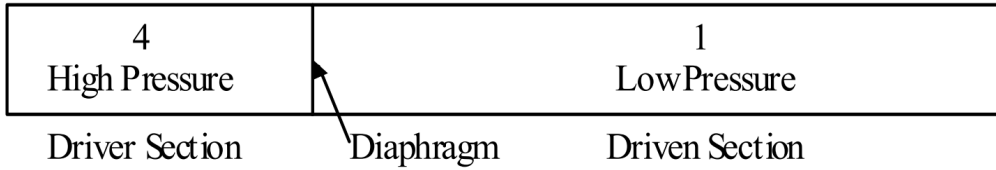
1

Figure 1: Section 4 and 1 shows the initial conditions in the shock tube [18].

When the pressure difference between the two sections becomes sufficiently high, the diaphragm will rupture and the two sections will be forced to equalize at high speeds. This equalization presents itself in the form of a shockwave propagating through the low pressure section and a rarefaction wave, or decompression wave, propagating through the high pressure section. The interface between the gas in the driver section and the driven section is called the contact surface, or contact discontinuity.
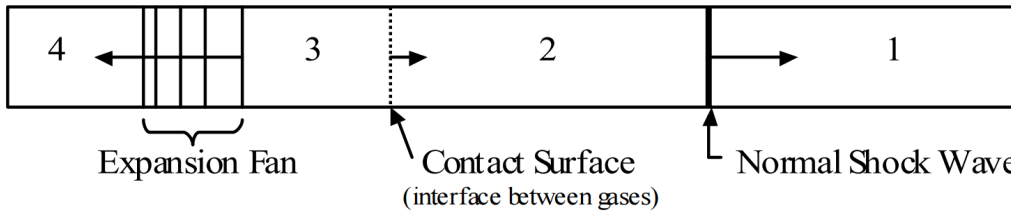

Figure 2: After the rupture of the diaphragm, the shock tube is divided into four sections [18].

As the shockwave propagates through region 2 (Figure 2), it increases the pressure and velocity behind it to the same level as in region 3. Region 2 will, because of the increase in pressure, experience an increase in temperature and density. Based on this we can say that across the contact surface the entropy and the density changes, while the pressure and velocity are preserved.

While the shockwave is a very thin region (in the order of 10^{-5} cm for air at standard conditions [2]), the rarefaction wave, or decompression wave, appear as an expanding fan, and is therefore also known as an expansion fan.

The interaction between the shock wave and a layer of dust in region 1 has been subject for numerous studies ([9], [26], [8]). The scenario of interaction between the rarefaction wave and dust in region 4, on the other hand, has

not received as much attention. Still, some experiments ([19]) and some simulations ([13], [25]) have been carried out. These simulations are one- or two dimensional. Three dimensional studies of dust layer-rarefaction wave interaction are few or non-existing. One of the goals of this thesis was therefore to recreate experiments conducted by Medvedev et al. in [19] using a computational fluid dynamics (CFD) software called STAR-CCM+. The simulations were first, for verification, run and compared to the results obtained from an exact Riemann solver. The simulations were three-dimensional and the results were compared to the work done by Medvedev et al. [19] and Klemens et al. in [13].

The computational time, or the amount of time that passes for a computer to finish its task, for a problem like this should be kept to a minimum without compromising the quality of the results too much. A simplification that could lead to a shorter computational time was investigated, and its effect on the results was studied.

As a second part of the thesis a series of experiments with dust-rarefaction wave interaction were conducted. The purpose of this was, in addition to theory and computational work, to observe the nature of the phenomena. The experiments were recorded with a high speed camera and studied afterwards.

An attempt to create a model of the experimental setup in STAR-CCM+ was also made.

2 Literature survey

Gerrard [11] studied photographically the mechanisms of dust dispersion during the first hundred microseconds after the passage of a shock wave in air over a dust deposit on a horizontal surface. He reported a short delay, depending on the depth of the dust layer, between the passing of a shock wave and the raising of dust at that point. Gerrard argued that this dependence on the depth indicated that the initial dispersion was connected with the shock wave reflected from the base of the dust returning to the surface of the deposits. Fletcher [9] investigated in 1975, as Gerrard suggested, the possibility that dust could be raised from a deposit over which a shock wave passed by the reflection of a pressure waves from the underlying surface. The experiments was showing that, instead of the reflecting waves, the dust was raised as a result of the rapid flow behind the shock wave.

Medvedev et al. [19] conducted experiments with a 2.6 m long shock tube to investigate the initial stage of dust layer dispersion by a short duration flow generated by a rarefaction wave. The tube consisted of two pressure chambers, high and low, with a membrane separating them. The tube had a cross-sectional area of 28x56 mm with a 26x52 mm dust container in the end. Experiments with three different high pressure chamber (HPC) lengths, 1.57 m, 2.07 m and 2.57 m, combined with low pressure chamber (LPC) lengths of 1.03 m, 0.53 m and 0.03 m (giving a total length of 2.6 m in each experiment), were conducted. The initial pressure, the depth of the dust layer and, as mentioned, the length of the sections were varied in the experiments. The experiments showed that even weak rarefaction disturbances dispersed a dust layer effectively. The velocity of dust lifting was rising with increasing layer depth, with a maximum for 50 mm. By keeping the height constant at 50 mm and varying the other variables, it was found that the dynamics of the dust lifting depends mainly on the amplitudes of the waves and almost not on the durations.

Klemens et al. [13] performed one-dimensional mathematical modelling of dust layer dispersion due to rarefaction waves. The geometry consisted of a tube of length 2.6 m with a high-pressure section of length 2.1 m containing a 50 mm thick dust layer located at the end. The main objective of the computation was to compare the results with what was obtained by Medvedev et al. [19]. They found a quantitative difference between the numerical simulation and the experiment. The most important reason was that the model used did not describe flow in dust mixtures of high concentration very well. In addition to this, the assumption that it was a one-dimensional problem,

4

when in reality it was three-dimensional, might have caused the differences. Despite this the results was qualitatively and physically correct, so the model may be used for applications were exact data are not needed.

Zhilin et al. [25] investigated interaction of a rarefaction wave with a layer of solid particles near the end face of a shock tube. The task was to determine the flow pattern in the shock tube at subsequent times ($T > 0$) and the mechanism of rarefaction wave interaction with a layer of solid particles in the presence of a rigid boundary. One-dimensional simulations were performed and compared to experiments by Medvedev et al. [19]. As in [19], the total length of tube was 2.6 meter with HPC varying between 1.570 m, 2.070 m and 2.570 m. Zhilin et al. approximated the volume fraction of particles used Medvedev et al. to be 0.5, and used this for their research.
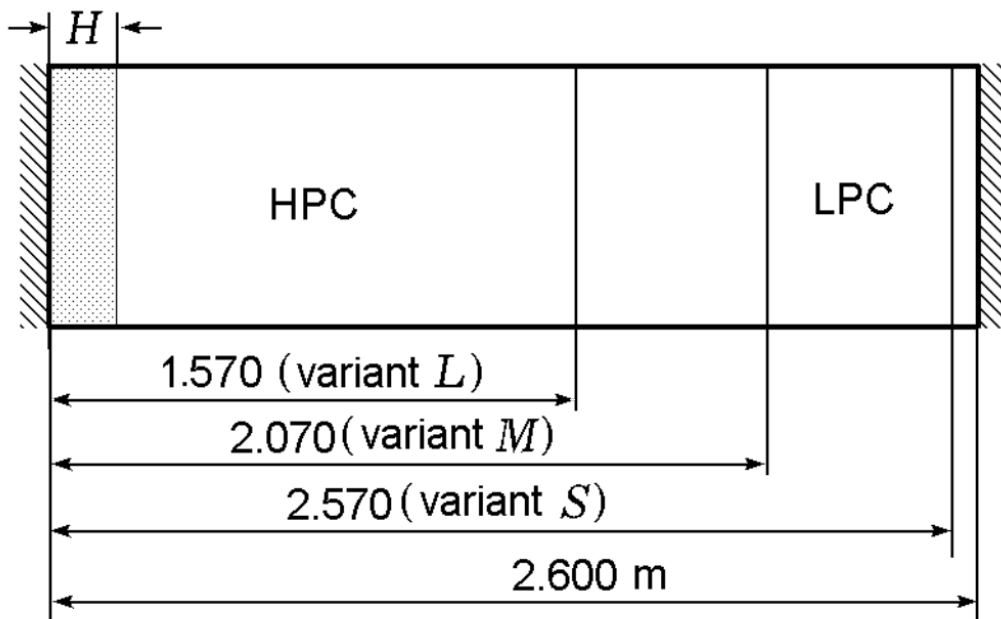

Figure 3: Formulation of the problem by Zhilin et al. [25] H denotes the height of the dust layer.

For the dynamics of lifting of the layer, after comparing with [19], Zhilin et al. concluded that the initial stage of lifting is adequately described by the proposed theory. The model underestimates to some extent the second stage of lifting. The velocity of lifting of the layer versus the initial pressure difference in the HPC and the LPC was investigated and compared to the

5

two series of experiments and theoretical estimates done by Medvedev et al. [19]. The results calculated by the proposed model were seen to be consistent with experimental data.

Utkilen et al. [22] investigated dust lifting behind a moving pressure wave using the Eulerian-Eulerian approach. One of the goals was to provide data for dust layers with high volume fractions, since few previous studies had focused on this. Four simulations varying the initial pressure and volume fraction of the dust were performed. Pressure varied between 4 and 8 bar, while the volume fraction varied between 0.4 and 0.6. It was found that a combination of high pressure and high volume fraction led to the greatest dispersion of dust. In addition to this, investigations of drag-force models and particle-particle interaction models were conducted. Two different drag-force models were compared: the Schiller-Naumann and the Gidaspow. The Schiller-Naumann model was found to underestimate the drag in the diluted parts of the layer, and hence led to a lower lifting than the Gidaspow model. The results indicated that lifting due to particle-particle interaction was neglectable compared to the lifting from fluid-particle interaction.

Fan et al. [8] investigated the interaction of a planar shock wave with a loose bulky layer both experimentally and numerically. A flowfield of gas and granular phases was visualized by means of shadowgraphs and pulsed x-ray shadowgraphs with traced particles. The numerical results was in good agreement with the measured results, and the dense two-phase model developed by Gidaspow proved to be valid for the description of the interaction of a shock wave with a dusty particle layer.

Zydak et al. [26] simulated two-phase flows in large geometries using the Eulerian-Eulerian approach. A model of dust lifting behind a propagating shock wave has previously been developed. Three improvements of the model were studied: Saffman force, Magnus force and particles collisions. The addition of Saffman force and Magnus force did not improve the model, as high values of the empirical constants had to be used to notice any influence. If the model of particle collisions was used, the results were improved, especially with regards to the shape of the dust cloud, comparing to those obtained without any of the studied models. The increase in shock wave velocity and dust layer height led to an increase in the vertical velocity of the dust, but overall the vertical velocity of the dust was to high when compared to experimental results.

Klemens et al. [14] investigated experimentally the process of dust lifting

from a layer. The delay in lifting the dust after the shockwave had passed and the vertical velocity of the lifted dust was calculated from concentration measurements. The results confirmed that the dust lifting process is observed at some distance behind the shock wave, which means that it is the flow behind the shockwave that causes the process of dust lifting. As in the simulations done by Zydak et al. [26], the vertical velocity of dust was increasing with increasing dust layer thickness and shock wave velocity. This was the case especially near the layer, but at greater heights above the layer this did not apply equally. The velocity of the lifted dust at each experiment usually increased as the dust was moving out, but finally decreased as the dust approached the upper part of the channel.

3 Fluid dynamics

Fluid dynamics is the branch of physics and engineering that describes the flow of liquids and gasses.

3.1 The governing equations of fluid dynamics

All the problems encountered in fluid dynamics are solved using three laws. These laws are the mathematical statements of three fundamental physical principles [5]; The conservation of mass results in the continuity equation, Newton's second law is used to obtain the momentum equation and the conservation of energy yields the energy equation.

The three equations can be portrayed in four ways, depending on which model the equations are derived from. They can be in integral form and either conservation form or nonconervation form, or they can be in differential form and either conservation form or nonconservation form. What form the equations take depends on what model of flow they are derived from. There are four models:

- Finite control volume fixed in space with the fluid moving through it.

- Finite control volume moving with the fluid such that the same fluid particles are always in the same control volume.

- Infinitesimal fluid element fixed in space with the fluid moving through it.

- Infinitesimal fluid element moving along a streamline with the velocity equal to the local flow velocity at each point.

An equation on integral form is derived on the basis of a finite control volume. If the control volume is fixed in space, it leads to a specific integral form, which is called conservation form. The forms of the governing flow equations that are directly obtained from a flow model, which is fixed in space are, by definition, called the conservation form.

If the equation is in a partial differential equation form, it is derived on the basis of an infinitesimally small element. The forms of the governing flow equations that are directly obtained from a flow model, which is moving with the flow are, by definition, called the nonconservation form [5].

Continuity equation

By applying the physical principle of conservation of mass on any of the four models of flow listed in the previous section, the continuity equation is obtained [5]. This equation is a representation of the physical principle of conservation of mass.

Momentum equation

The momentum equation is obtained by applying another fundamental principle to a model of flow. By applying Newton's second law $\vec{F} = m\vec{a}$ to for instance an infinitesimally small fluid element moving with the flow, the momentum equation on nonconservation form is obtained [5]. There are two sources of force acting in this equation

- Body forces act directly on the volumetric mass of the fluid element. Examples are gravitational, electric and magnetic forces.

- Surface forces act directly on the surface of the fluid element. These forces are due to two things:

  - The pressure acting on the surface by the fluid surrounding the fluid element.
  - The shear and normal stress distributions acting, by means of friction, on the surface from the fluid surrounding the fluid element.

When this operation is done in the x, y and z directions, a set of equations called the Navier-Stokes Equations are obtained. However, in modern CFD-litterature, the terminology Navier-Stokes equations has been expanded to include the entire system of flow equations for the solution of a viscous flow, the continuity and momentum, as well as the energy equation [5].

Energy equation

The third physical principle mentioned in Section 3.1 is the conservation of energy. This physical principle is in fact the first law of thermodynamics, and when applied to the flow model of a fluid element moving with the flow, the first law states that:

$$
\begin{array}{llll}
\text{Rate of change} & \text{Net flux of} & \text{Rate of work done on} & \\
\text{of energy inside} & = \text{heat into} & + \text{element due to} & (1) \\
\text{fluid element} & \text{element} & \text{body and surface forces} &
\end{array}
$$

Filling in for the terms above the end result is the final form of the energy equation.

3.2 Boundary conditions

The governing equations of fluid dynamics are the same for flows in different systems. Despite this the flow fields are quite different. This is due to boundary conditions. The boundary conditions dictate the particular solutions obtained from the governing equations [5]. For a viscous flow the boundary conditions on a surface assumes zero relative velocity between the surface and the gas immediately next to the surface. This is known as the no-slip condition. At a stationary surface with a flow moving past it, the velocity at the surface is

$$u = v = w = 0. \tag{2}$$

In theory, the cross-section of a turbulent stream consists of three layers. The viscous sublayer, the buffer layer and the turbulent core [17]. Right next to the wall, there is a thin volume where the velocity gradient is essentially constant and the flow is viscous most of the time. This is the viscous sublayer. Here, eddy diffusion is minor, and only viscous shear is important. Immediately next to the viscous sublayer there exists a transition layer called the buffer layer. This is, like the viscous sublayer, very thin. The majority of the cross-section is occupied by the turbulent core, where viscous shear is negligible in comparison with that from the eddy viscosity.

Expression of the velocity distribution in turbulent flow is done in terms of dimensionless parameters by the following equations:

$$u^* \equiv \bar{V}\sqrt{\frac{f}{2}} = \sqrt{\frac{\tau_W}{\rho}}, \tag{3}$$

$$u^+ \equiv \frac{u}{u^*}, \tag{4}$$

$$y^+ \equiv \frac{yu^*\rho}{\mu} = \frac{y}{\mu}\sqrt{\tau_w\rho}. \tag{5}$$

Where u^* is the friction velocity, u^+ is the dimensionless velocity quotient, y^+ is dimensionless distance and y is distance from wall of tube. τ_W is the wall shear stress and ρ is the density of the fluid. The relationship between y, r and r_w, the radius of the tube, is

$$r_w = r + y. \tag{6}$$

The ranges for the different layers described are

$$\text{The viscous sublayer: } y^+ < 5$$
$$\text{The buffer zone: } 5 < y^+ < 30$$
$$\text{The turbulent core: } 30 < y^+$$

3.3   Multiphase flow

The flow of multicomponent, multiphase mixtures covers a wide spectrum of flow conditions and applications. A component is a chemical species such as nitrogen, oxygen or water [4]. A phase refers to the thermodynamical state of the matter, like solid, liquid and vapour. In multi-component flow, the different species are mixed at molecular level and have the same convection velocity. In multiphase flow, the different phases are mixed at macroscopic scale and have a different convection velocity. There are two main categories of multiphase flow, dispersed flows and stratified flows [20]. A phase is considered dispersed if it occupies disconnected regions of space, like bubbles, drops or particles. The opposite of a dispersed phase is a continuous phase. Examples of stratified flows are free surface flows and annular film flow in pipes.

In a flow consisting of particles dispersed in a continuous phase of air, there will be particle-fluid interactions. Particle-fluid interactions refers to the exchange of properties between phases and is responsible for coupling in dispersed phase flow [4]. Mass, momentum and energy transfer between phases are the different forms of interaction. There have been a large number of experiments and analyses performed for the transfer of properties, but most studies have been done for isolated particles in uniform flow fields. For a single particle, the conservation equations describes the interactions. In the case of particles in a cloud, it is especially hard to determine drag. Analytical models are challenging because the model has to account for the surface of every particle, and in experimental studies it is difficult to make detailed local measurements of a particle in a cloud. Therefore the drag force is inferred from experiments and measurements done on settled and fluidized beds. Ergun [7] conducted a series of experiments with a particle bed not yet fluidized, and found an expression for the pressure drop through the packed bed. Wen and Yu [24] conducted a series of fluidization experiments to infer the drag force on particles in dense mixtures, and came up with a correlation that is valid for particle volume fractions less than 0.7. These expressions for drag force are used in this thesis, and can be found in Section 4.5.

4 Computational fluid dynamics

As mentioned in Section 3, fluid flows are governed by partial differential equations which represents conservation laws of mass, momentum and energy. In short, Computational fluid dynamics (CFD) is the replacement of the partial differential equations by a set of algebraic equations which can be solved using computers. When using CFD, scientists and engineers are able to obtain a prediction of how fluid will flow in different scenarios. Meteorologists use CFD to forecast the weather and warn of natural disasters, car-designers use CFD to minimize drag force and hence the fuel consumption, and if you happen to be a race car driver CFD is most likely used to find just the right balance between drag force for top speed and down force to give you grip when cutting corners. In other words, no matter what you do or where you go in life, you are likely to encounter some sort of fluid flow problem. From the air you breath to the air driving the wind-turbines powering you iPhone-charger. In this thesis CFD is used through a software called STAR-CCM+, allowing the author to conduct numerical analyses of the previously described problem.

4.1 Discretization

STAR-CCM+ uses discretization methods to convert the continuous system of equations to a set of discrete algebraic equations. Depending on the mathematical model, STAR-CCM+ discretizes the continuous equations using either the finite volume method or the finite element method [20]. For the solution of Newtonian fluid flow, multiphase flow and heat transfer, the finite volume method is applied. Generally the methods follow a common procedure of first to divide the continuous domain into a finite number of subdomains. Second, the unknowns are stored at specific locations of the mesh, like vertices, cell centroids, face centroids or edges. Lastly, the integral or differential equations are employed for discretization in space and time. The result is a coupled system of algebraic equations that needs to be solved at each time-step.

4.2 Grid/Mesh

The mesh is the domain we are looking at divided into a "mesh" of subdomains. In each and every one of these subdomains, or cells, the discretized governing equations are solved. When a domain is divided into this ensemble of subdomains, it resembles a wire mesh (for two-dimensional analyses), hence the name.

4.3 Modelling multiphase flow

STAR-CCM+ provides several ways to model the two categories (dispersed and stratified) of multiphase flow described in Section 3.3. This thesis is investigating particles moving through air, namely dispersed flow. There are two main approaches in modelling this kind of multiphase flow [20]. The Eulerian-Lagrangian (E-L) approach and the Eulerian-Eulerian (E-E) approach. The difference is how the dispersed phase is treated. The E-L approach treats each particle individually. Every single particle is assigned its own set of equations so that the model can track them through space and time. This makes the E-L approach a very accurate tool when modelling this kind of multiphase flow.

Single phase flow problems are solved using the conservation equations. The E-E approach is basically an extension of this. It treats the particle cloud, as well as the air, as continuous fluids and develops equations for the conservation of mass, momentum and energy for each phase. By discretizing these into algebraic equations they can be solved for each cell in the domain.

The E-E approach is normally the best alternative for dispersed particle problems, especially when the dust cloud becomes so dense that it is hard to single out the particles. If the E-L approach is applied in cases like this, the solving of equations for each particle would lead to a very long calculation time.

A weakness of the E-E model is the lack of internal particle to particle interactions. Because of the frequent particle collisions in dense clouds, the E-L would have been desirable if it hadn't been for the calculation time. However, development of the E-E approach has made it possible to include models for particle-particle interactions.

4.4 Governing equations

The governing equations for the E-E approach are presented below. They are based on the STAR-CCM+ methodology [20].

Continuity equation

For a generic phase i:

$$\frac{\partial}{\partial t}(\alpha_i \rho_i) + \nabla(\alpha_i \rho_i \boldsymbol{v}_i) = 0, \tag{7}$$

where a_i is the volume fraction and $\boldsymbol{v}_i$ is the mean phase velocity. The volume fractions must satisfy the equation:

$$\sum_i \alpha_i = 1. \tag{8}$$

Momentum equation

$$\frac{\partial}{\partial t}(\alpha_i \rho_i \boldsymbol{v}_i) + \nabla \cdot (\alpha_i \rho_i \boldsymbol{v}_i \mathbf{v}_i) = -\alpha_i \nabla p + \alpha_i \rho_i g + \nabla \cdot [\alpha_i(\tau_i + \tau_i^t)] + M_i + (F_{int})_i, \tag{9}$$

where τ_i and τ_i^t are molecular and turbulent stresses, p is pressure (assumed to be equal for both phases), $(\boldsymbol{F}_{int})_i$ represents internal forces (such as the solid pressure force between particles in Section 4.6) and $\boldsymbol{M}_i$ is the interphase momentum transfer per unit volume (such as the drag force in Section 4.5). The interphase momentum transfer represents the sum of all the forces the phases exert on one another and satisfies the equation:

$$\sum_i \boldsymbol{M}_i = 0. \tag{10}$$

Energy equation

For an Eulerian phase i, the energy is conserved according to the following equation [20]:

$$\frac{\partial}{\partial t}((\alpha_i \rho_i E_i) + \nabla \cdot [\alpha_i \rho_i H_i(\boldsymbol{v}_i - \boldsymbol{v}_g)] + \nabla \cdot \alpha_i \boldsymbol{v}_g p = \nabla \cdot (\alpha_i(k_i + \frac{\mu_i^t C_{p,i}}{\sigma_i^t})\nabla T_i)$$
$$+ \nabla \cdot (\boldsymbol{T}_i \cdot \boldsymbol{v}_i) + \boldsymbol{f}_i \cdot \boldsymbol{v}_i. \tag{11}$$

Here, E_i is the total energy, H_i is the enthalpy, $\mathbf{T}_i$ is the viscous stress tensor, k_i is the thermal conductivity, $C_{p,i}$ is the specific heat, σ_i^t is the turbulent thermal diffusion Prandtl number, T_i is the temperature, $\boldsymbol{f}_i$ is the body force vector and $\boldsymbol{v}_g$ is the grid velocity.

Turbulence

Turbulent flow is the state of fluid motion that is characterized by apperent random chatotic changes in pressure and flow velocity [1]. It has, in contrast to laminar flow, a high Reynolds number (see Section 4.5). The Reynolds-averaged Navier-Stokes (RANS) equations are equations used to describe turbulent flows. To obtain the RANS equations, each solution variable in the instantaneous Navier-Stokes equations (Equation (7), Equation (9) and Equation (11)) is decomposed into its averaged value and its fluctuating component. When splitting the Navier-Stokes equations into an averaging and a fluctuating part, a stress term will appear when averaging the equations. This is a tensor quantity known as the Reynolds stress tensor, $\mathbf{T}_t$, which is the component of the total stress tensor that accounts for the turbulent fluctuations. By modelling this in terms of mean flow flow quantities, one can bring closure to the governing equations.

The Reynolds stresses can be computed from several RANS-based turbulence models. Amongst these turbulence models are the linear eddy viscosity models. With the concept of what is called a turbulent eddy viscosity, μ_t, it is possible to model the Reynolds stress tensor as a function of mean flow quantities. The eddy viscosity models in STAR-CCM+ solves additional transport equations to obtain quantities that enables the derivation of the turbulent viscosity μ_t. The two equation model is a common eddy viscosity model used to obtain these quantities. It is actually the most widely used turbulence model in computational fluid dynamics [23]. It includes two extra transport equations in the calculations to represent the turbulent properties of the flow. The most common two-equation model is the K-Epsilon model $(\kappa - \epsilon)$. One equation determines the turbulent kinetic energy, which is represented by κ, and the other equation determines the rate of dissipation of the turbulent kinetic energy, represented by ϵ. For Eulerian multiphase cases the transport equations are:

$$
\begin{aligned}
\frac{d}{dt}\left(\alpha_i \rho_i \kappa_i\right) + \nabla \cdot \left(\alpha_i \rho_i \kappa_i(\boldsymbol{v}_i - \boldsymbol{v}_g)\right) = \nabla \cdot \left[\alpha_i \left(\mu_i + \frac{\mu_i^t}{\sigma_\kappa}\right)\nabla\kappa_i\right] \\
+ \alpha_i \left[f_i^c G_i^\kappa + G_i^b - \rho_i((\epsilon_i - \epsilon_0) + Y_i^M) + S_i^\kappa\right]
\end{aligned}
\tag{12}
$$

15

and

$$
\frac{d}{dt}(\alpha_i \rho_i \epsilon_i) + \nabla \cdot (\alpha_i \rho_i \epsilon_i (\boldsymbol{v}_i - \boldsymbol{v}_g)) = \nabla \cdot \left[\alpha_i \left(\mu_i + \frac{\mu_i^t}{\sigma_\epsilon} \right) \nabla \epsilon_i \right]
$$
$$
+ \alpha_i \left[f_i^c C_{\epsilon_1} S_i^\epsilon + \frac{\epsilon_i}{\kappa_i}(C_{\epsilon_1} C_{\epsilon_3} G_i^b) - \frac{\epsilon_i}{\kappa_i + \sqrt{V \epsilon_i}} C_{\epsilon_2} \rho_i (\epsilon_i - \epsilon_0) + S_i^\epsilon \right].
\tag{13}
$$

As always the subscript i denotes the different phases, $\sigma_\kappa, \sigma_\epsilon$ and C_{ϵ_2} are coefficients depending on which model is used (for realizable K-Epsilon they are 1, 1.2 and 1.9), C_{ϵ_1} is given by $max\left(0.43, \frac{\eta}{5+\eta}\right)$ where $\eta = \frac{S\kappa}{\epsilon}$, α_i is the volume fraction of each phase i and S_i^ϵ and S_i^κ are user-specified turbulence source terms.

Both Equation (12) and Equation (13) contains production terms consisting of G_i^κ, G_i^b, Y_i^M and f_i^c which is, respectively, turbulent production, buoyancy production, compressibility modification and the curvature correction factor. The last one alters the turbulent kinetic energy production term according to local rotation and vorticity rates.

C_{ϵ_3} is a model coefficient that is, by default for the realizable K-Epsilon model, computed from the velocity components parallel and perpendicular to the gravitational vector **g**.

The turbulent viscosity μ_i^t is calculated as:

$$
\mu_i^t = \rho_i C_\mu f_\mu \kappa T_e,
\tag{14}
$$

where C_μ is a coefficient depending on which model is used (for Realizable K-Epsilon it is 0.09), f_μ is a damping function which mimics the decrease of turbulent mixing near walls and $T_e = \frac{k}{\epsilon}$ is the large-eddy time scale.

4.5   Interphase momentum transfer

In STAR-CCM+, the momentum transfer term $\boldsymbol{M}_i$ can include force contributions from drag, virtual mass, lift and turbulent dispersion. In this model the drag force accounts for the inter-phase momentum transfer.

Drag force

According to the STAR-CCM+ user manual [20], the Gidaspow Drag Model is appropriate for solid dispersed-phase applications such as fluidized beds

where particle loadings are high. Most widely used are the Ergun equation for regions with high solid particle concentration and a modified Stokes law for regions of lower concentration:

$$A_{ij}^D = \begin{cases} \frac{150\alpha_d^2\mu_c}{\alpha_c l_{cd}^2} + \frac{1.75\alpha_d\rho_c|v_r|}{l_{cd}} & \alpha_d \geq \alpha_{tr} \\ \frac{3}{4}C_D\frac{\alpha_d\rho_c}{l_{cd}}|v_r|\alpha_c^n & \alpha_d < \alpha_{tr}. \end{cases} \tag{15}$$

Here, α_{tr}, the transition volume fraction, is used for switching between the two formulas. The subscript d is the dispersed phase, and the subscript c is the continuous phase. n is the hindered-settling exponent. The correction factor α_c^n accounts for the hindered settling that arises when inter-particle forces affects the particle velocity. $|v_r|$ is the relative slip velocity between phases. C_D is from the correlation of Schiller and Naumann, and applies for Newtonian fluids. The drag coefficient of spherical, rigid particles is computed from:

$$C_D = \begin{cases} \frac{24}{Re_d}(1 + 0.15Re_d^{0.687}) & 0 < Re_d \geq 1000 \\ 0.44 & Re_d > 1000. \end{cases} \tag{16}$$

Re_d is the Reynolds Number for the dispersed phase and is defined as:

$$Re_d = \frac{\rho_c|v_r|l}{\mu_c}. \tag{17}$$

4.6 Internal forces between particles

Solid pressure force model

The Solid Pressure Force model adds a compaction or "solid pressure" force to the momentum equations of the dispersed particle phase [20]. When the maximum packing limit, $\alpha_{p,max}$, is reached, this force becomes significant. It acts by increasing the repel force between the particles exponentially as they approach each other, and is given by:

$$(\boldsymbol{F}_{int})_i = -\frac{\alpha_i}{\sum_{j=1}^{M}\alpha_{pj}}\left[e^{A(\alpha_{p,max}-\sum_{j=1}^{M}\alpha_{p,j})}\right]\nabla(\sum_{j=1}^{M}\alpha_{p,j}), \tag{18}$$

where $\alpha_{p,j}$ is the volume fracion of the jth particle phase, M is the number of particles and A is the model constant (600 by default). Since it is only one particle phase in this model, the dispersed phase d, Equation (18) becomes:

$$(\boldsymbol{F}_{int})_d = -\left[e^{600(\alpha_{d,max}-\alpha_d)}\right]\nabla\alpha_d. \tag{19}$$

5 Numerical procedure

The simulations performed in this thesis can be divided into three main parts. In the first part verification simulations were performed with the purpose of creating a CFD-model that could be used in the second part that consisted of simulations conducted for comparison with experiments and simulations from literature. The last part is where simulations were done using geometries corresponding to the setup used later in the experimental part of the thesis.

5.1 Geometry

Three different geometries were used in the simulations. Geometry one was a recreation of the experimental setup used by Medvedev et al. [19]. Geometry two and geometry three were recreations of the experiments performed in this thesis. Geometry one (see Figure 4) was a duct with a rectangular cross-section measuring 28 mm x 56 mm with a length of 2.6 m. At the end of the duct there was a shorter duct with a larger cross-sectional area. This box acted as a pressure outlet box and measures (0.12 x 0.08) m^2 x 0.3 m.
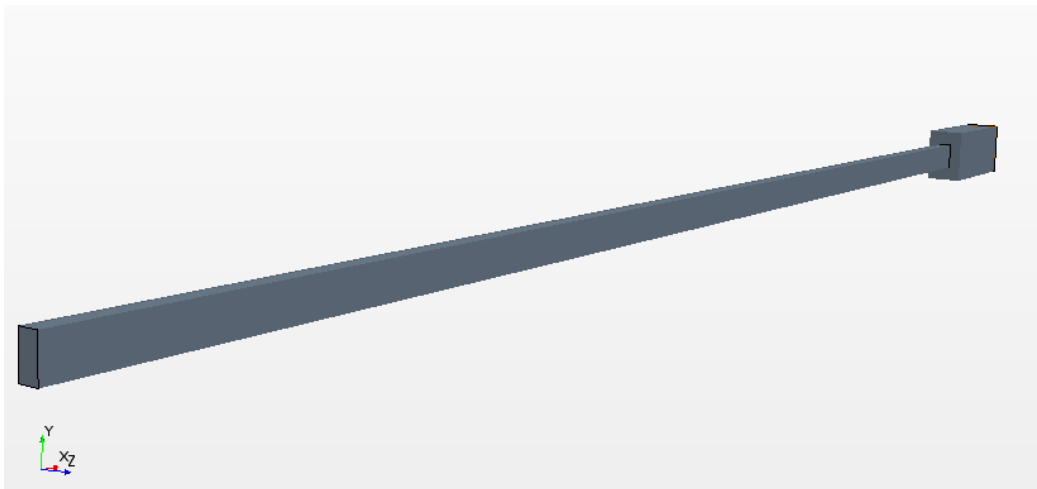
Figure 4: Geometry one.

Geometry two (see Figure 5) was a tube with a diameter of 78 mm and a length of 0.95 m. At the end of the tube there was a constriction in the tube that acted as a simplified version of the valve used in the experiments. It consisted of a 0.05 m long tube with a radius of 0.006 m connected to a smaller tube with a length of 0.01 m and a radius of 0.0025 m. This geometry also had a pressure outlet in the form of a tube with a length of 0.1 m and

a radius of 0.023 m.
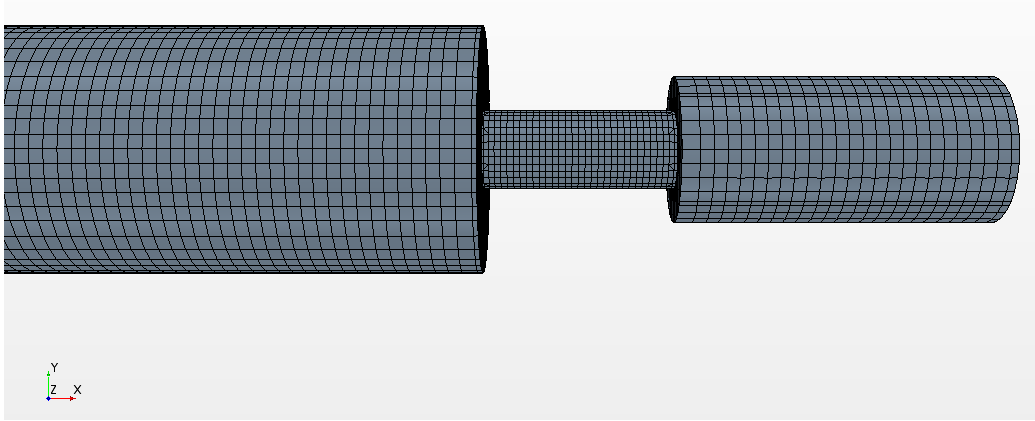
Figure 5: Geometry two.

Geometry three was the same as geometry two, except the main chamber had a diameter of 40 mm.

5.2   Grid/Mesh

In this thesis there were used three different types of mesh. Surface mesh, prism layer mesh and trimmed cell mesh.

In order to improve the quality of the geometry surface and optimize it for the volume mesh models, the surface mesh retriangulated the surface. As well as improving the surface for the volume mesh it also aided the subsurface generator when the prism mesh option was selected [20].

The prism mesh option was applied to the geometry together with the core volume mesh, in this case the trimmed cell mesh, to generate orthogonal prismatic cells next to the wall surfaces or boundaries. This layer of cells improved the accuracy of the flow next to the walls and boundaries, and hence the accuracy of the total solution [20].

The trimmed cell mesh was a grid of high quality for this fairly simple geometry.

The mesh base size for the generated mesh for both geometry one was 0.003 m. The mesh base size for geometry two was 0.004 m and for geometry

three the mesh base size was 0.0028 m. Inside all the geometries volumetric refinement was used to create finer mesh, and an even finer mesh, 50 percent of the base size, in the area where the particles interacted with air and in the valve area for geometry two and three. The mesh count for geometry one, geometry two and geometry three were 412 969, 245 380 and 214 043.

Figure 6 and Figure 7 show a cross-section of the mesh in the closed and the open end of geometry one, respectively.
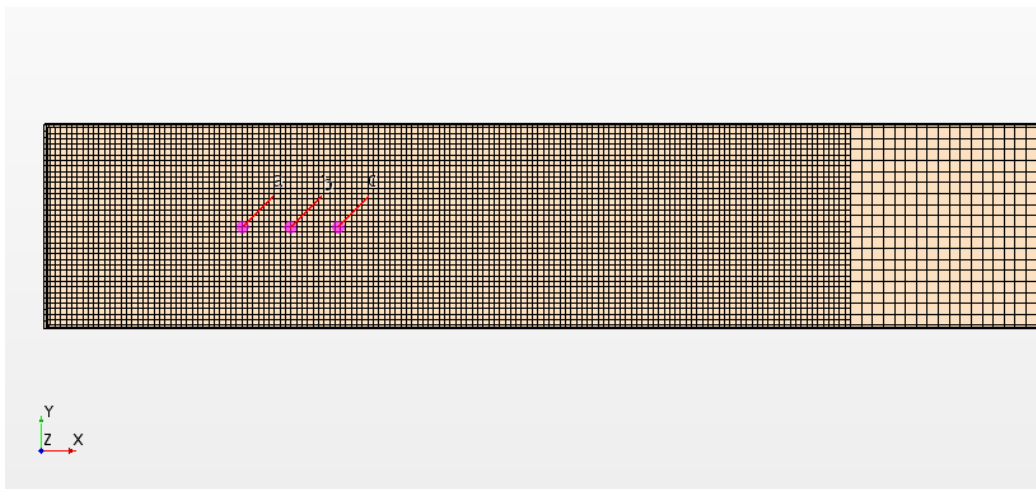
Figure 6: Mesh one.
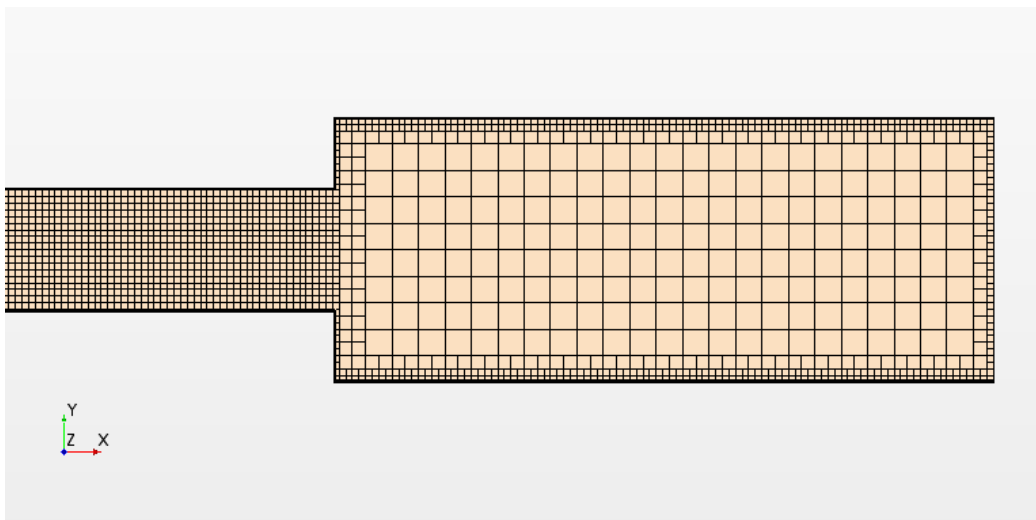
Figure 7: Mesh one.

Figure 8 and Figure 9 show a cross-section of the mesh in the closed end of geometry two and the open end of geometry three, respectively.
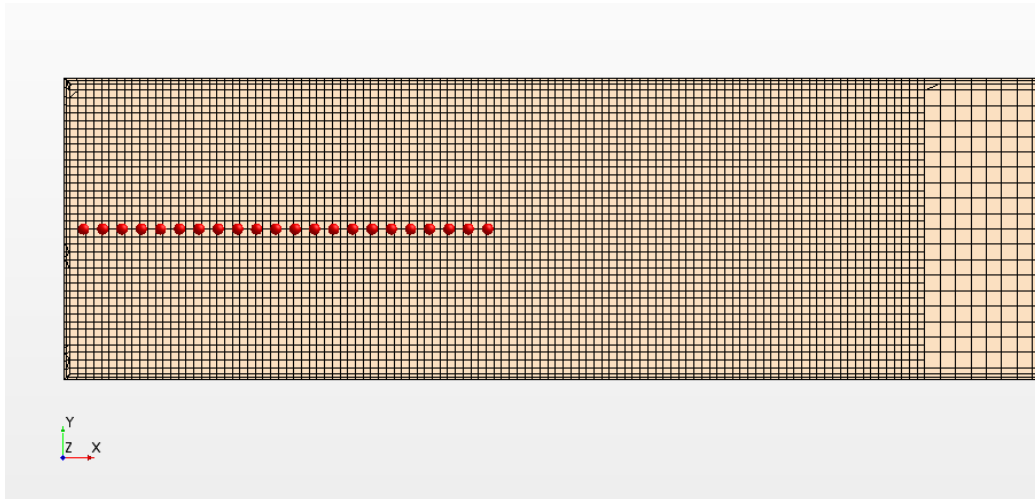
Figure 8: Mesh two.
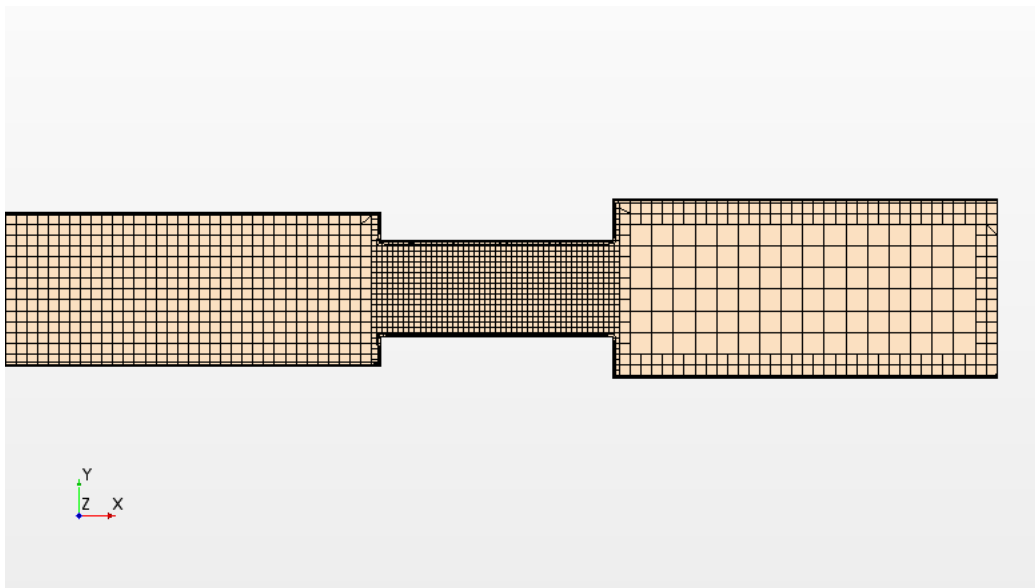
Figure 9: Mesh three.

5.3 Models

In STAR-CCM+ the physics models define which mathematical formulas and conditions are used to decide the behaviour of the specified material. They

work together with the solvers to obtain a solution.

The multiphase segregated flow model was used to model Eulerian Multiphase cases (E-E cases) by solving a set of conservation equations for each Eulerian phase in the simulations. The pressure was assumed the same in the different phases, but the velocity and physical properties differed. The share of the flow domain that each phase occupied was given through the volume fraction.

The segregated fluid temperature model was used to solve the total energy equation in the continuum with the temperature as the solved variable. Enthalpy was then computed from temperature. This model is, according to the STAR-CCM+ user manual, appropriate for simulations that do not involve combustion. The segregated fluid isothermal model was applied to some simulations, which kept the continuum temperature constant.

The implicit unsteady model was the only available unsteady model that could be used with the segregated flow model. This model used the implicit unsteady solver.

To describe the phases, the Realizable K-Epsilon model with high y+ wall treatment was used for both the continuous phase and the dispersed phase. The Standard K-Epsilon model is a two-equation model that contains transport equations for the turbulent kinetic energy and its dissipation rate. The Realizable K-Epsilon model differs from the standard K-Epsilon model in that it contains a new transport equation for the turbulent dissipation rate. Also, a critical coefficient, C, of the model is expressed as a function of mean flow and turbulence rather than assumed constant. This model has shown to give results that are at least as accurate than the standard model. The high y+ wall treatment performs three important functions. It specifies the reference velocity used in the wall laws, computes a value of turbulent production in the wall cell and computes a value of turbulent dissipation in the wall cell.

As described in Section 4.5, the model for drag force was enabled to account for interaction between particles and the air. To prevent the particles from exceeding the maximum packing limit, the Solid Pressure model was activated.

5.4 Solvers

The solvers in STAR-CCM+ work with the models to obtain a solution. They are activated once per iteration, and act as a control of the solution. What makes the solvers different from models is that the scope of a model is limited to the continuum in which it is defined, while the span of a solver can be over multiple continua. By the approach of domain decomposition, STAR-CCM+ breaks the computational domain into two separate sub-domains to make use of parallel processing. Before any physics solvers can be activated on a common iteration or time-step, the Partitioning solver is activated to ensure that the domain decomposition is up to date.

The Implicit Unsteady solver was used as the Implicit Unsteady model was activated. This solver controls the update at each physical time for the calculation as well as the size of the time-step.

All turbulence models require the Wall Distance solver which controls the wall distance for all continua where wall distance is calculated. Wall distance represents the distance from a cell centroid to the nearest wall face with a non-slip boundary condition.

The Multiphase Segregated Flow solver was used. In STAR-CCM+ this has several tasks. First of all, it controls the solution update from the Multiphase Segregated Flow model. In addition to this the Segregated Flow solver controls the Phase Coupled Velocity solver and the Pressure solver. The purpose of the former is to solve the discretized conservation equations to obtain the intermediate velocity field for each phase, which in turn are used to correct the cell velocities. It also controls the under-relaxation factor and algebraic multigrid (AMG) parameters for the phase momentum equations. The Pressure solver updates the pressure field by solving the discretized equation for pressure correction.

The K-Epsilon Turbulence solver was activated to control the solutions in all continua where the K-Epsilon model was activated. Working together with this solver is the K-Epsilon Turbulent Viscosity solver, which controls the update of the turbulent viscosity.

To control the solution update of the Segregated Fluid model, the Energy solver was used. This solver sets the under-relaxation factor and AMG parameters for the energy equation.

5.5 Initial conditions

Particles and air

For the experiments done in [19], Medvedev et al. used corn starch dust. Some parameters of the dust are given in Table 1. These parameters were used in the simulation in section 7.

Table 1: Properties of corn starch dust.

Mean particle diameter	10 μm
Density of particles	1300 kg/m^3
Particle layer height	50 mm
Approximate particle volume fraction	0.5
Maximum solid fraction	0.624
Lowest explosion limit (LEL) concentration in air	0.06 kg/m^3
Lowest explosion limit (LEL) volume fraction in air	$4.6 \cdot 10^{-5}$
Stoichiometric concentration in air	0.233 kg/m^3
Stoichiometric volume fraction in air	$1.792 \cdot 10^{-4}$

Table 2 contains the properties of the particles used in the experiments conducted in this thesis. These properties were also used in the simulations in Section 10 and Section 11.

Table 2: Properties of SIGMA glass bead particles, unwashed.

Mean particle diameter	$\leq$ 106 μm and 212 - 300 μm
Density of particles	2530 kg/m^3
Particle volume fraction	0.56

The layer of dust were in all the simulations and experiments placed at the end of the HPC, as displayed in Figure 3 in Section 2.

The ideal gas model was activated so the air was treated as compressible. Other properties of air are given in Table 3. These are values used in all simulations.

Table 3: Properties of air.

Material properties	Value
Dynamic viscosity	$1.85 \cdot 10^{-5}$ Pa-s
Molecular weight	28.96 kg/kmol
Specific heat	1003.62 J/kg-K
Thermal conductivity	0.026 W/m-K
Turbulent Prandtl number	0.9

Pressure and velocity

The tube was divided into two zones of different initial air pressure and size, depending on what simulation was run, by a field function. The pressure values entered in the field function were pressure above atmospheric pressure, and the values exported from STAR-CCM+ were given in absolute pressure.

To ease forward differencing of the governing equation in the generated mesh, the velocity magnitude in the gas was set to 0.01 m/s in the x-direction. The velocity magnitude for the particles was set to $1.0 \cdot 10^{-5}$ m/s, also in the x-direction.

The gravity model accounts for gravitational acceleration on materials in the physics continuum. It was set to 9.81 meter per second per second and acted in the negative x-direction.

Time-step and inner iterations

For the simulations, a time-step of $1.0 \cdot 10^{-5}$ was used. Bigger time-steps made the solution unstable, and smaller time-steps increased the computational time significantly. Temporal discretization was set to first-order, since second-order proved to be hard to stabilize. This is discussed in Section 6.

Under-relaxation factor

Introducing a relaxation factor has shown to reduce the number of iterations necessary to achieve convergence and therefore reducing the computational time by a factor of up to 30 [5]. At each iteration the under-relaxation factor governs to which extent the newly computed solution replaces the old one, and therefore decides how quickly a solver will obtain a solution. The under-relaxation factor may have a value ranging from 0 to 1, 0 giving the slowest solution and 1 the fastest. For an unsteady two-phase flow diverging,

changing the under-relaxation factor for the solvers can lead to convergence.

For the different solvers, these were the factors used:

- **Multiphase Segregated Flow solver**:

  1. **Phase Coupled Velocity solver**: The under-relaxation factor was set to 0.3 and the convergence tolerance was set to $1.0 \cdot 10^{-4}$.

  2. **Pressure solver**: The under-relaxation factor was set to 0.3 and the convergence tolerance was set to $1.0 \cdot 10^{-4}$.

- **Volume Fraction solver**: The under-relaxation factor was set to 0.1 and the convergence tolerance was set to $1.0 \cdot 10^{-4}$.

- **Segregated Energy solver**: The under-relaxation factor was set to 0.9 and the convergence tolerance was set to $1.0 \cdot 10^{-4}$.

- **K-Epsilon Turbulence solver**: The under-relaxation factor was set to 0.1 and the convergence tolerance was set to $1.0 \cdot 10^{-4}$.

- **K-Epsilon Turbulent Viscosity solver**: The under-relaxation factor was set to 0.3 and the Maximum Ratio, the maximum allowance ratio of turbulent to laminar viscosity, was set to $1.0 \cdot 10^{7}$.

Turbulence specification

For turbulent specification the K + Epsilon method was chosen. One node for Turbulent Dissipation rate and one node for Turbulent Kinetic Energy was added to the initial conditions for both phases. For the continuous phase, air, the Initial Turbulent Dissipation Rate was set to 0.1 m^2/s^3 and the Turbulent Kinetic Energy was set to 0.001 J/kg. For the dispersed phase, the particles, the Initial Turbulent Dissipation Rate was set to 0.1 m^2/s^3 and the Turbulent Kinetic Energy was set to 0.001 J/kg.

5.6 Boundary Conditions

The boundary conditions, and sometimes the initial conditions, dictate the particular solutions to be obtained from the governing equations [5]. The geometry under investigation had wall and outlet boundaries.

5.6.1 Outlet boundaries

- The pressure was decided with the same field function as used to decide the pressure through the pressure chamber.

- The volume fraction of both air and particles was decided in the field function used to decide the pressure through the pressure chamber.

- Turbulence specification was set to K + Epsilon.

- Turbulent kinetic energy was set to 0.001 J/kg.

- Turbulent dissipation rate was set to 0.1 $\mathrm{m}^2/\mathrm{s}^3$.

5.6.2 Wall boundaries

No slip was set as the method for shear stress specification for both air and particles. The thermal specification was set to adiabatic, which means that no heat transfer was permitted across the boundary.

5.7 Riemann solution

The expected behaviour of the shock wave, of the contact wave and of the rarefaction wave is described by Toro in [21]. The Sod shock tube problem is a Riemann problem and common test for the accuracy of computational fluid codes. The solution consists of a right travelling shock wave, a right travelling contact discontinuity and a left travelling sonic rarefaction wave. Figure 10 shows the solution profile for density, velocity, pressure and specific internal energy across the complete wave structure.
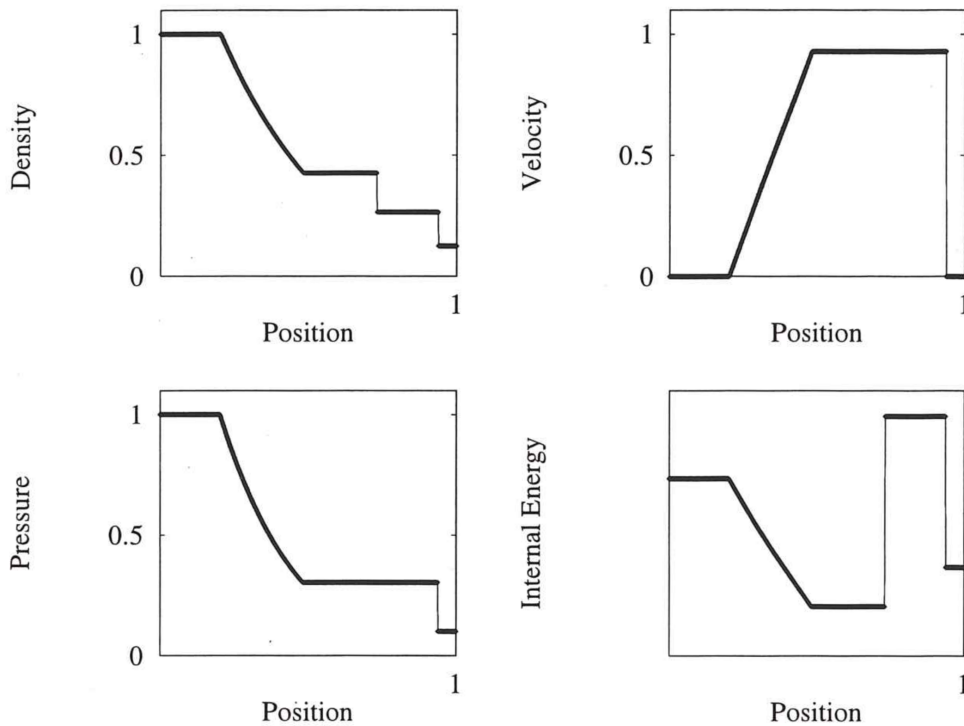
Figure 10: Exact solution for density, velocity, pressure and specific internal energy at a certain point in time [21].

The discontinuity at x ≈ 0.75 in the density plot and in the internal energy plot, is the contact discontinuity. This is a surface that separates areas of different density and temperature. The pressure across the surface is per definition in equilibrium [2].

When solving for the contact discontinuity numerically, it is difficult to get an accurate solution compared with the shock wave. This has to do with the characteristics around the contacts of the waves. Around the contact discontinuity the characteristics run parallel to the wave, while the characteristics on either side of the shock wave runs into the wave making it easier to compute numerically [21].

5.8 Simulations

Verification simulations

For verification of the models used in this thesis, simulations were run and compared with the exact Riemann solution described in Section 5.7. Two simulations were run with geometry one. Differences are given in Table 4.

Table 4: Differences between simulation 1 and simulation 2

Simulation	Energy model
1	Segregated fluid temperature
2	Segregated fluid isothermal

According to the STAR-CCM+ user manual [20], it would be computational expensive to solve an ordinary energy equation in a problem that has no or little temperature variation. Therefore simulation 2 was run and compared to simulation 1 and the exact Riemann solution. Simulation 2 had all the same settings as simulation 1, except for a constant temperature field. A constant energy model means that instead of solving the energy equation (see Section 4.4), a constant energy field is provided to all models that require temperature.

For the verification simulations:

- A section with the length of 1.2 meters was studied. The HPC was set to be between 0 and 0.5 meter and the LPC from 0.5 meter to 2.6 meter.

- The simulations were set to terminate after 0.00097 seconds. At this time the characteristics of the rarefaction wave, the contact discontinuity and the shock wave were clearly visible.

- Initial pressure in the HPC were set to 3.01 bar and in the LPC 1.01 bar.

The results from the simulations were compared to the exact Riemann solution at time = 0.00097 seconds, HPC at 3.01 bar and LPC at 1.01 bar.

Simulations of previous experiments

Simulations 3 - 7 are simulations with initial conditions like the experiments conducted by Medvedev et al. in [19].

Table 5: Initial conditions of simulations 3 - 7.

Simulation	3	4.1	4.2	4.3	5	6	7
Length of HPC [m]	1.57	2.07	2.07	2.07	2.57	1.57	2.57
Length of LPC [m]	1.03	0.53	0.53	0.53	0.03	1.03	0.03
Initial pressure in HPC [barg]	1.04	1.04	1.04	1.04	1.04	0.40	0.40
Initial pressure in LPC [barg]	0	0	0	0	0	0	0
Fluid energy model	-	-	segregated fluid temp.	segregated fluid temp.	-	-	-
Geometry	one	one	one	one, closed end	one	one	one

The simulations were run with a fluid energy model of constant temperature, except for simulation 4.2 and 4.3 which were run with the segregated fluid temperature model.

Simulations of experiments with the valve

Simulation 8 - 19 are simulations conducted with geometry two and three, which are similar to the geometries used in the experimental part of the thesis. Initial conditions are given in Table 6. The particles had a diameter of 106 μm, with the rest of the dust properties given in Table 2. The fluid energy model used was the segregated fluid isothermal.

Table 6: Initial conditions of simulations 8 - 19.

Simulation	Pressure [barg]	Layer height [mm]	HPC diameter [mm]
8	1	10	40
9	5	10	40
10	1	30	40
11	5	30	40
12	1	50	40
13	5	50	40
14	1	10	78
15	5	10	78
16	1	30	78
17	5	30	78
18	1	50	78
19	5	50	78

6 Verification of the model
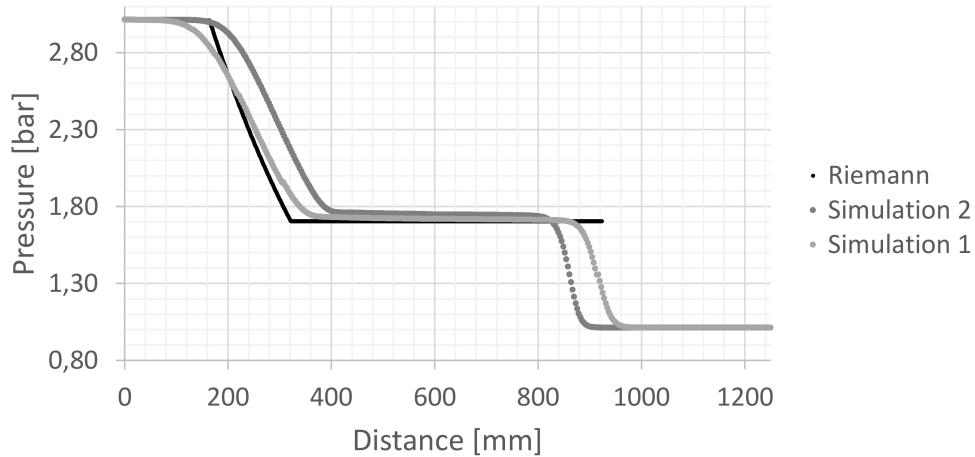
Figure 11: The pressure of air as a function of position through the geometry.

Figure 11 shows pressure plotted as a function of position through the pressure chamber. The rarefaction wave is from the exact Riemann solution identified as the pressure drop from around 3 bar at 160 mm to 1.7 bar at 320 mm and the shock wave is the zero-width transition from 1.9 bar to 1 bar at around 920 mm. The zone in between, from 320 mm to 920 mm is called the star region[21]. As can be seen in Figure 11 simulation 1 is in good correspondence with the exact Riemann solution. However, the shock wave is "smeared" across more cells than the zero-width Riemann shock wave. The rarefaction wave has similar characteristics in that it is also "smeared". This is mainly in the head and the tail of the wave, where an error in the derivative exists. Both the start-pressure, the end-pressure and the pressure in the star region for simulation 1 comply with the exact Riemann solution. The pressure in the star region is slightly higher for simulation 1.

The pressure in the star region for simulation 2 is even higher than for simulation 1. In addition to this it appears that the speed of propagation for both the shock wave and rarefaction wave is not correct. It is important to notice that the head of the rarefaction wave is moving at a high velocity, approximately sonic (see Table 7), over a short distance. In Figure 11 the rarefaction wave for simulation 2 is, at the most, approximately 40 mm behind the exact Riemann solution. This corresponds to, assuming a velocity

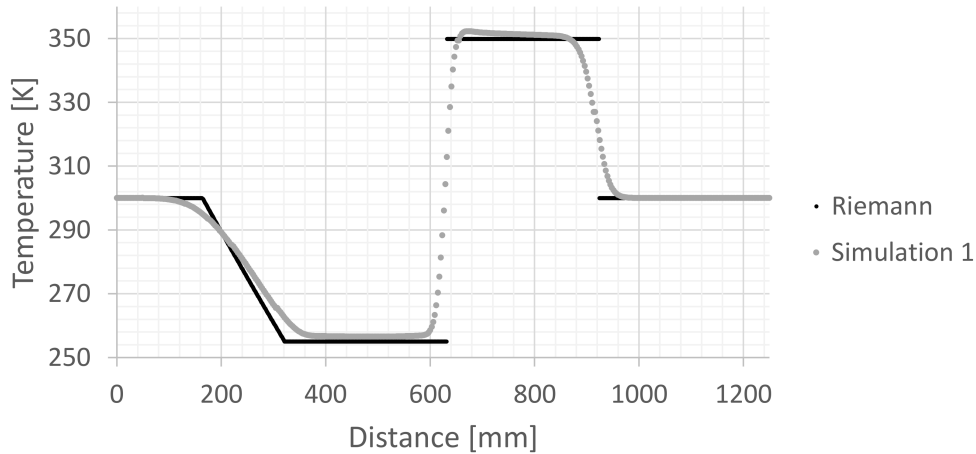at the speed of sound, a delay of only 0.11 ms.
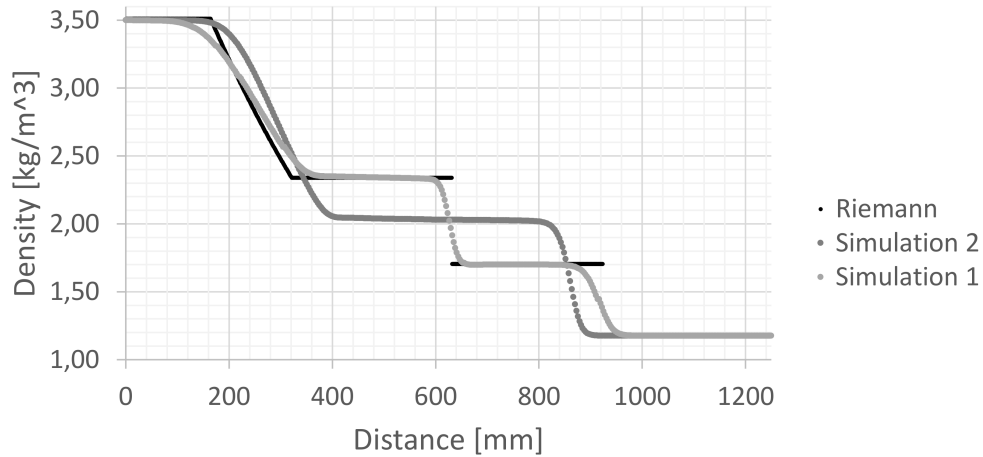
Figure 12: The density of air as a function of position through the pressure chamber.

Figure 12 shows the density of air as a function of distance through the pressure chamber. Both the exact Riemann solution and the solution from simulation 1 stabilizes at around 2.35 kg/m^3 after the rarefaction wave, before dropping to 1.7 kg/m^3 after 600 mm. This drop is the contact discontinuity and separates areas of different density and temperature. It is not, or should not, be visible in the pressure and velocity plots because the pressure and velocity is per definition in equilibrium across the contact discontinuity [2].

Simulation 2, on the other hand, shows no sign of a contact discontinuity. This is because the segregated fluid isothermal model used in simulation 2 keeps the temperature in the continuum constant. Therefore, as the shock wave propagates through the LPC, the energy that in simulation 1 is used to increase the temperature and density will be spent solely on increasing the density. As the rarefaction wave in simulation 1 propagates through the HPC, the pressure decreases leading to a decrease in temperature and density. In simulation 2 the temperature is kept constant, leading to a lower density than in simulation 1.
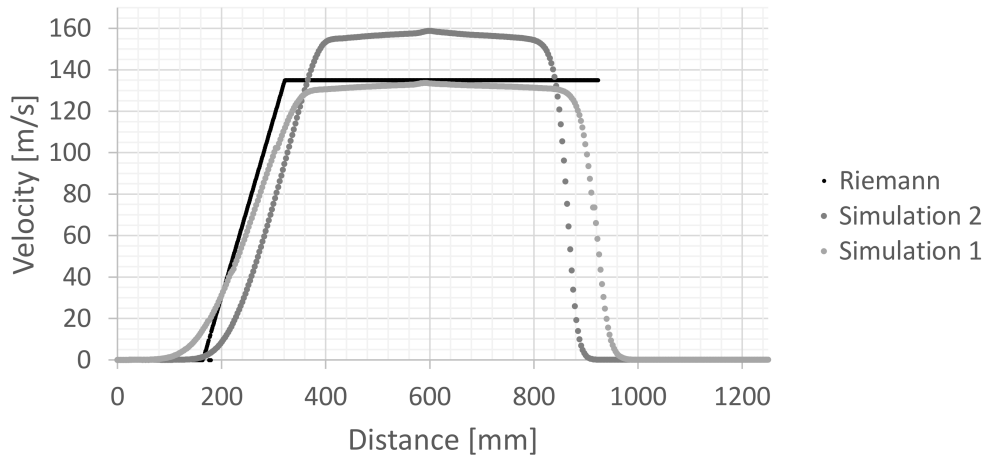
Figure 13: The velocity of air as a function of position through the pressure chamber.

Figure 13 shows the velocity of air as a function of distance through the pressure chamber. The exact Riemann solution shows that the velocity increases from 0 m/s at 160 mm to around 135 m/s at 320 mm. The velocity is constant through the pressure chamber until it falls to zero at around 920 mm. Simulation 1 is matching the exact solution fairly good, but with a longer rarefaction- and shock wave. The velocity is not constant in the star region and its highest value is 135 m/s at 600 mm.

The velocity plot for simulation 2 shows a velocity approximately 25 m/s higher than in simulation 1 with a peak of 160 m/s at 600 mm. The drag force is dependent on the relative slip velocity between phases (See Equation (4.5) in Section 4). This is investigated further in Section 7.

Figure 14: The temperature of air as a function of position through the pressure chamber.

Figure 14 shows the temperature as a function of distance through the pressure chamber. Temperatures in front of the rarefaction wave and in front of the shock wave are the initial conditions, 300 K. The rarefaction wave lowers the temperature for the exact Riemann solution to 264 K and for the simulation a few degrees higher. After the contact discontinuity at 640 mm, the temperature jumps to around 350 K.

Temporal discretization was first set to 2nd-order, which provided the option of doing time discretization with four or five levels [20]. The model turned out to be hard to stabilize, and was therefore changed to first-order. While the exact solution of a shock-wave has a zero-width transition zone, first-order methods tends to "smear" the shock-wave over several computing cells. The contact discontinuity is also supposed to have a zero-width transition zone, but this is, as can be seen in Figure 12 and Figure 14, also "smeared". This smearing may seem unsatisfactory but is in fact common [21] and, in this case, acceptable since we consider the behaviour of the rarefaction wave. However, it seems like the rarefaction wave is a victim of the "smearing" as well. Because of this the rarefaction wave for simulation 1 is slightly longer than what it is supposed to be, according to the exact Riemann solution. The rarefaction wave does not have a zero-width transition zone. In fact, it has quite the opposite behaviour in that it expands. This is because the velocity of the wave, relative to the observer, is the velocity of the gas minus the speed of sound [2]. The gas in the region that the head of the wave propagates into has not yet started moving, giving the head of the

rarefaction wave an absolute velocity equal to the speed of sound. The gas in the region of the tail of the rarefaction wave is flowing the opposite way of the rarefaction wave, giving it an absolute velocity less than the speed of sound.

7 Simulations compared to previous experiments and simulations

Medvedev et al. [19] used surveillance points at heights 5 mm (a), 18 mm (b) and 31 mm (c) over the layer measuring concentration as a function of time. These points were in simulation 3 - 7 named a, b and c, and can be seen in Figure 6 in Section 5.2. When the dust concentration in point a started to change, one could say that the dust had "arrived" at this point. The same applied for point b and c. In this way the height of the dispersed dust could be plotted as a function of time. How steep the lines between point a, b and c are, will give information about the average velocity of the dust cloud between the points. Point a was also used to record the pressure as a function of time. This plot not only shows the arrival of the rarefaction wave, but also some of the wave characteristics.

For the simulations, the volume fraction as a function of x-direction in the pressure chamber for different times are shown. The volume fractions were measured in points, approximately one for each mesh cell, on a line along the center of the geometry.

Medvedev et al. postulated $t_0 = 0$ as the initial moment of interaction between rarefaction wave and dust layer. $t_0 = 0$ was set to the time of interaction between the dust layer and rarefaction wave for simulations 3 - 7. Table 7 shows the time from initiation of the rarefaction wave until the first pressure drop was noticed in probe a. Knowing the length of the HPC and the height of the dust layer, the average velocity of the rarefaction wave could be calculated.

Table 7: Time from initiation of rarefaction wave until arrival at dust layer for simulation 3 - 7.

Simulation	Time [s]	Average velocity [m/s]
3	0.0045	336.66
4.1	0.0061	335.83
4.2	0.005	403.00
4.3	0.005	403.00
5	0.0077	326.62
6	0.0044	344.32
7	0.0076	330.92

In dry air at 20 deg C, the speed of sound is 343 meter per second [16]. The head of the rarefaction wave should, according to [2], travel at a speed equal to the speed of sound. Table 7 shows that the head of all the rarefaction waves in simulation 3 - 7 travels close to, or at, sonic speeds. This is true for all the simulations except simulation 4.2 and simulation 4.3, which apparently travels at speeds way above sonic. The reason for this is, as discussed in Section 6, the "smearing" of the rarefaction wave. This "smearing" makes the rarefaction wave arrive at probe a before it is supposed to. By assuming the head of the "real" rarefaction wave travels at sonic speed and using t_0 for simulation 4.2, the "smearing" can be calculated to 300 mm, or 0.875 ms, ahead of the exact solution. The same logic can be used to show that the propagation speed of the rarefaction waves in simulation 3, 4.1, 5, 6 and 7 is too low.

The criterion for what dust concentration counted as "detected" by probe a, b and c in [19] was unclear. However, a lower explosion limit (LEL) was specified, therefore the dust cloud in simulation 3 - 7 was considered "detected" when the volume fraction exceeded LEL.

Table 8: Time from t_0 until the volume fraction exceeds LEL in probe a, b and c for simulation 3 - 7.

Simulation	Time at a [s]	Time at b [s]	Time at c [s]
3	0.00118	0.00294	0.00457
4.1	0.00135	0.00336	0.00504
4.2	0.00136	0.00328	0.00516
4.3	0.00135	0.00308	0.00460
5	0.00152	0.00375	0.00545
6	0.00138	0.00415	0.01296
7	0.00170	0.00422	0.00651
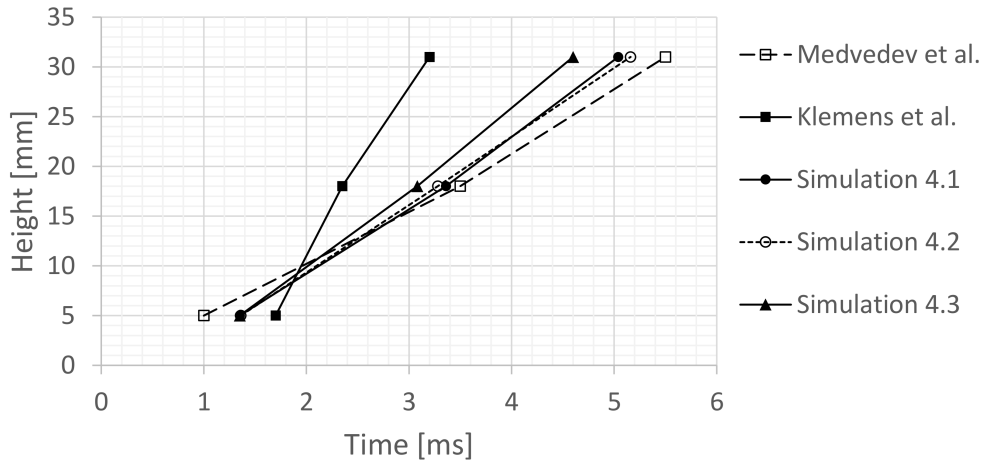
Figure 15: Dust lifting height above initial dust bed as a function of time. Results from simulation 4.1, simulation 4.2 and simulation 4.3 compared to Medvedev et al. [19] and Klemens et al. [13].

Figure 15 shows the height of probe a, b and c plotted against the LEL detection times for simulation 4.1 and simulation 4.2, together with results from previous simulations and experiments presented in research litterature. For simulation 4.3 the volume fraction in probe c never reached LEL, so the dust cloud had to be considered detected at a volume fraction of $1 \cdot 10^{-5}$. This lead to a shift to the left for the point at height 31 mm. The results from the simulations by Klemens et al. [13] are read of a similar plot, then re-entered here and therefore have an uncertainty of approximately ± 0.1 ms. The results from the experiment by Medvedev et al. [19] are read of a hand-drawn concentration vs. time plot for each of the probes a, b and c, and therefore have a higher uncertainty.

As can be seen in Figure 15, the difference between the initial dust lifting for simulation 4.1, simulation 4.2 and simulation 4.3 is not big. It looks like the dust lifting velocity is about the same at 5 mm. At 18 mm, simulation 4.3 is slightly ahead of simulation 4.1 and simulation 4.2. At 31 mm, simulation 4.3 is even further ahead. This is, as mentioned earlier, because of the low detection volume fraction for probe c in simulation 4.3. The low volume fraction is probably a result of the reflected shock wave returning from the closed end. The returning shock wave can be seen as the increase in pressure around 5 ms in Figure 16.

Overall, the initial dust lifting in simulation 4.1, simulation 4.2 and simula-

39

tion 4.3 match the experimental values well, except for a slightly high dust lifting velocity seen from the higher slope in the lines. The simulation conducted by Klemens et al. [13] seems to have overestimated the initial dust lifting velocity.
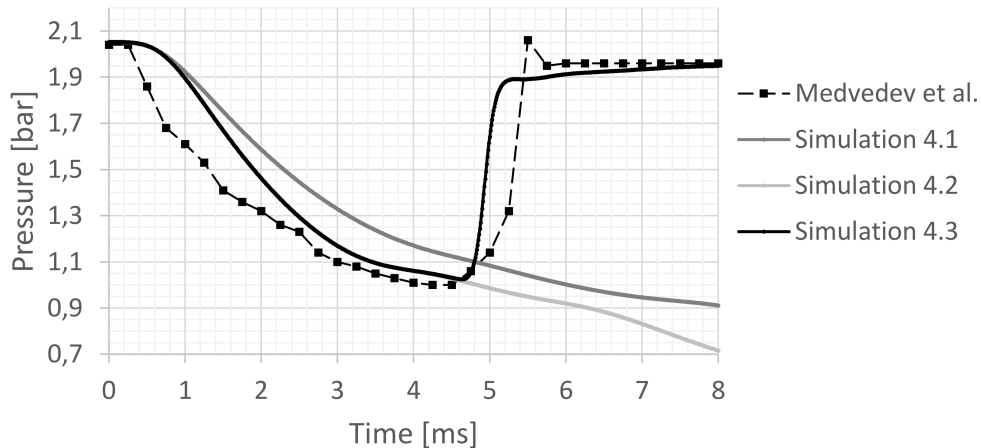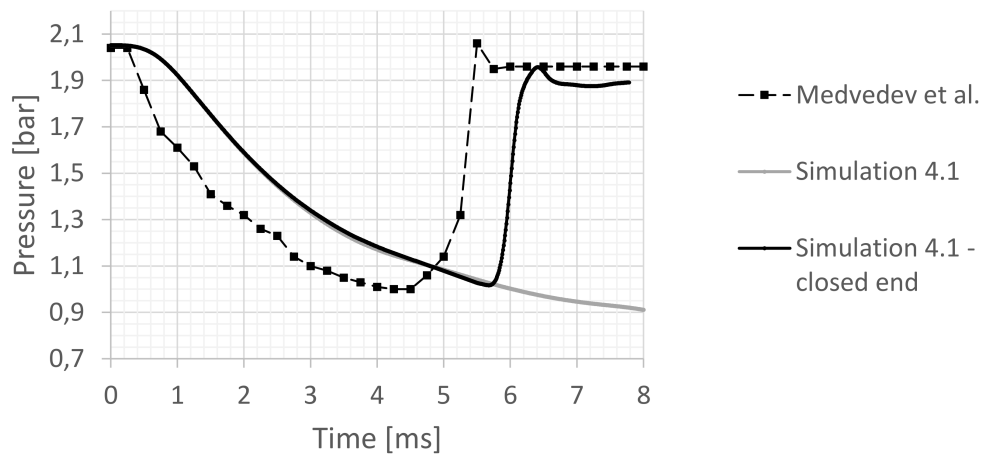

Figure 16: Pressure record from point a in Medvedev et al. [19] compared to simulation 4.1, simulation 4.2 and simulation 4.3.

The pressure record, from point a, of the experiment by Medvedev et al. [19] equivalent to the conditions in simulation 4.2 is, like the height-time plot, read of a hand-drawn plot and presented in Figure 16. It is compared to the pressure records obtained in simulation 4.1, simulation 4.2 and simulation 4.3. Simulation 4.2 and simulation 4.3 are almost identical until 4.6 ms, when the pressure for simulation 4.3 rapidly increases from around 1 bar to 1.9 bar. This increase is due to the shock wave returning from the closed end after being reflected. For simulation 4.2, which has an open end leading to the shock wave propagating out of the pressure chamber, the pressure keeps decreasing. The pressure in simulation 4.1 is from 1 ms higher than simulation 4.2, at times as much as 0.2 bar. From Figure 16 it looks like simulation 4.3 is in good correspondence with the experiment by Medvedev et al. The start pressure is the same, it hits a low point with approximately the same pressure and end with the same pressure. It also follows the same trends as the experiment. However, the pressure in the experiment decreases with a higher rate in the beginning than for the simulations, which all seems to be delayed, and a difference of around 0.3 ms exists between the returning shock waves for simulation 4.3 and the experiment.

Reasons for the delay could be the determination of t_0 for both the experiment and the simulation. If t_0 for the simulation is set set to a point in time where the change in pressure is steeper, the plot would shift left and give a better match at earlier times, but increase the discrepancy between the shock waves for simulation 4.3 and the experiment. Likewise, the plot of the experimental results would shift right if the change in pressure was detected before, which could be affected by parameters like the resolution, frequency and response time of the piezoelectric gauge monitoring the pressure. In addition to this, the placement of the gauge is not specified other than being located at the end of the HPC.

The biggest contributor to the shift in the simulation plot is probably, as discussed in Section 6 and displayed in Figure 11, the fact that the head of the rarefaction wave is "smeared" across a greater distance than it would be in reality. Because of this, t_0 for the simulation is defined earlier than it should had it not been "smeared".

Simulation 4.1, if adjusted for the "smearing" of the rarefaction wave, seems to have much the same traits as the experiment until the returning shock wave arrives. Therefore 4.1 was run once more with a closed end to investigate this further.

Figure 17: Pressure record from point a in Medvedev et al. [19] compared to simulation 4.1 and simulation 4.1 with a closed end.

If simulation 4.1 with closed end in Figure 17 is adjusted for the previously discussed "smearing", the plot trend would fit the experimental plot

by Mevedev et al. [19] well.

Assuming that t_0 for simulation 4.1, simulation 4.2 and simulation 4.3 is defined at a time 0.87 ms before it should, the height-time lines in Figure 15 are positioned too far to the right.
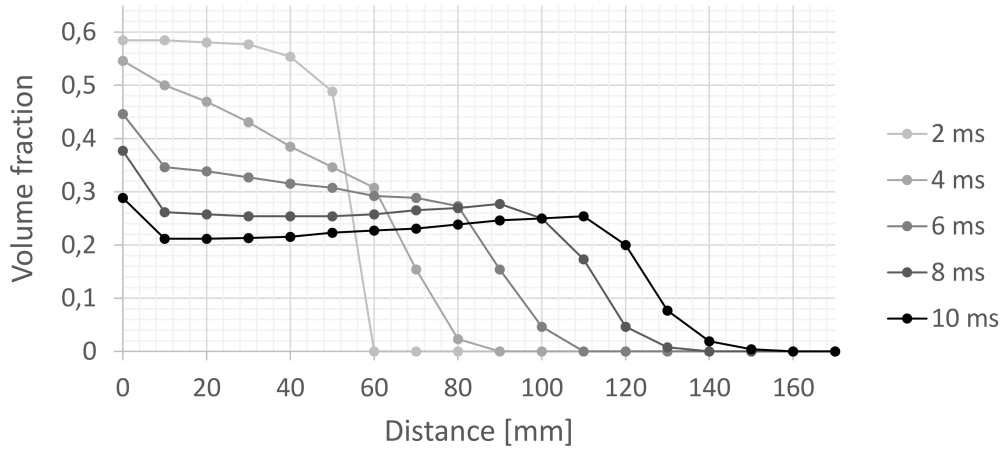
Figure 18: Volume fraction vs. distance from Klemens et al. [13].
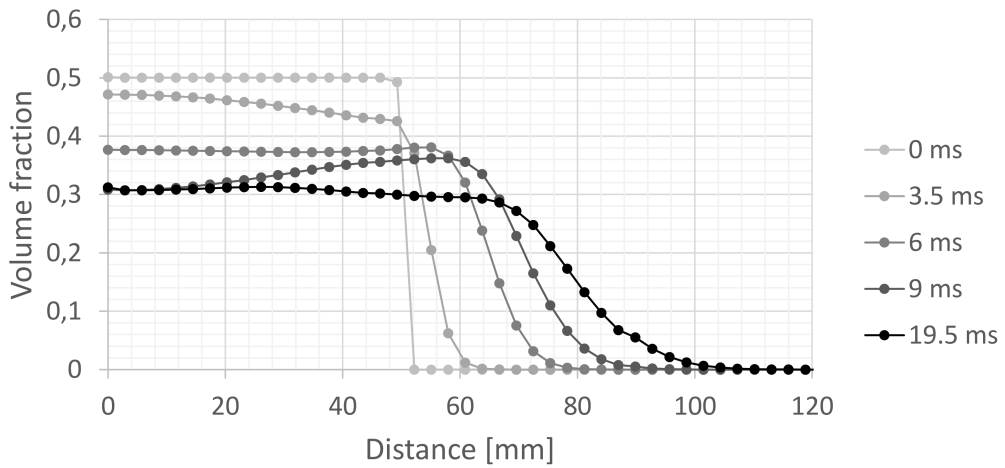
Figure 19: Volume fraction vs. distance from simulation 4.1.
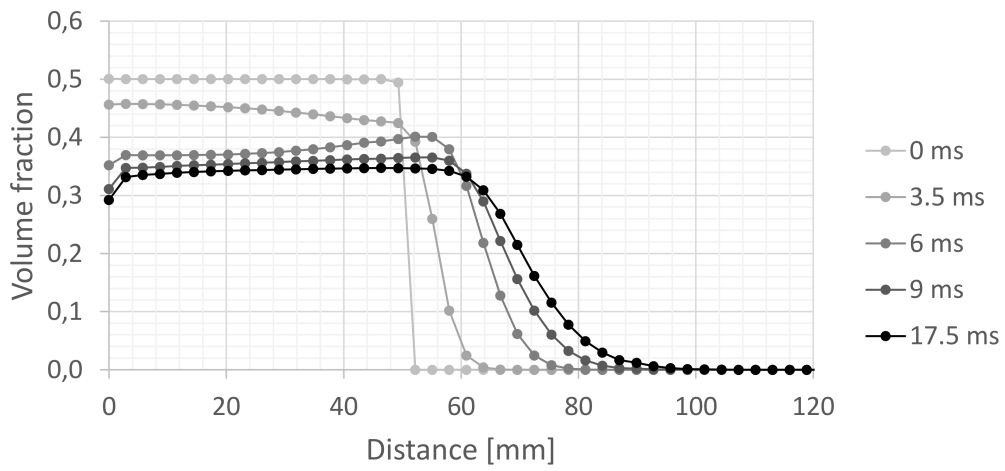
Figure 20: Volume fraction vs. distance from simulation 4.2.
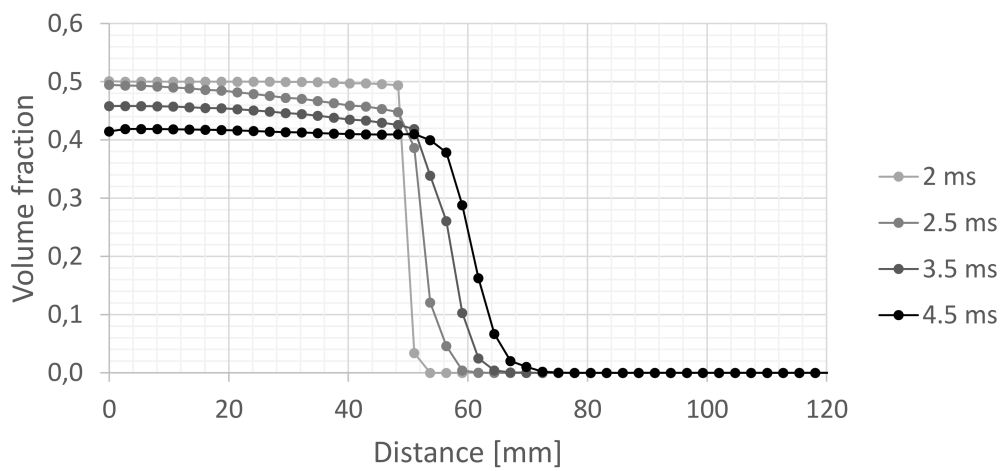
Figure 21: Volume fraction vs. distance from simulation 4.3 with closed end.

43
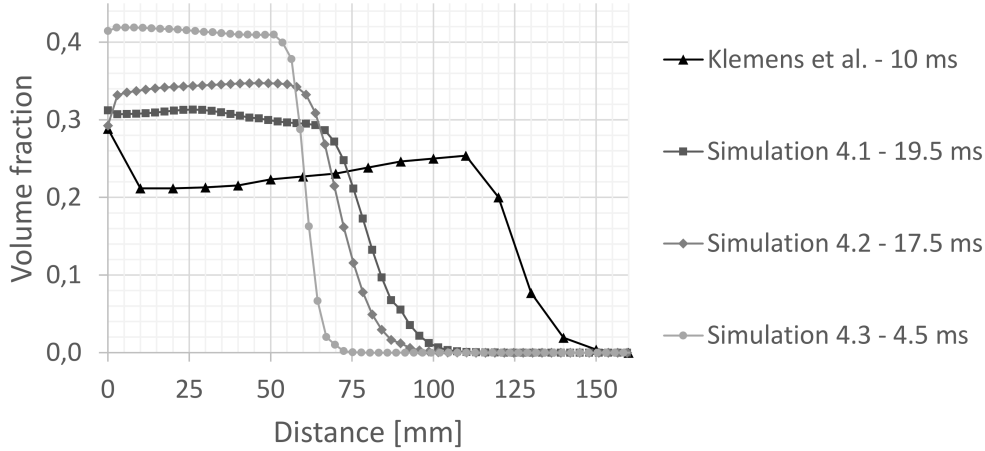
Figure 22: Maximum dust dispersion from simulation 4.1, simulation 4.2, simulation 4.3 and Klemens et al [13].

Figure 18, Figure 19, Figure 20 and Figure 21 shows volume fraction of dust as a function of distance through the pressure chamber from the simulation by Klemens et al. [13], simulation 4.1, simulation 4.2 and simulation 4.3, respectively. Each of them show the distribution for different points in time since t_0. For simulation 4.1, simulation 4.2 and simulation 4.3, the plot series with the latest point in time is the time of greatest amount of dust-dispersion. In Figure 22 the maximum dust dispersion from simulation 4.1, simulation 4.2, simulation 4.3 and Klemens et al [13] are compared in one figure.

The one-dimensional simulation by Klemens et al. [13] shows a volume fraction of 0.2 for as high as 120 mm after 10 ms. Simulation 4.1 has a maximum dust dispersion of volume fraction 0.2 at 76 mm after 19.5 ms. Simulation 4.2 has a maximum dust dispersion of volume fraction 0.2 at 70 mm after 17.5 ms. Simulation 4.3 has a maximum dust dispersion of volume fraction 0.2 at 60 mm in 4.5 ms. The one-dimensional model by Klemens et al. is dispersing the dust almost twice as far as the three-dimensional ones. The initial velocity of the dust can be approximated by the earlier points in time that shows a higher value for the one-dimensional simulation, which is consistent with Figure 15.

The maximum dust dispersion for the simulation with closed end, simulation 4.3, is not as great as for the open end scenario, simulation 4.2. By comparing the curves for the different points in time for both simulations, one can observe that the dust lifting velocity it slightly higher in simulation 4.3.

This complies with Figure 15. The maximum height of volume fraction 0.1 is 76 mm and 64 mm for open and closed end, respectively. After 4.5 ms the dust dispersion in the closed end simulation is at its maximum and the dust starts moving in the negative x-direction. Figure 16 shows that this is approximately the time of shock wave arrival. This indicates that simulation 4.2 and simulation 4.3 with closed end behaves much in the same way until the arrival of the reflected shock wave with its accompanying air flow, which seems to counteract the dispersion of dust.

Comparing simulation 4.1, which is run with the isothermal energy model, to simulation 4.2, which is run with the temperature energy model, shows a higher maximum dust dispersion for the isothermal case. This probably has to do with the higher air velocity for the isothermal case shown in Figure 13 in Section 6.

The figures created from the results obtained from simulation 3, simulation 5, simulation 6 and simulation 7 can be found in Appendix B.

Variation in mesh base size and time-step

Two additional simulations were run to investigate the effects of changing the grid size and the time-step. These simulations were based on simulation 4.2, but with different mesh base size and time-step. Specifications are given i table 9.

Table 9: Specifications for simulation 4.2.2 and 4.2.3 based on simulation 4.2.

Simulation	Mesh base size [m]	Time-step[s]
4.2	0.003	$1.0 \cdot 10^{-5}$
4.2.2	0.00125	$1.0 \cdot 10^{-5}$
4.2.3	0.003	$5.0 \cdot 10^{-6}$

Simulation 4.2.2 and simulation 4.2.3 were first run and compared to simulation 1 from Section 6, with the same initial conditions for the pressure distribution. This was done to see how changing the mesh base size and the time-step affects the rarefaction wave. Simulation 4.2.2 was an almost exact match with simulation 1. The comparison between simulation 4.2.3 and simulation 1 can be seen in Figure 23.
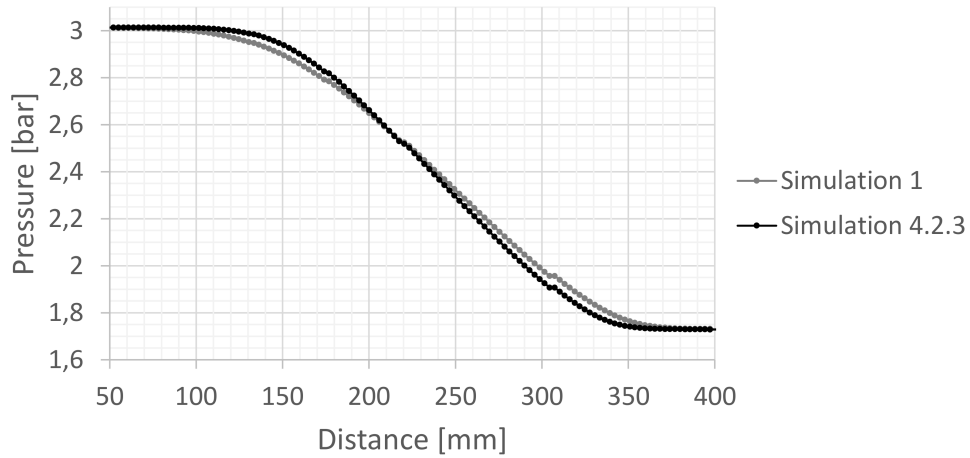
Figure 23: Pressure as a function of position with emphasis on the area of the rarefaction wave, comparison between simulation 1 and simulation 4.2.3.

Figure 23 shows the rarefaction waves of simulation 1 and simulation 4.2.3 after 0.00097 seconds. What this figure shows is that when decreasing the time-step, the rarefaction wave is less "smeared". Because of this, t_0 is expected to be defined at a later point in time. t_0 for the simulations are shown in Table 10.

Table 10: Time from initiation of rarefaction wave until arrival at dust layer for simulation 4.2, simulation 4.2.2 and simulation 4.2.3.

Simulation	Time [s]
4.2	0.005
4.2.2	0.005
4.2.3	0.0053
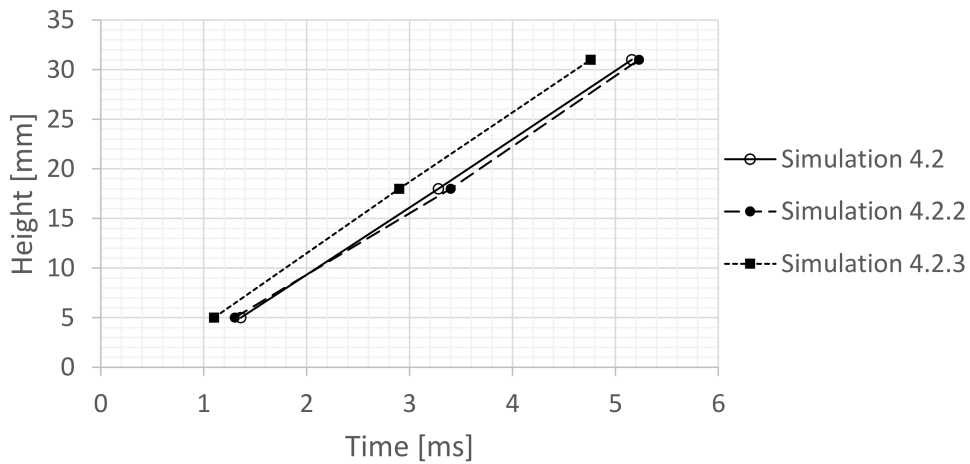
Figure 24: Height as a function of LEL detection time for simulation 4.2, simulation 4.2.2 and simulation 4.2.3.

Figure 24 shows height plotted as a function of LEL detection times for simulation 4.2, simulation 4.2.2 and simulation 4.2.3. As previously discussed t_0 is defined at a later point in time for simulation 4.2.3, which is probably the reason for the plot being positioned to the left of the others.
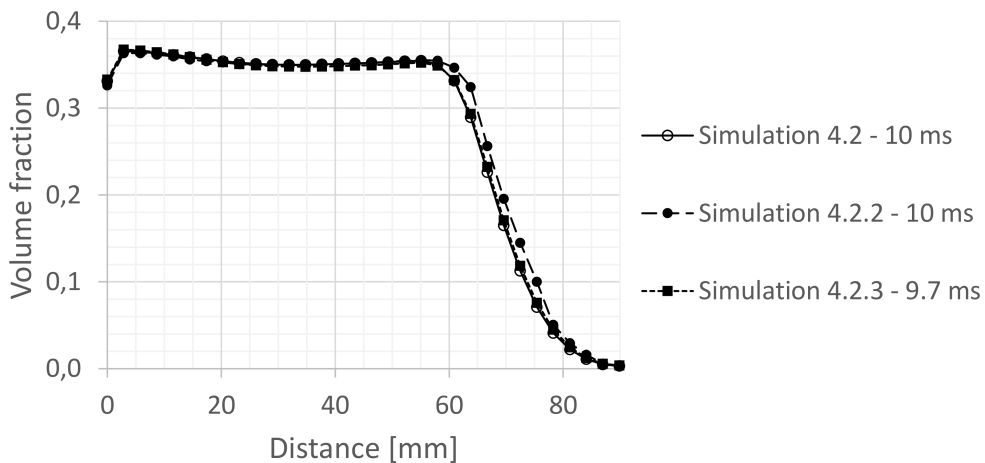
Figure 25: Volume fraction as a function of distance for simulation 4.2, simulation 4.2.2, simulation 4.2.3.

Figure 25 shows volume fraction as a function of distance through the pressure chamber for simulation 4.2, simulation 4.2.2 and simulation 4.2.3 at

approximately the same point in time.

Overall, changing the base mesh size from 0.003 m to 0.00125 m did not make any apparent changes to the rarefaction wave and did not seem to affect the dust dispersion much. When changing the time-step from $1.0 \cdot 10^{-5}$ to $5.0 \cdot 10^{-6}$ the rarefaction wave was less "smeared" which lead to t_0 being defined at an earlier point in time. This did not seem to affect the dust dispersion much, but did, however, increase the computational time substantially.

8 Experimental Procedure

8.1 Purpose and goal

To initiate a rarefaction wave, Mevdedev et al. [19] used a rupturing diaphragm mounted in a vertical shock tube. One of the goals in this thesis was to generate a rarefaction wave and observe some of the effects it is able to generate. Several ways of generating the rarefaction wave was considered, including a method similar to the one used by Medvedev et al. This method used pressure rupture disks, or diaphragms, mounted on the end of a pressure chamber. When the pressure inside the pressure chamber reached a certain point, the pressure rupture disk would give in and rupture. This would probably give the best results since the air-evacuation of the pressure chamber would be limited mostly by the air-properties. However, this method was discarded because the supplier would not be able to deliver in time and because the price exceeded the budget.

The method that was chosen was based on a solenoid valve. A solenoid valve mounted on top of a vertical aligned pressure chamber made out of an acrylic glass tube. After using compressed air to increase the pressure inside the pressure chamber, the solenoid valve could be activated and air would start to flow out of the pressure chamber. A rarefaction wave would now propagate through the pressure chamber towards a dust layer located at the end. The pressure chamber was made out of acrylic glass so that it was possible to observe the dust layer and record the process using a high-speed camera.

8.2 Equipment and Experimental setup

The valve

The valve used for the experiments was the 5404 2/2-way servo-assisted solenoid piston valve from Burkert. Some specifications are given in Table 11 and a cross-section of the valve is shown in Figure 26.

Table 11: Specifications for the valve used in the experiments [3].

Media	Neutral gasses and liquids
Media temperature	0 to 100 deg C
Voltage	200 - 240 V
Opening time	20 - 400 ms
Protection class	IP 65
Pressure range	1 - 50 bar
Air flow	10 800 l/min

1	Valve body	Brass
2	Seal (seat)	PTFE
3	Piston	Brass
4	Piston-seal	PTFE
5	O-rings	NBR (FKM optional)
6	Cover	Brass
7	Spring	1.4310 Stainless Steel
8	Plunger Seal	NBR (FKM optional)
9	Spring	1.4310 Stainless Steel
10	Plunger	1.4105 Stainless Steel
11	Armature guide tube:	1.4303 Stainless Steel
12	Stopper	1.4105 Stainless Steel
13	Coil	Polyamide (epoxy on request)
14	Cable plug	Polyamide

Figure 26: Cross-section of the Burkert solenoid valve.

8.2.1 Particle properties

For the experiments carried out in this thesis, two types of particles were used. These particles are described in Table 2 in Section 5.5. The density, and hence the volume fraction, of the particles was approximated using a beaker and a weight. The beaker was placed on the weight and filled half-full with water. By adding glass beads to the beaker and note the change in weight and volume, the density could be calculated.

8.2.2 The pressure chamber

Two different pressure chambers were constructed. One with a diameter of 78 mm and the other with a diameter of 40 mm, from here on referred to as geometry two and geometry three. They were built out of an acrylic glass

tube with plugs in each end held together by screws and a steel frame (see Figure 27).

Figure 27: The 40 mm pressure chamber, geometry three, to the left with the solenoid valve to the right.

8.2.3 High speed camera and software

To record the process in the pressure chamber during the evacuation of air, a high speed camera of the type Photron FASTCAM SA4 was used. The camera captured the events in a resolution of 1024 x 1024 pixels at 3600 frames per second (fps) through a software called Photron FASTCAM Viewer.

8.2.4 Other equipment

High quality recordings with a high number of frames per second demands a lot of light, so a 500 watt lamp was used for high quality results.

The pressure was read of a pressure gauge in the hose.

8.3 Experimental procedure

A measuring tape was fastened to the side of the bottom part of the pressure chamber with the purpose of controlling the height of the dust layer, as well as acting as a reference when studying the recordings. The top of the pressure chamber was removed and dust was poured inside. After closing the pressure chamber, compressed air was injected into the chamber through a Schrader valve at the top of the chamber next to the solenoid valve. As the chamber filled up, the pressure was read from an air pressure gauge in the hose. When the desired pressure was obtained, the high speed recording was activated as the solenoid valve was opened.

In the manual for the solenoid valve [3] the application areas are described (see Table 26). Gas and fluids are the only phases this valve is supposed to be used for. During the experiments, the valve had to be disassembled and cleaned as a result of glass particles entering the valve and keeping it from closing. This problem, in addition to being extremely time consuming, led to a leakage in the valve of varying size during the experiments. As a result of this the experiments carried out in the 40 mm tube, shown in Table 13, were each done three times, while the experiments carried out in the 78 mm tube, shown in Table 12, were only done once.

Table 12: Initial conditions for experiments carried out in the 78 mm tube.

Experiment	Pressure [barg]	Layer height [mm]	Particle diameter [μm]
1	1	10	≤ 106
2	2	10	≤ 106
3	3	10	≤ 106
4	4	10	≤ 106
5	5	10	≤ 106
6	1	30	≤ 106
7	2	30	≤ 106
8	3	30	≤ 106
9	4	30	≤ 106
10	5	30	≤ 106
11	1	50	≤ 106
12	2	50	≤ 106
13	3	50	≤ 106
14	4	50	≤ 106
15	5	50	≤ 106
16	1	10	212 - 300
17	2	10	212 - 300
18	3	10	212 - 300
19	4	10	212 - 300
20	5	10	212 - 300
21	1	30	212 - 300
22	2	30	212 - 300
23	3	30	212 - 300
24	4	30	212 - 300
25	5	30	212 - 300
26	1	50	212 - 300
27	2	50	212 - 300
28	3	50	212 - 300
29	4	50	212 - 300
30	5	50	212 - 300

Table 13: Initial conditions for experiments carried out in the 40 mm tube.

Experiment	Pressure [barg]	Layer height [mm]	Particle diameter [μm]
31	1	10	≤ 106
32	2	10	≤ 106
33	3	10	≤ 106
34	4	10	≤ 106
35	5	10	≤ 106
36	1	30	≤ 106
37	2	30	≤ 106
38	3	30	≤ 106
39	4	30	≤ 106
40	5	30	≤ 106
41	1	50	≤ 106
42	2	50	≤ 106
43	3	50	≤ 106
44	4	50	≤ 106
45	5	50	≤ 106

9   Experimental results

A series of experiments with particle beds were conducted in the 78 mm and the 40 mm pressure chambers and recorded with a high speed camera. As the recordings were studied, the particle beds showed behaviour that resembles the behaviour of fluidizing beds with bubbles of different sizes forming.

Levenspiel [15] makes a review of fluidized bed reactors and their different flow regimes. In a fluidized bed reactor, a fluid is passed through a solid granular material at such velocities that the bed will behave like a fluid. Different gas/solid contact regimes are described:

- **Fixed Bed**: The air is flowing through the bed without fluidizing it. There are no throughflow of particles.

- **Bubbling fluidized bed (BFB)**: The air flows through the fluidized bed in bubbles without throughflow of particles.

- **Turbulent fluidized**: Much like the bubbling fluidized bed, except the gas flows through the solids in streaks and channels and small parts of the solids may flow up and out of the reactor.

- **Fast fluidized**: Has a lean mixture of gas and particles in the core of the bed and a dense mixture by the walls. Throughflow of particles.

- **Pneumatic conveying**: The reactor has a lean mixture of particles and gas everywhere with throughflow of particles.

Geldard [10] studied how different kinds of solids behave when fluidized and came up with the Geldard classification. This states that the behaviour of solids fluidized by gases falls into four recognizable groups, A, B, C and D, characterized by the density difference between the solid and the fluid and the mean particle size. Group A consists of particles with small mean diameter and/or a low particle density. Characteristics of beds in this category is that they expand considerably before bubbling commences. Bubbles in category B starts to form slightly above minimum fluidization velocity and the bed expansion is small. Group C consists of particles that are in any way cohesive. They are difficult to fluidize, as the solids clump, and rise as slugs. The gas rises in channels. The last group, group D, consists of beds with large exploding bubbles and low bed voidage. Particles in this group are liable to spout.

The difference between the fluidized bed reactors described by Levenspiel [15] and the experiments conducted here, is mainly the mechanism of gas flow. In a fluidized bed reactor the gas is passed through the solid material, normally from a porous plate below the solids. In the experiments conducted here, the gas that fluidizes the solids is stored between the solids from the start. When the rarefaction wave arrives, the pressurized gas expands and starts to flow towards the section of the chamber with lower pressure. This creates, like the gas in the fluidized bed reactors, a gas flow that initiates what resembles fluidization of the bed of particles.
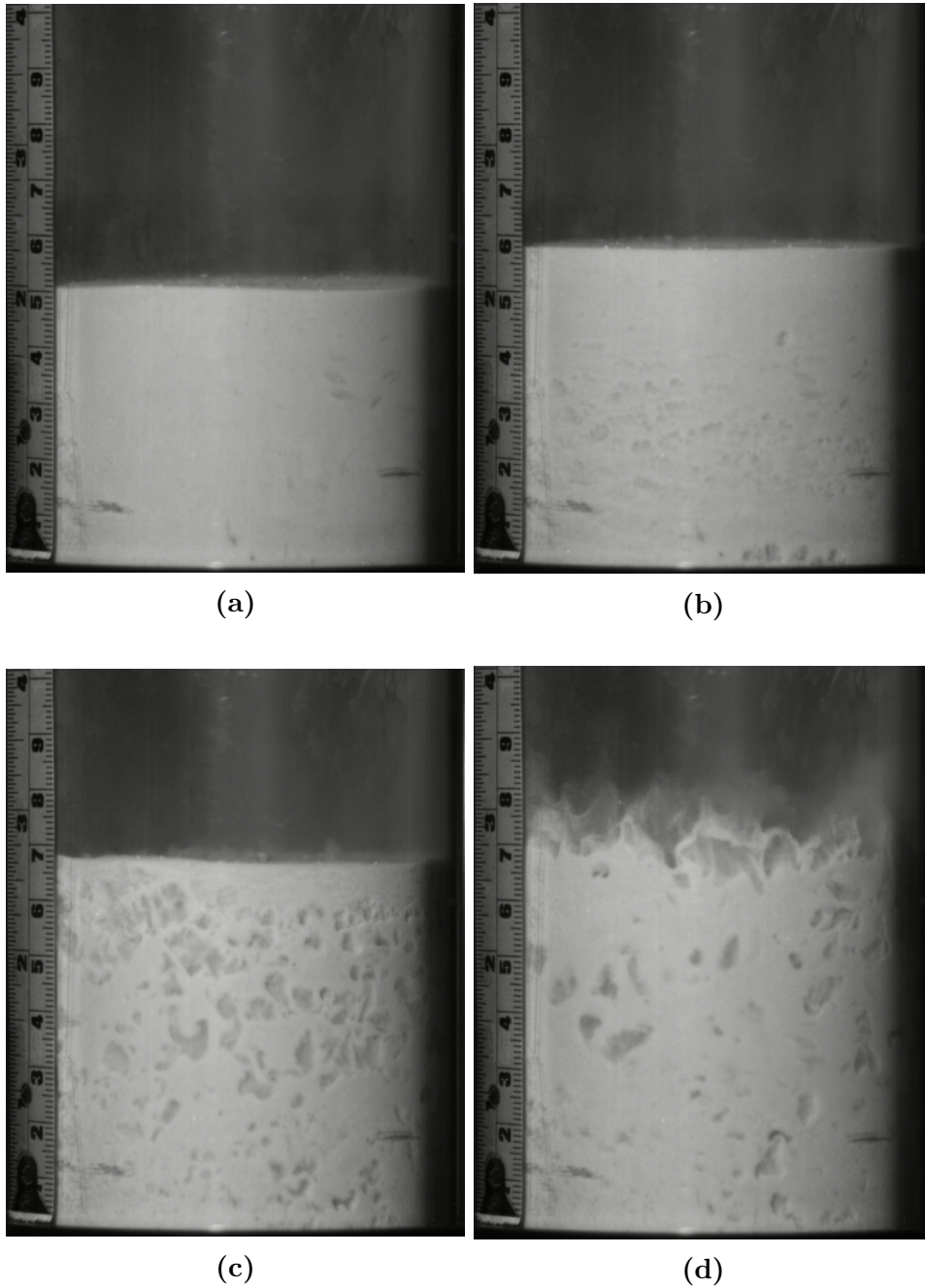
Figure 28: Experiment in geometry two, pressure chamber with diameter 78 mm, with glass beads of size ≤ 106 μm in a dust layer of height 50 mm and pressure of 1 barg. Subfigure (a) is a snapshot of the recorded video just before arrival of the rarefaction wave. In (b), bubbles of visible size are starting to form and the dust layer is rising. Large bubbles have formed in (c), and the surface of the layer is about to enter the violent state displayed in (d).

Figure 28 shows different states during an experiment in geometry two with beads of diameter ≤ 106 μm, bed height 50 mm and pressure 1 barg. From the initial state in Subfigure (a) to the moment visible bubbles have started to form in (b), the bed has expanded approximately 8 mm vertically. In Subfigure (c), the bubble phase and the emulsion phase is clearly visible, and the bed has expanded to around 68 mm. This is the point in time just before the bubbles break through the surface and spouting the particles in to the air above the bed. From here on this bed height is referred to as the breakthrough height.

(a)   (b)
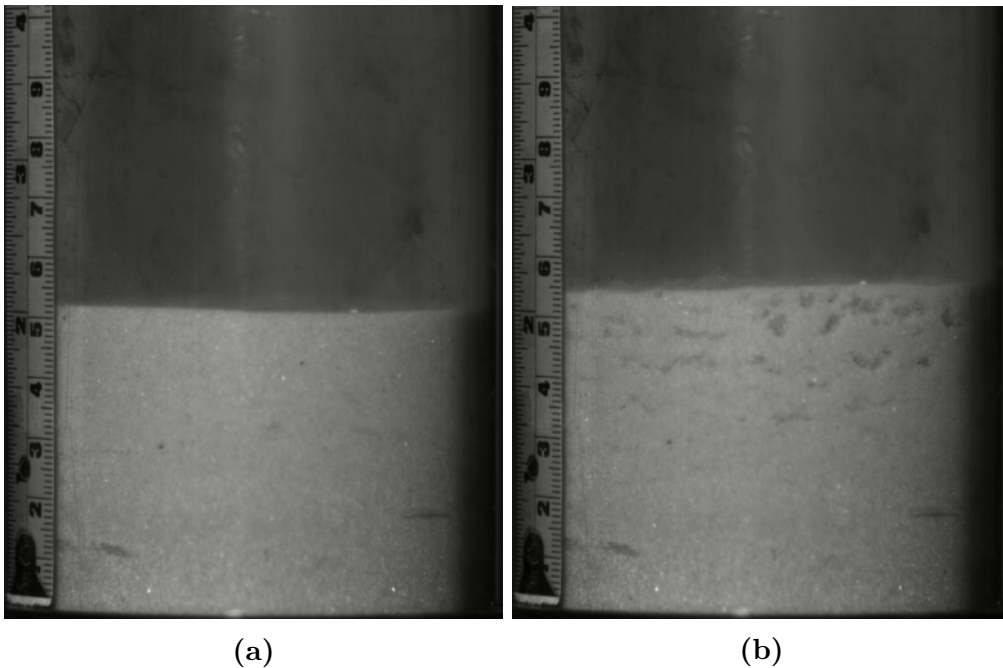
Figure 29: Experiment in geometry two, pressure chamber with diameter 78 mm, with glass beads of size 212 μm $-$ 300 μm in a dust layer of height ≈ 50 mm and pressure of 5 barg. Subfigure (b) shows the moment of maximum visible bubble size.

Figure 29 shows experimental results for geometry two with glass beads of size 212 μm $-$ 300 μm in a dust layer of height ≈ 50 mm and pressure of 5 barg. Visually, the particle bed looks much coarser than in the experiment with smaller beads (Figure 28). The bubbles are formed and reaches maximum size almost instantly after initiation of bed movement. Compared to the experiments with smaller beads, the bubbles are much smaller.
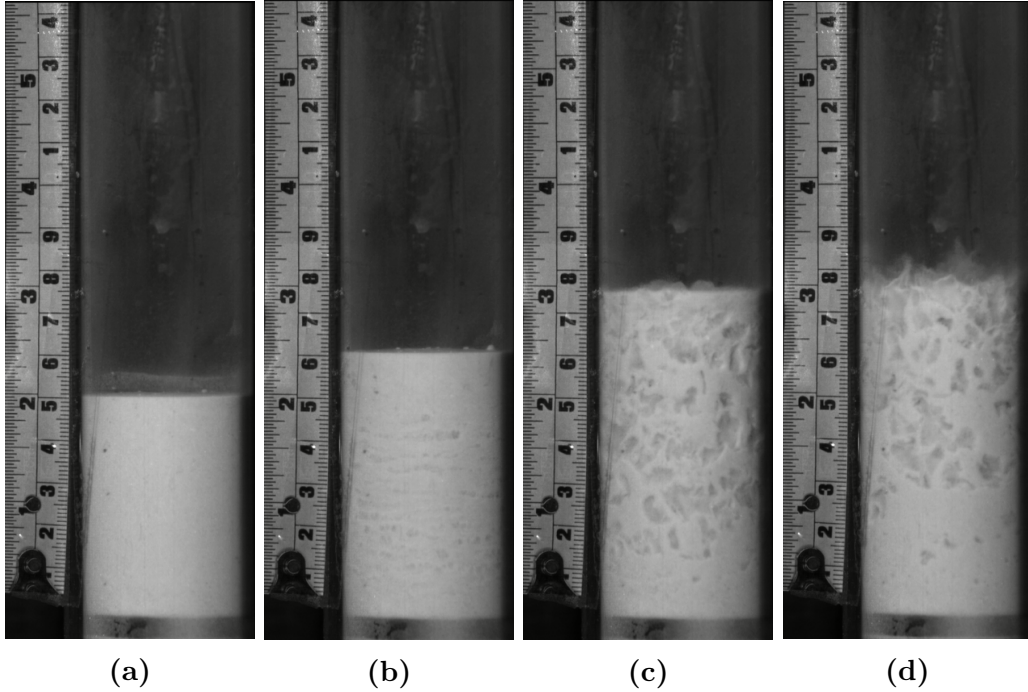
Figure 30: Experiment in the 40 mm pressure chamber with dust diameter ≤ 106 μm, dust layer height 50 mm and pressure 1 barg. In Subfigure (a), the rarefaction wave has arrived and initiated movement of the dust. In Subfigure (b), bubbles of visible size are starting to form. Subfigure (c) shows large bubbles shortly after breakthrough. In Subfigure (d) the dispersion of dust is at a maximum.

Figure 30 and Figure 31 shows experiments with small beads in geometry three with pressures of 1 barg and 5 barg, respectively. As can be seen in Subfigure (d) in both cases, the maximum dust dispersion is much greater in the experiment with 5 barg. However, looking at Subfigure (c) in Figure 30 and Subfigure (b) in Figure 31, one can observe that the bubble breakthrough occurs at approximately the same height independent of pressure. This is discussed further in Section 10.
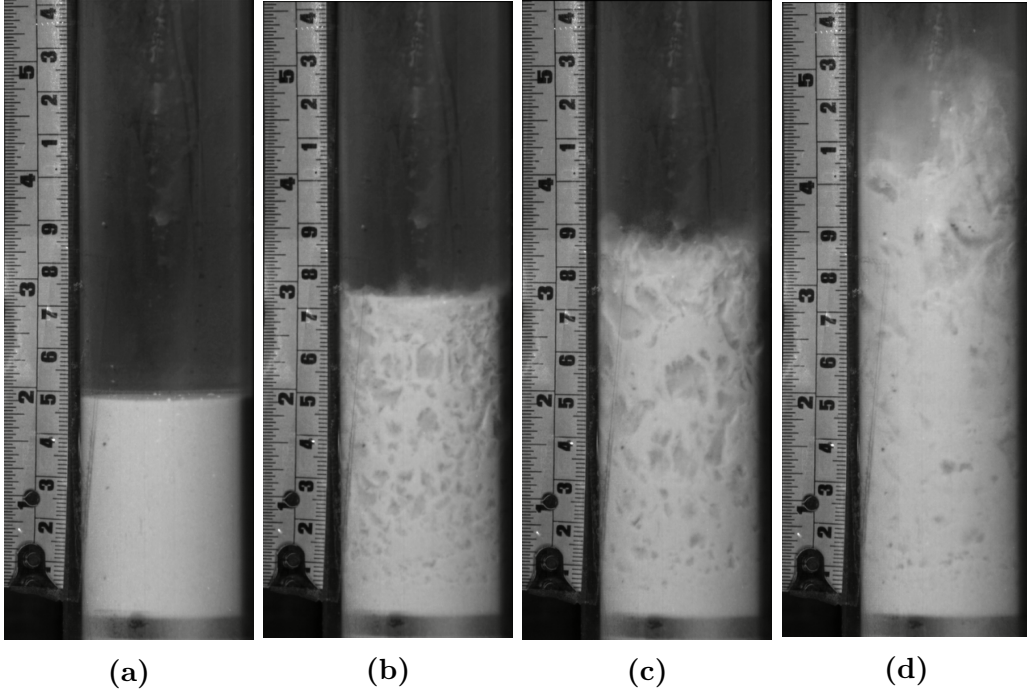
Figure 31: Experiment in the 40 mm pressure chamber with dust diameter ≤ 106 μm, dust layer height 50 mm and pressure 5 barg. In Subfigure (a), the rarefaction wave has arrived and initiated movement of the dust. Subfigure (b) shows breakthrough at 74 mm. In (c), the diameter of the visible bubbles is at a maximum. In Subfigure (d) the dispersion of dust is at a maximum.

If it is assumed that for these experiments the valve has reached its maximum capacity, and maximum mass flow rate out of the valve is obtained, a simple calculation can be made. If a maximum mass flow rate is obtained, it can be assumed constant with the same value for both geometry two and geometry three:

$$A_2 \cdot \rho \cdot v_2 = A_3 \cdot \rho \cdot v_3,$$

$$v_3 = \left(\frac{r_2}{r_3} \right)^2 \cdot v_2,$$

$$v_3 = 3.8 \cdot v_2. \tag{20}$$

Here, A is the cross sectional area of geometry two and three, and v is the mass flow velocity of air in the geometries. Equation (20) shows that, if the assumptions made are correct, one can expect a gas flow velocity in geometry

three nearly four times the value of the velocity in geometry two. Another observation that indicates that the gas velocity in geometry three is greater than in geometry two, has to do with the relative speed between the bubbles and the emulsion. By studying Figure 30 and Figure 28, it looks as the size of the bubbles are approximately the same. Levenspiel [15] explains that in a bubbling fluidized bed the rise velocity of the bubble depends only on the size of the bubble. This indicates that the velocity of the bubbles in both experiments are approximately the same. Since the particle bed, or the emulsion, in Figure 30 is reaching a higher altitude than the particle bed in Figure 28 before bubble-breakthrough, it could mean that the relative velocity between the bubbles and the gas rising in the emulsion is higher in geometry two. In other words; the gas rising through the emulsion in the experiments in geometry three has a higher velocity, giving the particles in the emulsion a higher velocity.

If the beds in the experiments with small glass beads were to be classified according to the Geldart classification [10] and the fluidized bed reactors described by Levenspiel [15], they would be described as a mix between a bubbling fluidized bed and a turbulent fluidized bed with a Geldart classification somewhere between A and B. This is because the air flows as bubbles through the emulsion, but eventually breaks to a more turbulent regime with particles flowing out through the valve. The density difference and particle diameter puts the particles in the A classification, but the almost instant bubble formation suggests they belong in category B.

10 Simulations compared with experimental results

Earlier in the thesis, t_0 was defined as the moment the rarefaction wave first interacted with the dust layer. For the experiments, and simulations 8 - 19, the time of particle bed movement, t_m, was defined as the point in time where movement in the dust layer was detected. This point was for the simulations found at the point in time when the volume fraction in the probe at the top of the dust layer started to change. In section 9 the term "breakthrough" of the bubbles was defined. In this section a series of plots of lifting height and lifting velocity as a function of pressure is shown. The height of the lifted dust is here defined as the difference between the height of the bubble breakthrough and the start-height. The velocity of the layer is calculated from the lifting height, t_m, and the time of bubble breakthrough.

The following are comparisons between the experiments conducted and simulations 8 - 19. For the experiments, two kinds of plots are shown; lifting height of the dust as a function of initial pressure, and lifting velocity as a function of initial pressure. An attempt to recreate these from the simulations is also presented. The point of breakthrough is difficult to determine for the simulations. This is solved by assuming the concentration of the particle beds in the experiments are homogeneous at the point of breakthrough. Since we know the start-height of the particle bed, the volume fraction at start, particle volume and breakthrough height of the experiments, the volume fraction at breakthrough can be approximated (see table 14).

Table 14: Breakthrough volume fractions calculated from experiments.

Simulation	Volume fraction at breakthrough
8	0.43
9	0.43
10	0.40
11	0.41
12	0.39
13	0.38
14	0.47
15	0.35
16	0.42
17	0.42
18	0.41
19	0.41

The volume fractions in Table 14 are from here on referred to as "volume fractions calculated from experiments". They are calculated from values with an already high uncertainty and are therefore not very reliable. In addition to plots based on these values, plots based on a volume fraction of 0.1 are also shown.

Lifting height as a function of pressure - geometry comparison
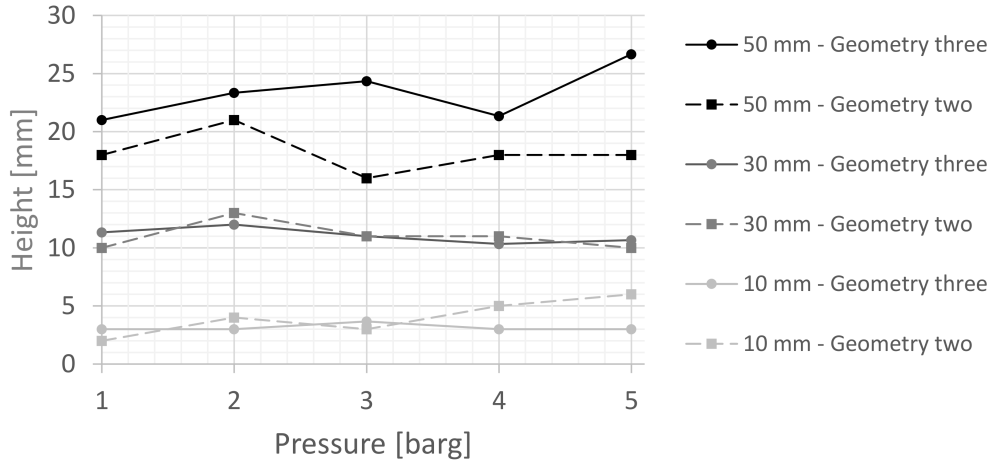
Figure 32: Lifting height as a function of pressure. Experiments conducted with beads of size ≤ 106 μm in geometry two with diameter 78 mm and in geometry three with diameter 40 mm.

Figure 32 shows the lifting height of the particle bed for experiments conducted with small glass beads in geometry two and geometry three. The most visible trend is that lifting height increases with layer depth. The dotted lines represent experiments conducted in geometry two with a diameter of 78 mm. These experiments were only carried out once each, and are therefore considered less reliable than the experiments in geometry three, which were carried out three times each. This is probably the reason why the dotted lines have a more oscillating behaviour than the smooth solid lines, which are from experiments in geometry three. For the experiments with 10 mm and 30 mm dust layers, increasing the pressure does not seem to increase the layer lifting. For the 50 mm dust layer in geometry two the lifting height is not changing much for the different pressures. The experiments with 50 mm dust layer in geometry three on the other hand could show a trend of slightly increasing lifting height for increasing pressure. In addition to the clear increase in lifting height for increased layer depths, the experiments with 50 mm dust layer shows that decreasing the chamber diameter will increase the layer lifting.
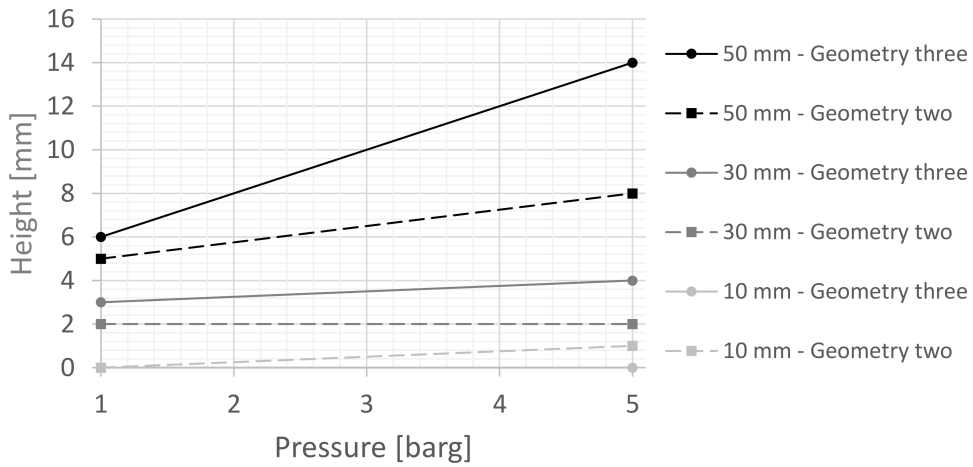
Figure 33: Height of dust with a volume fraction calculated from experiments as a function of pressure for simulation 8 - 19.
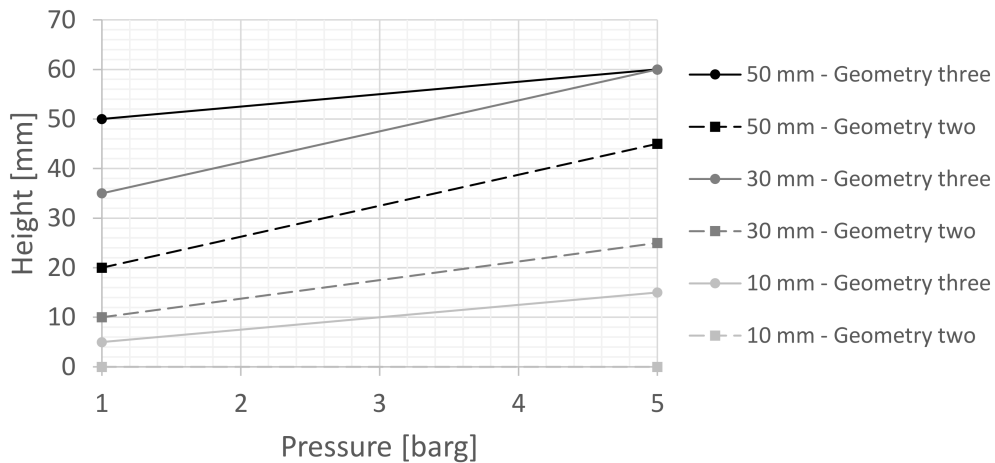
Figure 34: Height of dust with a volume fraction of 0.1 as a function of pressure for simulation 8 - 19.

Figure 33 shows lifting height as a function of time for the simulations, based on the volume fraction calculated from experiments (see Table 14). Figure 34 is the same plot, except based on a volume fraction of 0.1. As in the experiments, the simulations show an increase in lifting height with an increase in layer depth. The most interesting trend is that in Figure 34, the lifting height seem to increase with increasing pressure, while in Figure 33 the trend looks more like the trend for the experiments, where the lifting height only

increases with increasing pressures for the deep layer depths.

Lifting height and lifting velocity as a function of pressure - particle comparison
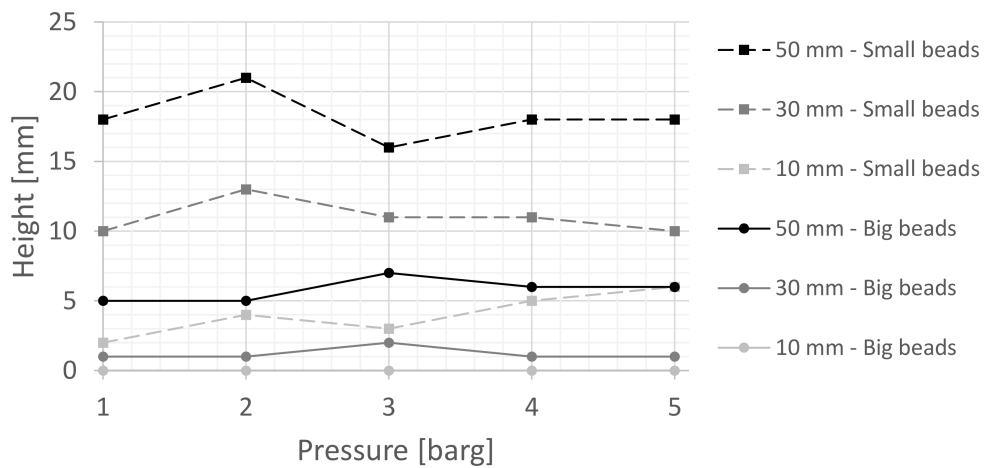
Figure 35: Height as a function of pressure. Experiments conducted with beads of size ≤ 106 μm compared to beads of size 212 μm $- 300$ μm (big beads) in geometry two with diameter 78 mm.
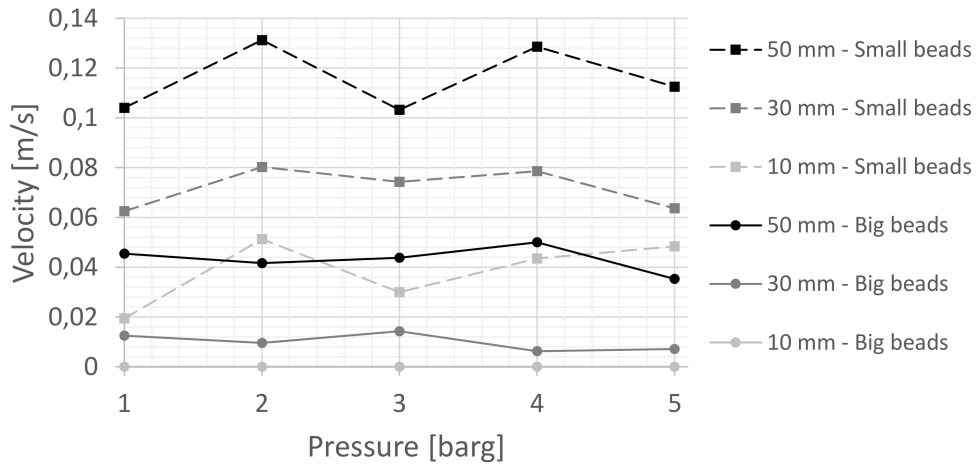
Figure 36: Velocity as a function of pressure. Experiments conducted with beads of size ≤ 106 μm compared to beads of size 212 μm $- 300$ μm (big beads) in geometry two with diameter 78 mm.

A comparison between the particles with a diameter ≤ 106 μm (small beads) and the particles with a diameter 212 μm $- 300$ μm (big beads) is shown i Figure 35 and in Figure 36. All the experiments were conducted in geometry two. The big beads are represented by the solid lines, while the small beads are represented by the dotted lines.

The experiments with the big beads in Figure 35 show the same as pointed out earlier; that the lifting height increases with increasing dust layer depth. For the experiments with the big beads in a 10 mm layer, no movement is detected at all. With a layer depth of 30 mm lifting heights between 1 and 2 mm are observed. For 50 mm layer depth, lifting heights are ranging from 5 to 7 mm, around one third of the heights observed for the small beads.

The plots in Figure 36 shows the velocities for the different particle sizes in the experiments compared to each other. In general, the velocity seems to be increasing with increasing layer depth and decreasing particle size.

Lifting velocity as a function of pressure - geometry comparison
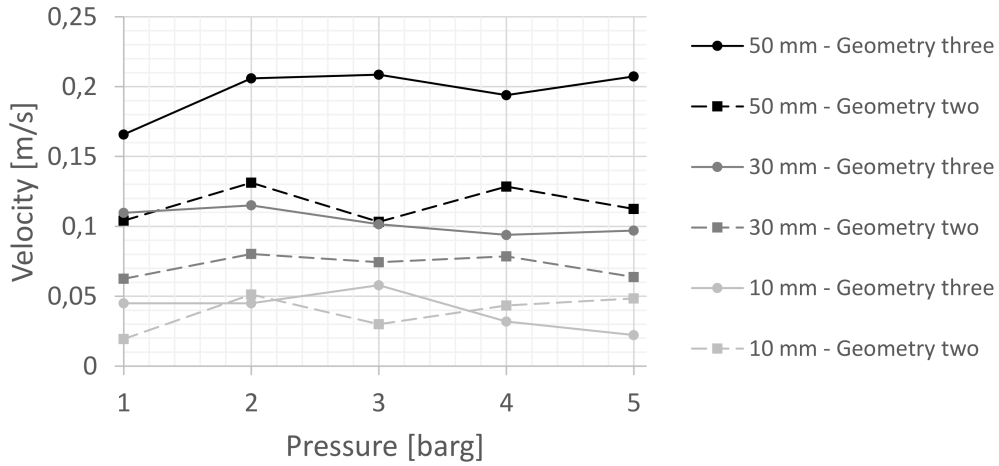
Figure 37: Velocity as a function of pressure. Experiments conducted with beads of size ≤ 106 μm in geometry two with diameter 78 mm and geometry three with diameter 40 mm.

The velocity plots for the experiments with different pressure chamber diameter in Figure 37 supports the hypothesis from Section 9, that the velocity of the particle bed, or emulsion, increase with decreasing diameter. This is true for layer depths of 50 mm and 30 mm, but for the experiments with 10 mm layer depth such a claim can not be made. The experiments also shows that increasing the layer depths increases the velocity. An increase in pressure does not seem to affect the velocity.

68
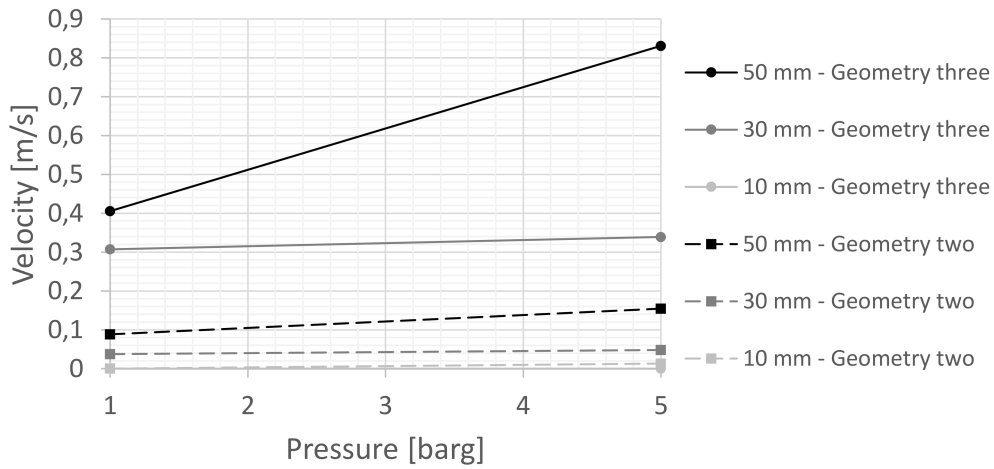
Figure 38: Velocity of dust with a volume fraction calculated from experiments as a function of pressure for simulation 8 - 19.
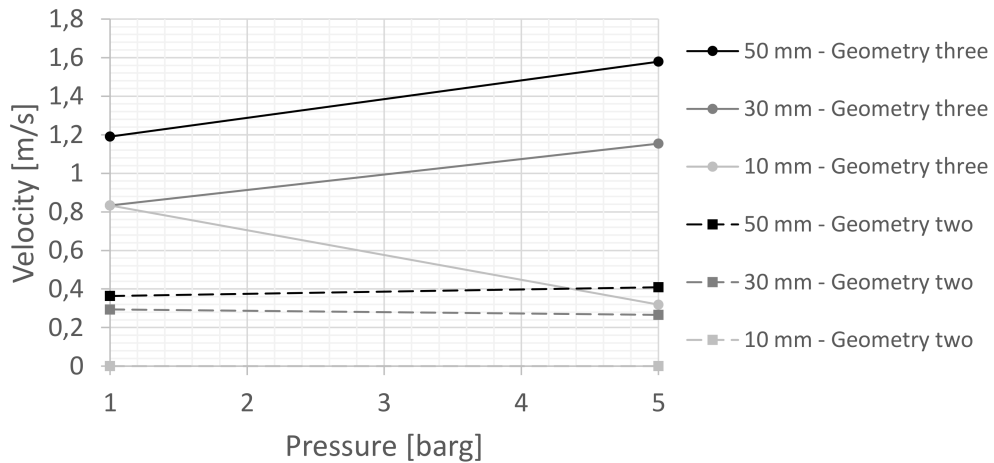
Figure 39: Velocity of dust with a volume fraction of 0.1 as a function of pressure for simulation 8 - 19.

Figure 38 and Figure 39 shows particle velocity plotted against pressure for the simulations. Figure 38 is based on the volume fractions calculated from experiments (see Table 14) while Figure 39 is based on a volume fraction of 0.1. In Figure 38, the velocities does not seem to vary much with pressure, except for the simulations with 50 mm layer depth where the velocities nearly doubles from 1 barg to 5 barg. In Figure 39, the dependency on pressure seem to be much more present in the simulations for geometry three than for

69

geometry two.

Overall, the velocity plot of the experiments shows a lifting velocity ranging from around 0.025 m/s to over 0.2 m/s. The simulation plots both have velocities around 0 m/s, because in the 10 mm layer height simulations very little movement was detected. The plots based on volume fractions from the experiments shows the highest velocity at 0.8 m/s while the highest velocity for the plot based on a volume fraction of 0.1 is almost 1.6 m/s.

11 Height-time investigation of experiments and simulations

For simulations 8 - 19, surveillance points were placed 5 mm over the end of the pressure chamber, and every 5 mm until 110 mm (see figure 8 in Section 5.2). Like for simulations 3 - 7, the height of the dispersed dust could be plotted as a function of time. To create similar plots for the experiments, a measuring tape was placed at the side of the pressure chamber and the experiments were recorded with a high speed camera. This way the dust dispersion could be studied in slow motion and as the dust cloud propagated through the pressure chamber the time at each 5 mm point was noted. What makes this section different from Section 10, is that in Section 10 the breakthrough height and time was noted so the average velocity could be calculated, while in this section the height and time of the highest visible dust every 5 mm was noted. The highest visible dust was until breakthrough the top of the expanding particle bed, after which the highest visible dust was in the form of dust clouds or gatherings of dust spouted into the air by bursting bubbles.

As mentioned in Section 10, t_F was set to the point in time the movement in the dust layer was detected. The time of dust cloud arrival at each probe was set to be when the concentration exceeded $1.0 \cdot 10^{-4}$ for all the simulations, as well as 0.01, 0.1 and 0.2 for a few chosen simulations. For simulation 13, which corresponds to experiment 45 (50 mm layer height, small beads and 5 barg in geometry three), a similar method as described in Section 10 was used. As the bed of particles expands upwards, the average volume fraction decreases. This is because the volume of particles is the same, but the volume the bed expands into increases. Since the height of the particle bed was recorded, the approximate volume fraction for every 5 mm could be calculated. However, the volume fractions calculated in this way turned out to be larger than for the dust in the simulation. Therefore, the volume fraction was set to decrease gradually from 0.4 to 0.01 for the plot named "VF decreasing" in Figure 40. The height of the experiments exceeded for some of the cases the 110 mm mark, which was the location of the highest probe in the simulations. Therefore plots that exceeded this limit were cropped so that it was easier to compare with the simulations, but can be seen in their full extent in Appendix A.
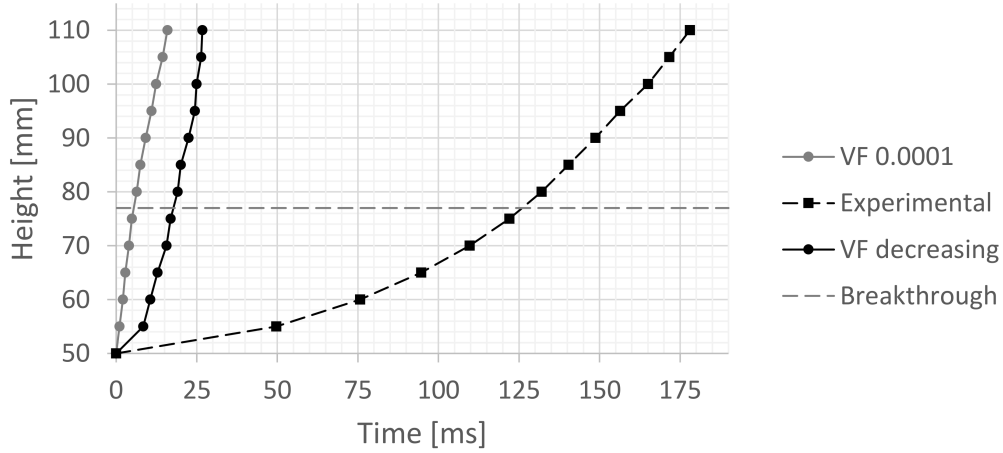
Figure 40: Height as a function of pressure for simulation 13 compared with experiment.

Figure 40 shows the results from simulation 13 compared to experiment 45, with pressure 5 barg in the 40 mm pressure chamber. The dotted line with a constant value of 77 mm represents the breakthrough height for the experiment. The dotted line with squares is the experimental results, the grey line with circles is based on a volume fraction of 0.0001 from the simulation and the black solid line with circles is from the simulation and based on the decreasing volume fraction described earlier.

What can be seen from the experimental plot is that, first of all, the time from t_F to the dust reaches a height of 110 mm is far longer for the experiment than for the simulation. Second, the acceleration of the dust is different in the different curves. The curve for the dust of constant volume fraction 0.0001 is at its steepest, i.e. the dust cloud has the highest velocity, at the start, while for the experimental curve and the simulation curve with decreasing volume fraction, the velocity is increasing over time. This makes the simulation plot based on the decreasing volume fraction more similar to the experimental plot. Still, a cloud of volume fraction 0.0001 is moving in front of the rest of the dust, making the model inaccurate.
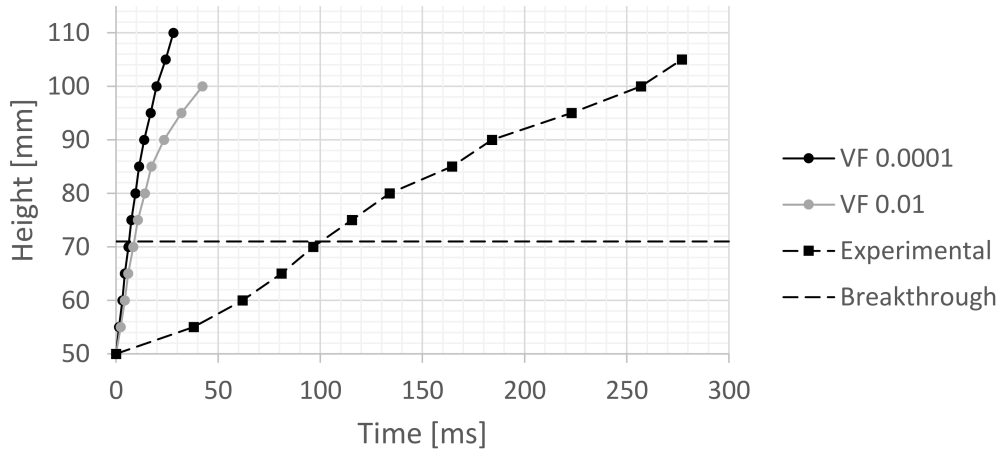
Figure 41: Height as a function of pressure for simulation 12 compared with experiment.

Figure 41 shows the height of the lifted dust as a function of time for simulation 12 and the experiment conducted in the 40 mm chamber with a dust height of 50 mm and pressure of 1 barg. As in Figure 40 the volume fraction of 0.0001 is plotted, in addition to a plot based on a volume fraction of 0.01. Here, the velocity decreasing over time is clearly visible. By studying the experimental plot and the line marking the breakthrough, one can observe that after the breakthrough the experimental curve goes from being convex to concave. This indicates that the dust has its maximum velocity around the breakthrough point.

Overall, the average velocity of the simulations is higher than for the experiments. This probably has to do with the fact that the solenoid valve is used for the experiments, while an extremely simplified model of the valve, a constriction in the cylinder, is used in the simulations. A narrower geometry was first used in the simulations, but because of the extreme computational time, it was discarded in favour of the current one. The bigger opening in the simulations is making the air inside the pressure chamber evacuate faster, dragging the dust with it at a higher velocity.

The dust velocity in the simulations is at a maximum at the start of the dispersion, then decreases over time. This can be seen in Appendix C. The dust velocity in the experiments increases from the start until at least the point of breakthrough, where the velocity either increases, decreases or a behave in a turbulent way. This can be seen in Appendix A.

73
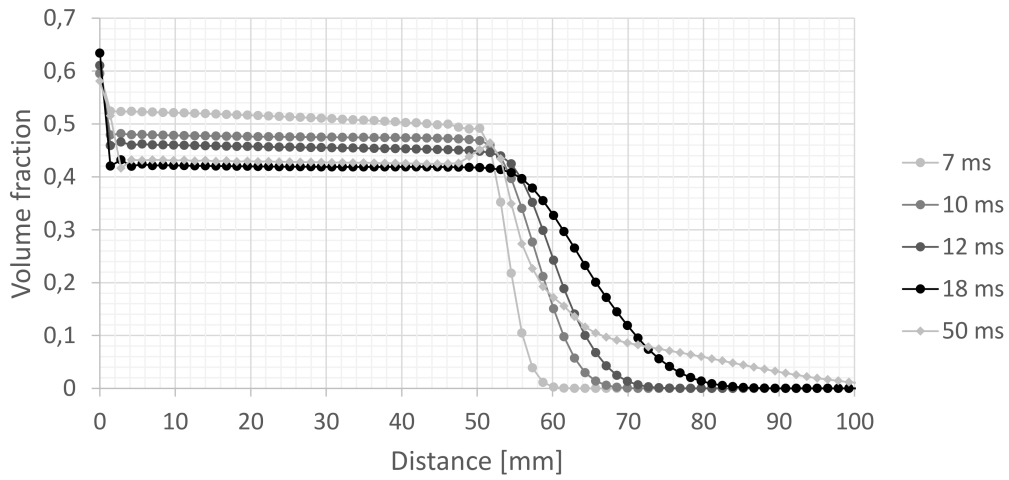
Figure 42: Volume fraction as a function of distance through the pressure chamber at different times for simulation 12.

Figure 72 shows the volume fraction as a function of distance through the chamber for different points in time. This plot, and the rest of the volume fraction plots in appendix C, shows that in the bottom part of the layers the volume fraction increases to a value between 0.6 and 0.7. This could indicate that there is something wrong with the volume fraction - particle diameter relationship. In the experiments the diameter of the particles is $\leq 106\ \mu m$ while for the simulations the diameter is $106\ \mu m$.

74

12   Conclusion

A three dimensional CFD-model of the interaction of a rarefaction wave with a layer of dust was created with the computational fluid dynamics software STAR-CCM+. Two CFD-models were investigated using different energy models; simulation 1 with the segregated fluid temperature model and simulation 2 with the segregated fluid isothermal model. They were run and compared to the exact Riemann solution. Simulation 1 was in good correspondence with the exact Riemann solution, while the propagation speed for the waves in simulation 2 was too low. For both simulations a "smearing" of the head and tail of the waves was observed. According to [21] the this is caused by first-order time-discretization. Reducing the time-step was shown to decrease this problem, at the cost of longer computational time. The consequence of solving with a constant temperature through the segregated fluid isothermal model was ultimately a higher air velocity behind the rarefaction wave.

The experiments conducted by Medvedev et al. [19] were recreated in STAR-CCM+ using both energy models from the verification section. The simulations were compared to each other, as well as to previous experiments by Medvedev et al. and simulations by Klemens et al. [13]. The simulations with different energy models both showed nearly identical initial dust lifting in the height-time plot, but the simulation with the isothermal energy model had, according to the volume fraction plot, a much greater dust dispersion. The latter was possibly connected to the higher air velocity behind the rarefaction wave. Ultimately, the energy intended to heat the air and the particles was instead converted to drag force leading to an overestimation of dust dispersion for the isothermal simulation.

Despite showing a slightly high dust lifting velocity in the height-time plot, the simulations were in good correspondence to the experiments by Medvedev et al. However, the "smearing" of the rarefaction waves led to the point in time of rarefaction wave arrival at the dust layer being defined earlier than it should. Correcting this error would probably lead to a shift of around 0.87 ms to the left in a plot of dust lifting height as a function of time after rarefaction wave arrival.

One simulation was run with a closed end geometry. In this scenario, the shock wave was reflected from the closed end opposite from the dust layer. The results indicates that reflected shock waves and its accompanying flow of gas have a suppressing effect on dust dispersion caused by rarefaction waves.

Through experiments it was shown that a particle bed placed at the closed end of a pressure chamber shows similarities to a fluidized particle bed when exposed to a rarefaction wave created from a sudden depressurization of the chamber through a solenoid valve placed at the opposite end. After the rarefaction wave arrived at the particle bed, the bed expanded upwards with visible bubbles forming and expanding inside, eventually breaking through the top of the bed and spouting dust further up the chamber. The size of the formed bubbles was shown to be dependent of the size of the particles, with smaller particles giving larger bubbles. The height at which the bubbles broke through the particle bed surface was defined as breakthrough height.

The breakthrough height was shown to vary with the diameter of the pressure chamber and the diameter of the particles. For layers of lower height the breakthrough height did not seem to vary with pressure. For the 50 mm dust layer the breakthrough height seemed to increase slightly with increasing pressure.

The dispersion of the dust cloud following the breakthrough was shown to increase with increasing pressure and smaller pressure chamber diameter.

A height-time plot of the dispersed dust in the experiments showed that the velocity curve had a convex shape (velocity increasing) until breakthrough where the dust was entering a more turbulent state, giving the curve varying traits.

An attempt was made to recreate the experimental setup in the numerical software STAR-CCM+. The simulation showed a dust lifting velocity way higher than the experiments. This was most likely because the solenoid valve was used for the experiments while an extremely simplified model of the valve, a constriction in the cylinder, was used in the simulations.

13 Further Work

Even though the results from the simulations were in good compliance with previous experiments, improvements can still be made. To create a model with as little "smearing" as possible, but with a shorter computational time is desirable.

An extension of the experiments conducted is also of interest. Both in terms of the observed phenomena of what resembles a fluidized bed and in terms of the mechanisms of dust dispersion due to rarefaction waves in general. An approach to what would happen to the particle bed if the experiments were conducted in a chamber of longer, or shorter, length can be made with emphasis on emulsion and gas velocity, breakthrough height and bubble characteristics. Experiments with dust with more given specifications, more precise equipment for pressure measurements and the use of pressure rupture panels should be considered. The use of pressure rupture panels would lead to a faster air evacuation of the pressure chamber and create a "cleaner" rarefaction wave.

It would also be interesting to conduct a numerical investigation of the phenomena of a particle bed showing similarities to a fluidized bed when exposed to a rarefaction wave.

References

[1] Turbulence modelling. `https://www.cfd-online.com/Wiki/Turbulence_modeling`, May 2017.

[2] John D Jr. Anderson. *Modern Compressible Flow With Historical Perspective.* McGraw-Hill, New York, third edition edition, 2003.

[3] Bürkert. Manual for Servo-assisted 2/2 way piston valve.

[4] Clayton T. Crowe, John D. Schwarzkopf, Martin Sommerfeld, and Yutaka Tsuji. *Multiphase Flows with Droplets and Particles.* CRC Press, second edition, 2012.

[5] John D. Anderson. *Computational Fluid Dynamics.* McGraw-Hill, 1995.

[6] Rolf K. Eckhoff. *Explosion Hazards in the Process Industries.* 2005.

[7] Sabri Ergun. Fluid flow through packed columns. *Chemical Engineering Progress*, 48:89–94, 1952.

[8] B. C. Fan, Z. H. Chen, X. H. Jiang, and H. Z. Li. Interaction of a shockwave with a loose dusty bulk layer. November 2006.

[9] B. Fletcher. The interaction of shock with a dust deposit. *J. Ohys. D; Appl. Phys.*, 9, 1976.

[10] D. Geldart. Types of Gas Fluidization. *Powder Technology*, 1973.

[11] J. H. Gerrard. An experimental investigation of the initial stages of the dispersion of dust by shock waves. 14, 1963.

[12] Ralph Jennings. Formosa Fun Coast explosion. `https://apnews.com/2d026cb0ecd94846a2a67fa8475b372c/fire-injures-scores-attending-party-taiwan-water-park`, June 2015.

[13] R. Klemens, P. Kosinski, and P. Oleszczak. Mathematical modelling of dust layer dispersion due to rarefaction waves. *archivum combustionis*, 22(1-2), 2002.

[14] R. Klemens, P. Zydak, M. Kaluzny, D. Litwin, and P. Wolanski. Dynamics of dust dispersion from the layer behind the propagating shock wave. *Journal of Loss Prevention in the Process Industries*, 19:200–209, 2006.

[15] Octave Levenspiel. *Chemical Reaction Engineering*. Third edition edition, 1999.

[16] Jan R. Lien and Gunnar Løvhøiden. *generell fysikk for universiteter og høgskoler*. Universitetsforlaget, 2001.

[17] Warren L. McCabe, Julian C. Smith, and Peter Harriot. *Unit Operations of Chemical Engineering*. McGraw-Hill, seventh edition, 2005.

[18] Robert J. McMillan. *Shock tube investigation of pressure and ion sensors used in pulse detonation engine research*. PhD thesis, Air Force Institute of Technology, 2004.

[19] S.P. Medvedev, J.H. Geng, and H. Grönig. Shock tube study of dust layer dispersion by rarefaction wave.

[20] STAR-CCM+. STAR-CCM+ user guide. 11.06.

[21] Eleuterio F. Toro. *Riemann Solvers and Numerical Methods for Fluid Dynamics*. Springer, 2nd edition.

[22] Hanna Utkilen, Boris V. Balakin, and Pawel Kosinski. Numerical study of dust lifting using the Eulerian-Eulerian approach. *Journal of Loss Prevention in the Process Industries*, 27:89–98, 2014.

[23] J. Warnatz, U. Maas, and R. W. Dibble. *Combustion*. Springer, 4 edition, 2006.

[24] C.Y. Wen and Y.H. Yu. Mechanics of Fluidization. 1966.

[25] A. A. Zhilin and A. V. Fedorov. Interaction of Rarefaction Waves with a Finite-Thickness Layer near a Rigid Boundary. Equilibrium Approximation. *Combustion, Explosion, and Shock Waves*, 43(5):607–615, 2007.

[26] Przemyslaw Zydak and Rudolf Klemens. Modelling of dust lifting process behind propagating shock wave. *Journal of Loss Prevention in the Process Industries*, pages 417–426, 2006.

Appendices

A   Additional figures from experiments
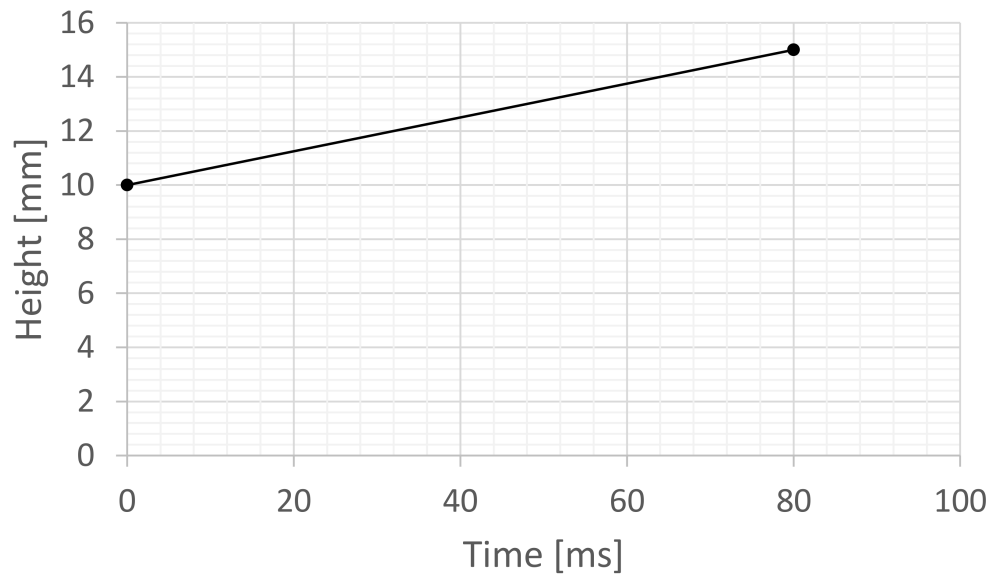
Figure 43: Dust lifting height as a function of time for experiment 8.
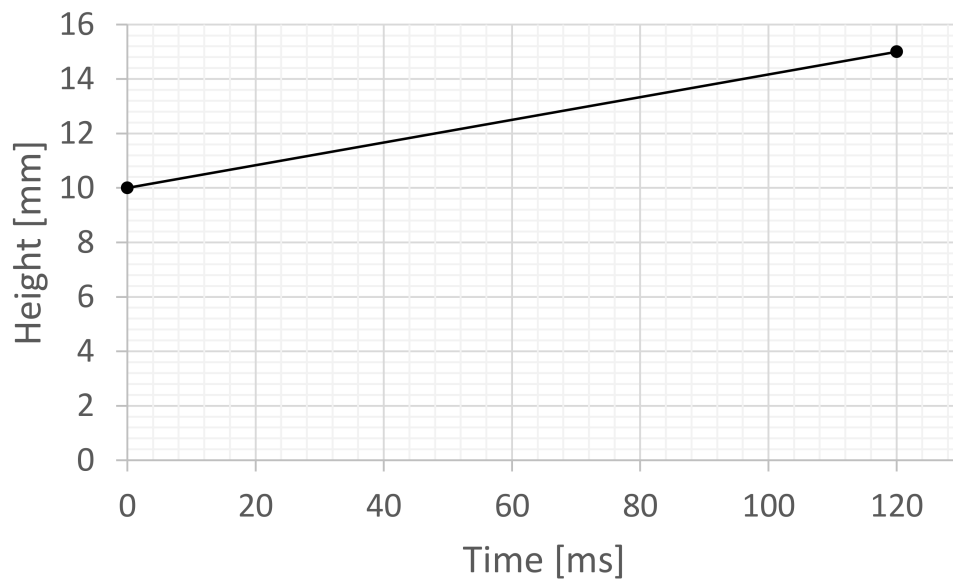
Figure 44: Dust lifting height as a function of time for experiment 9.
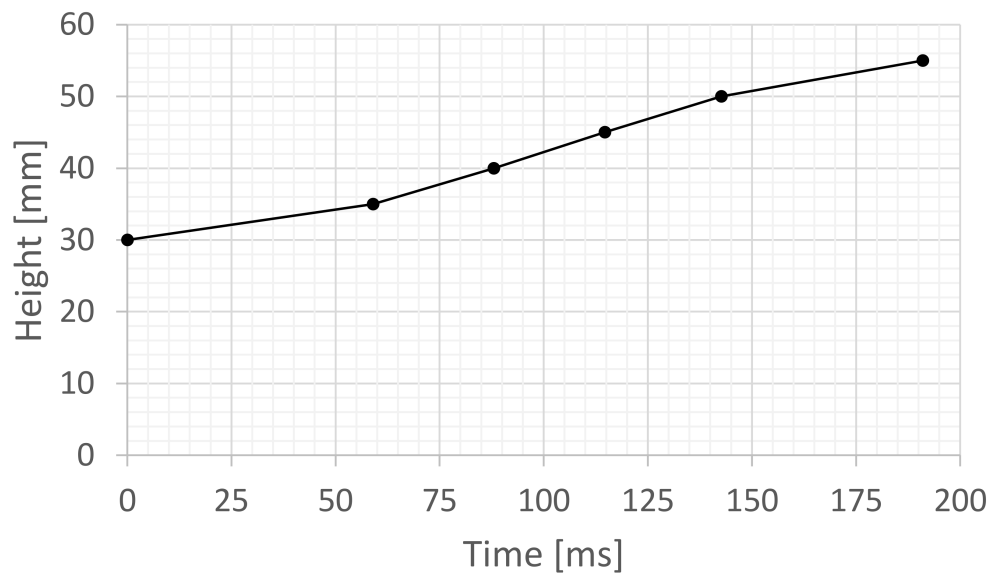
Figure 45: Dust lifting height as a function of time for experiment 10.
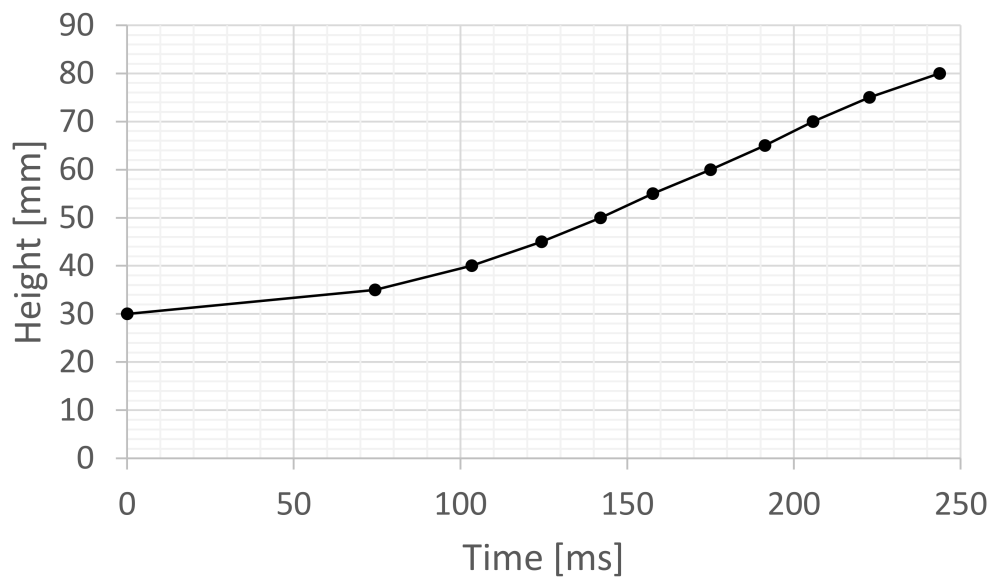
Figure 46: Dust lifting height as a function of time for experiment 11.
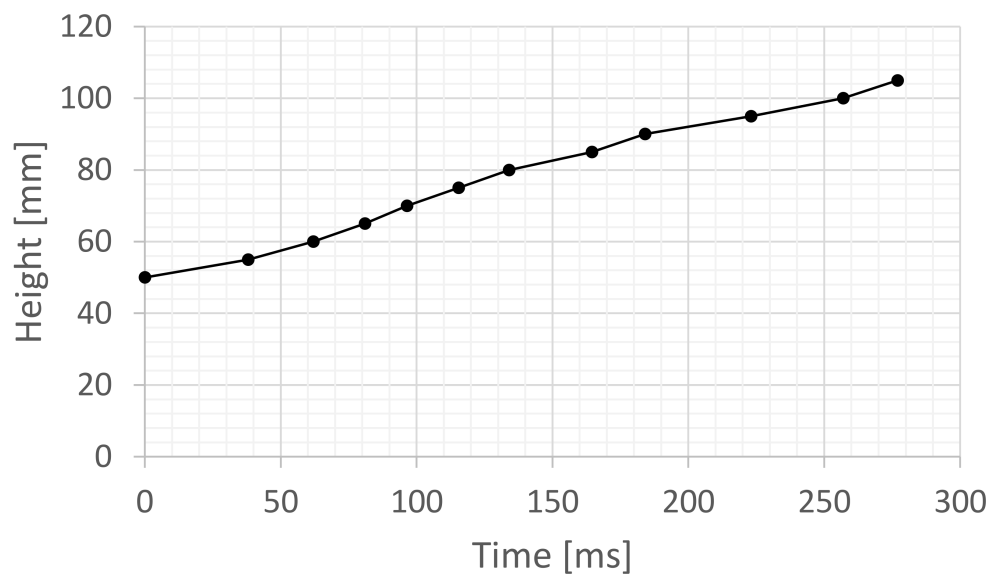
Figure 47: Dust lifting height as a function of time for experiment 12.
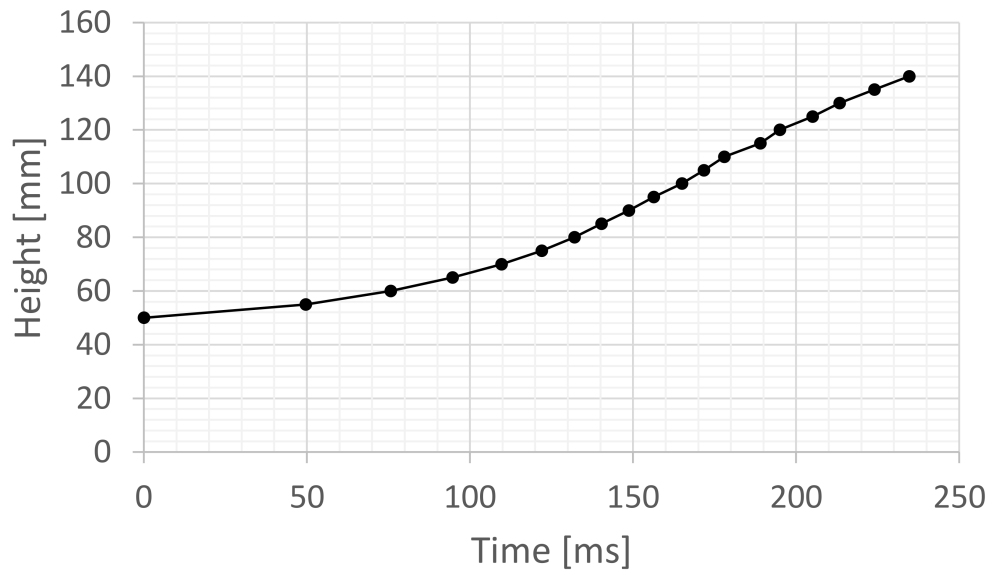
Figure 48: Dust lifting height as a function of time for experiment 13.
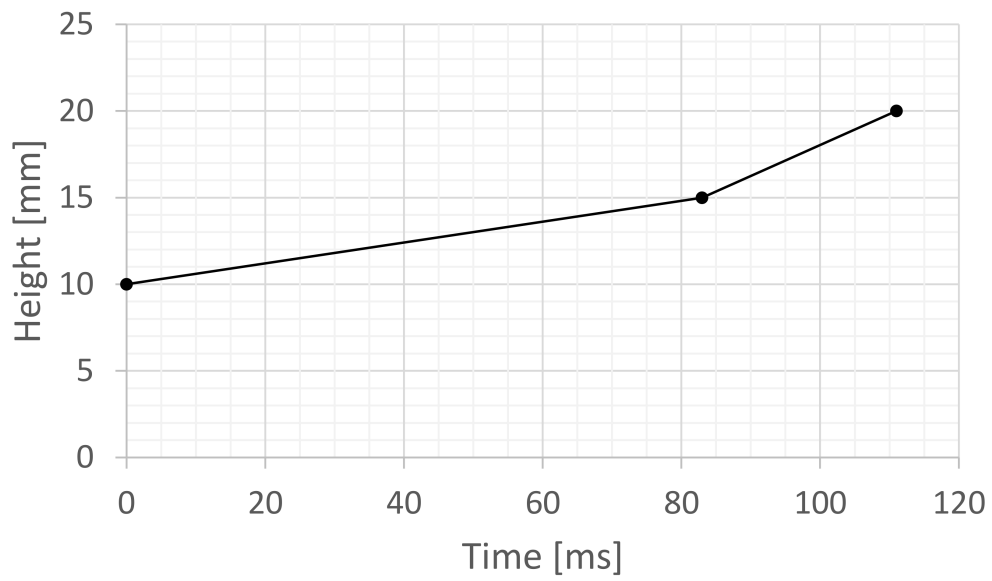
Figure 49: Dust lifting height as a function of time for experiment 14.
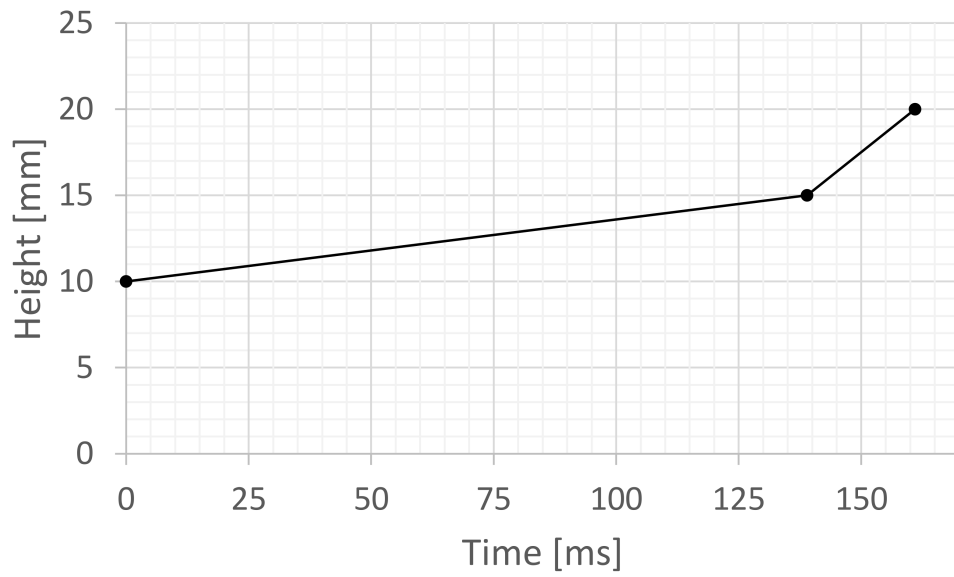
Figure 50: Dust lifting height as a function of time for experiment 15.
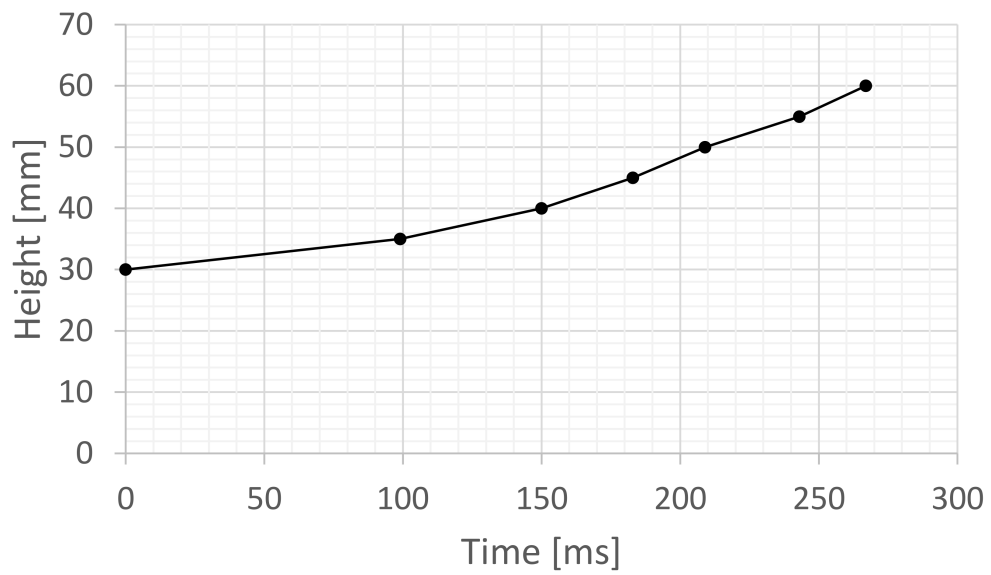
Figure 51: Dust lifting height as a function of time for experiment 16.
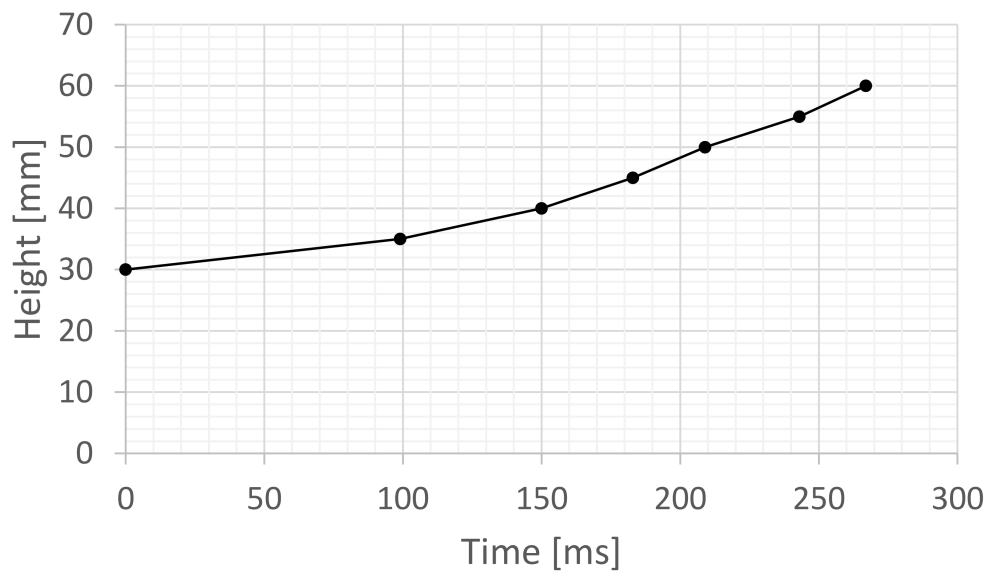
Figure 52: Dust lifting height as a function of time for experiment 17.
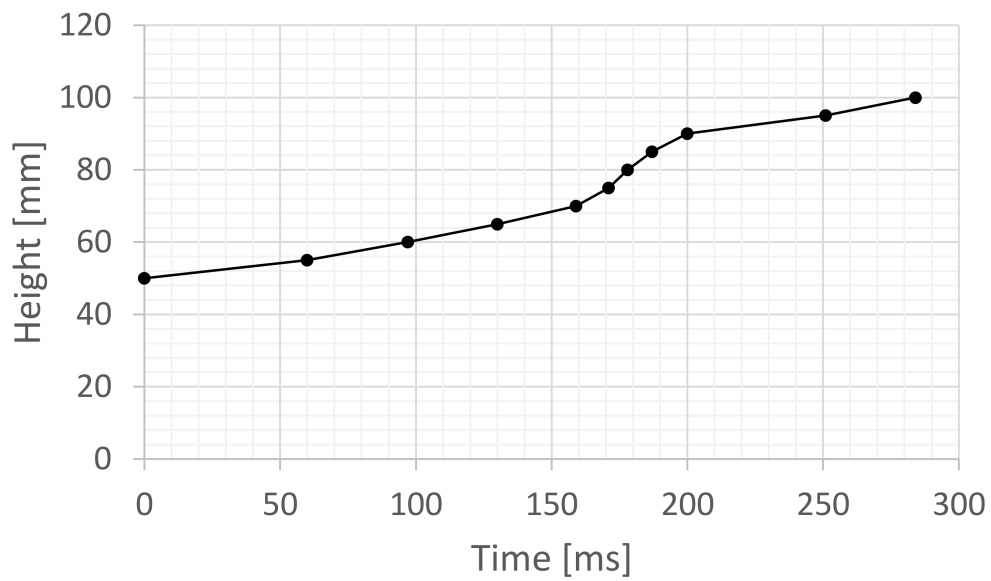
Figure 53: Dust lifting height as a function of time for experiment 18.
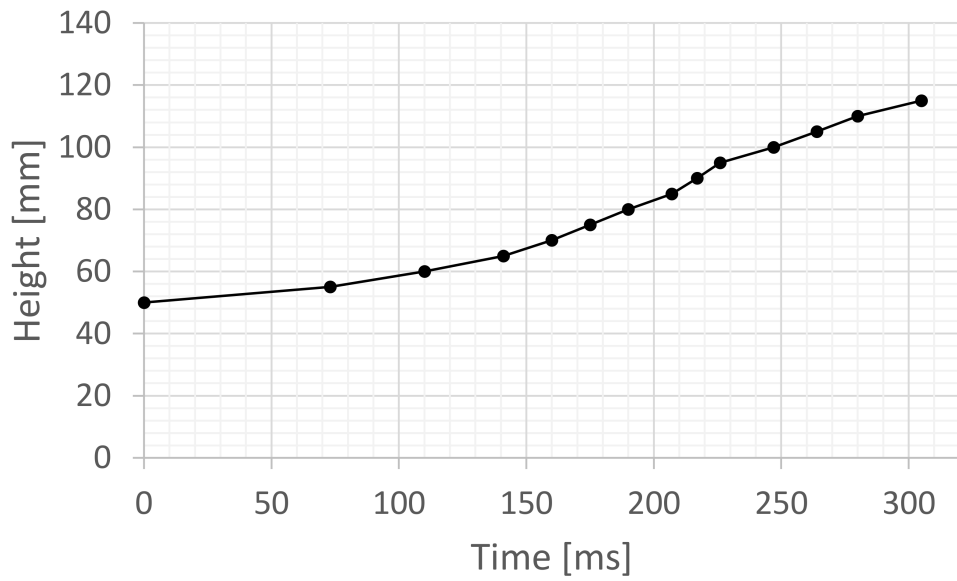
Figure 54: Dust lifting height as a function of time for experiment 19.

B   Additional figures from simulation 3 - 7
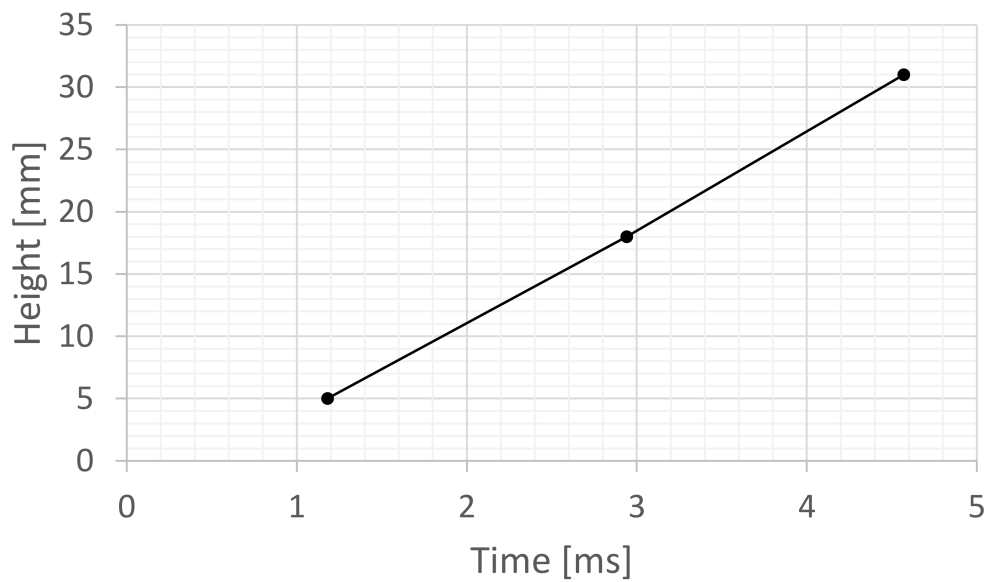
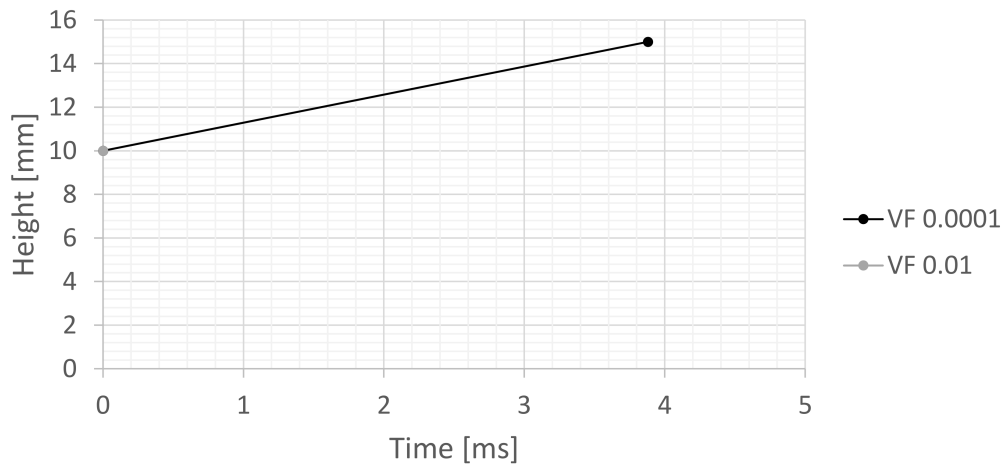**Figure 55:** Dust lifting height above initial dust bed as a function of time for simulation 3.
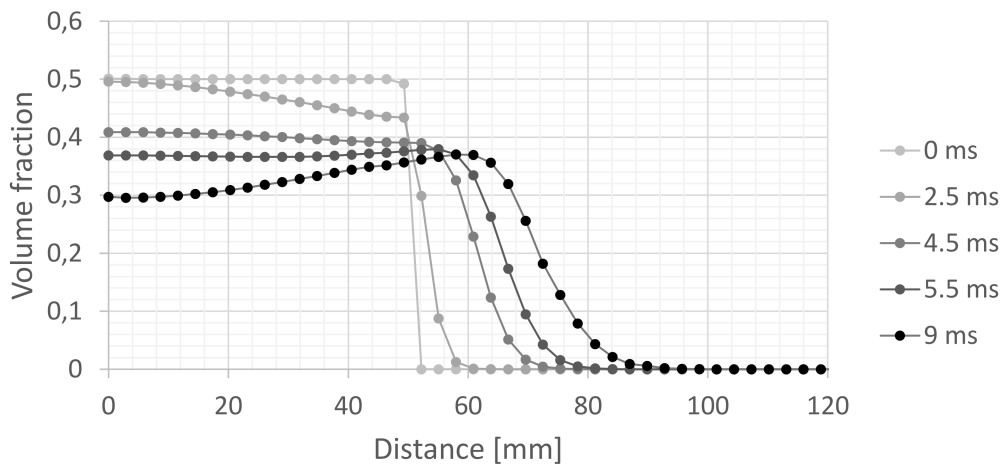
Figure 56: Volume fraction simulation 3.
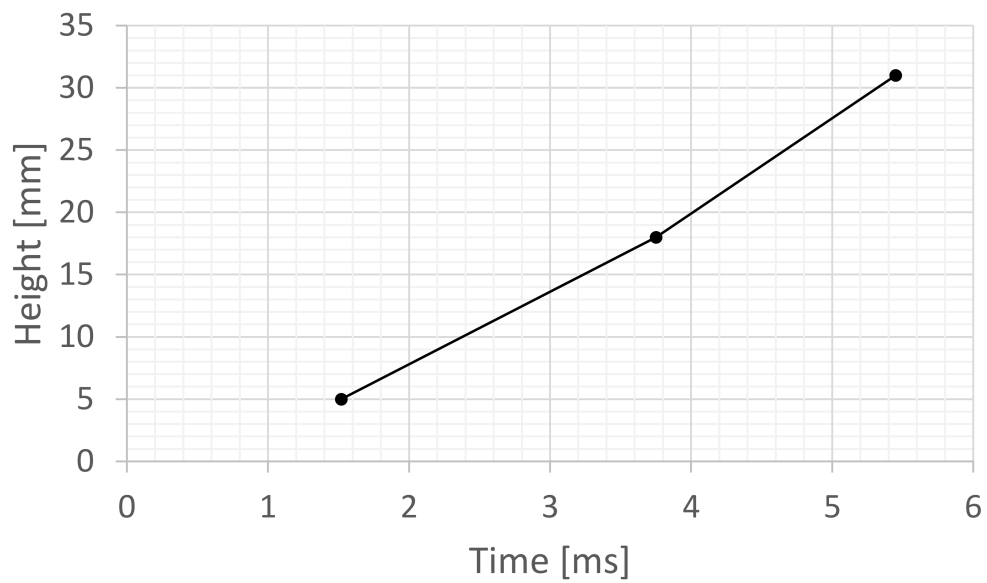
Figure 57: Dust lifting height above initial dust bed as a function of time for simulation 5.
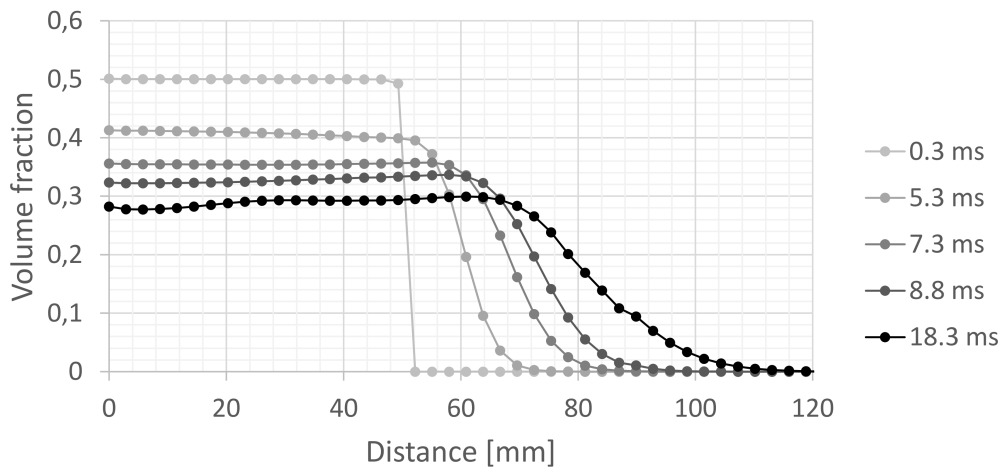
Figure 58: Volume fraction simulation 5.
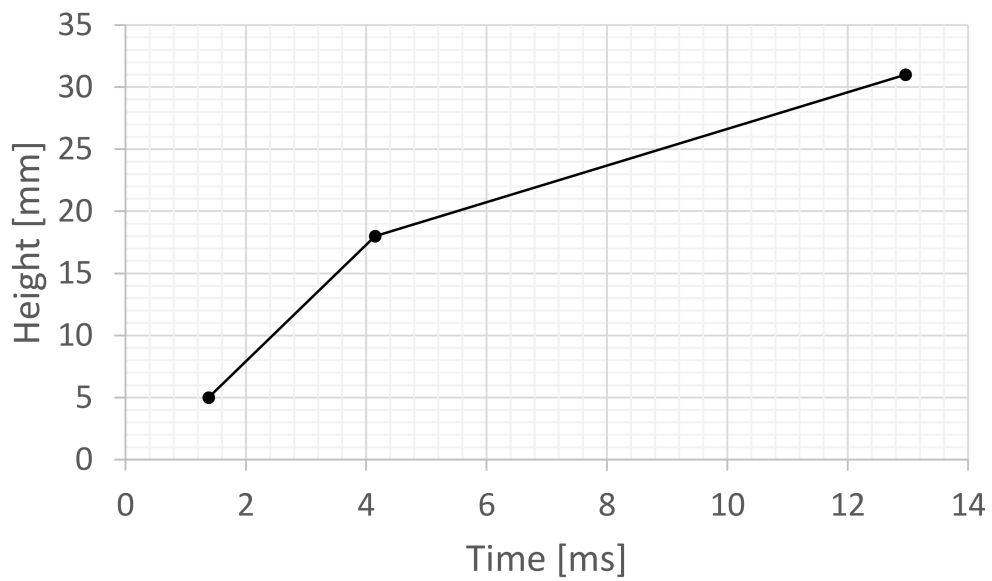
Figure 59: Dust lifting height above initial dust bed as a function of time for simulation 6.
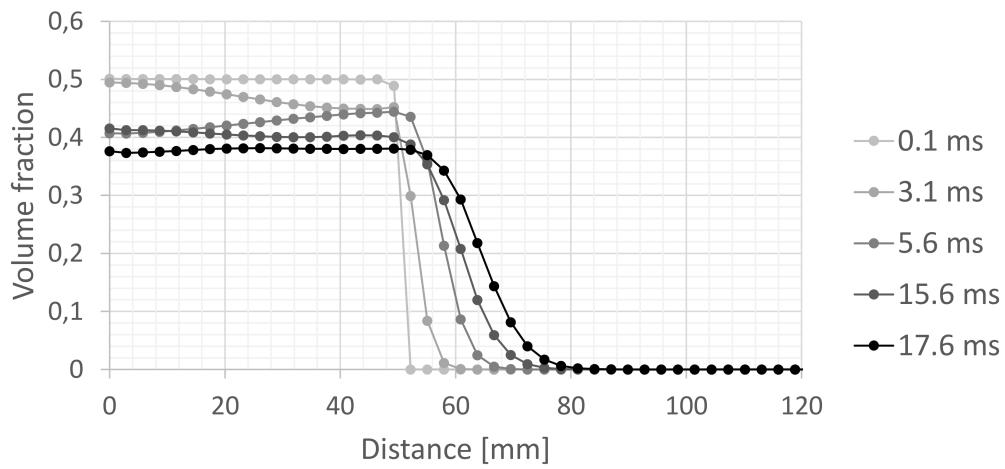
Figure 60: Volume fraction simulation 6.
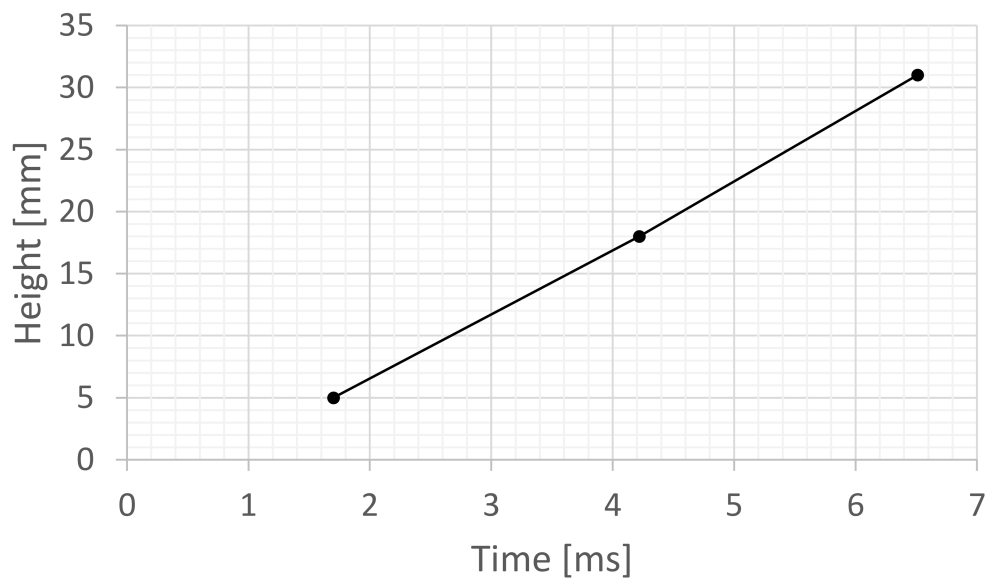
Figure 61: Dust lifting height above initial dust bed as a function of time for simulation 7.
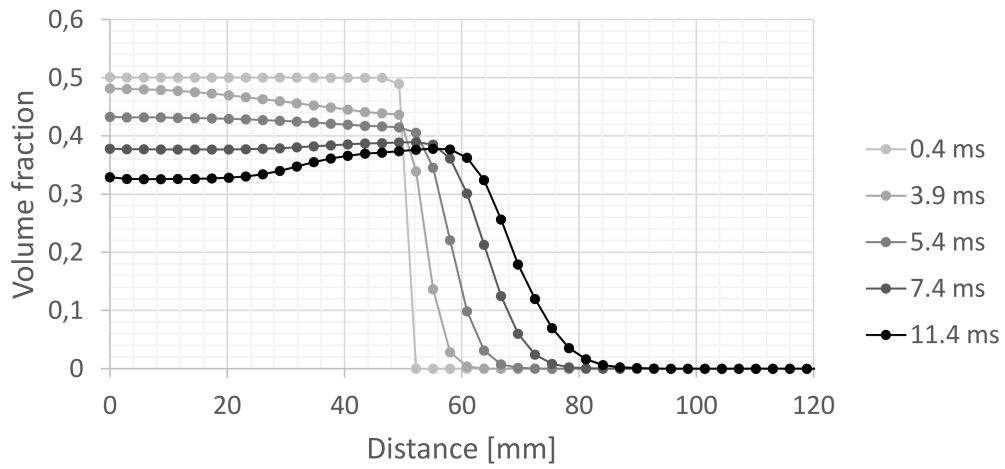
Figure 62: Volume fraction simulation 7.

C Additional figures from simulation 8 - 19
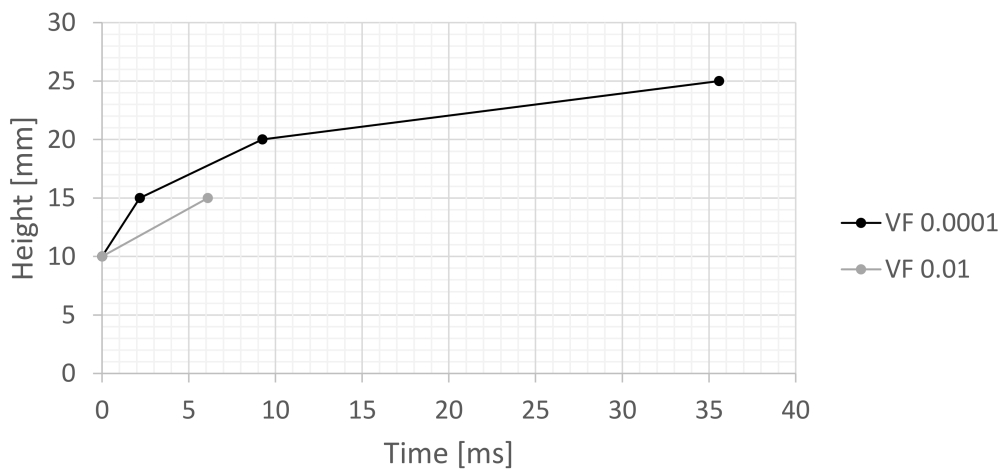
Figure 63: Dust lifting height above initial dust bed as a function of time for simulation 8.
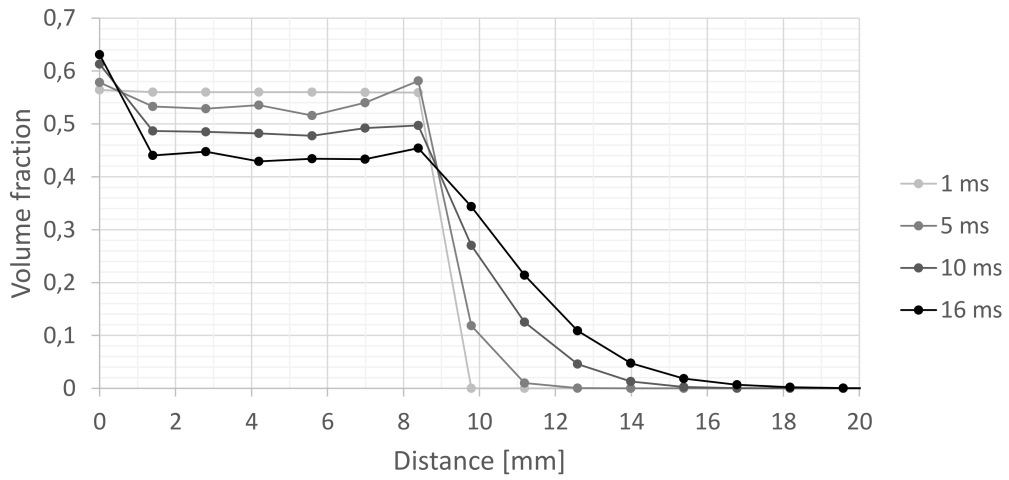
Figure 64: Volume fraction as a function of distance through the pressure chamber at different times for simulation 8.
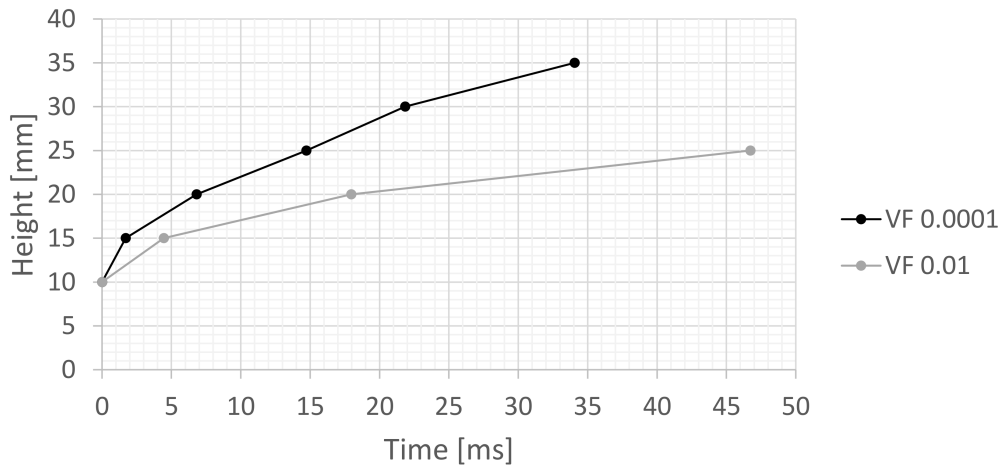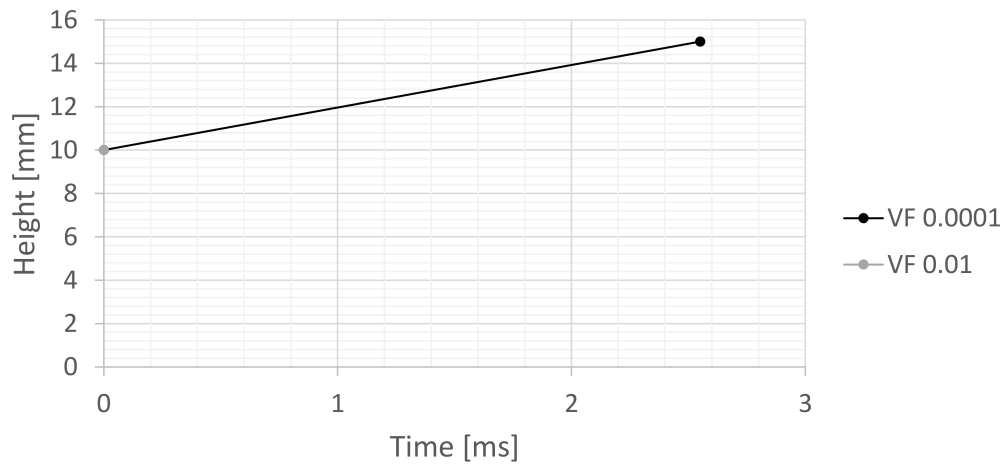

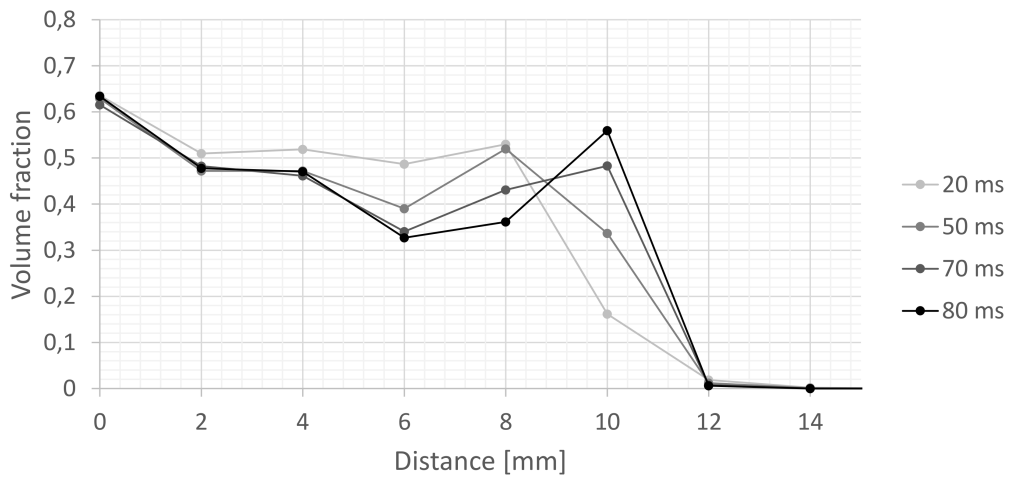**Figure 65:** Dust lifting height above initial dust bed as a function of time for simulation 9.
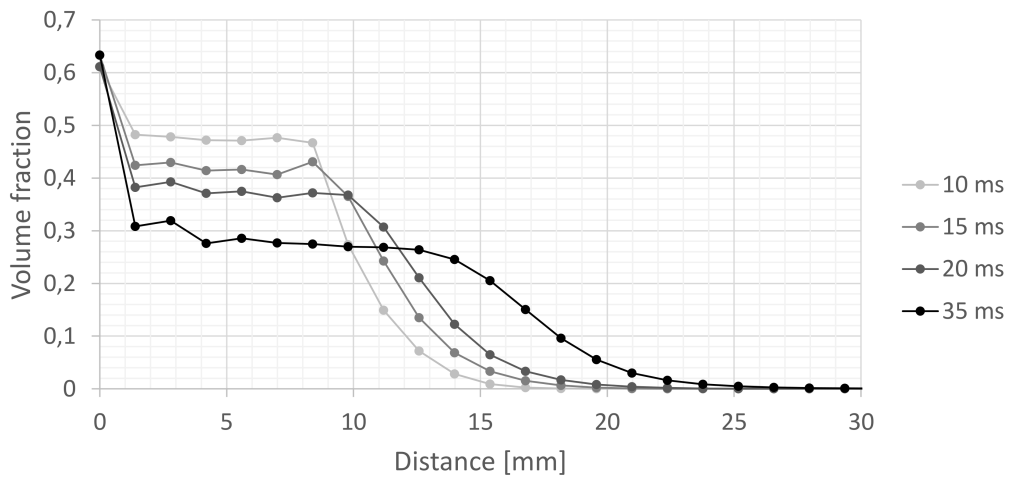
Figure 66: Volume fraction as a function of distance through the pressure chamber at different times for simulation 9.
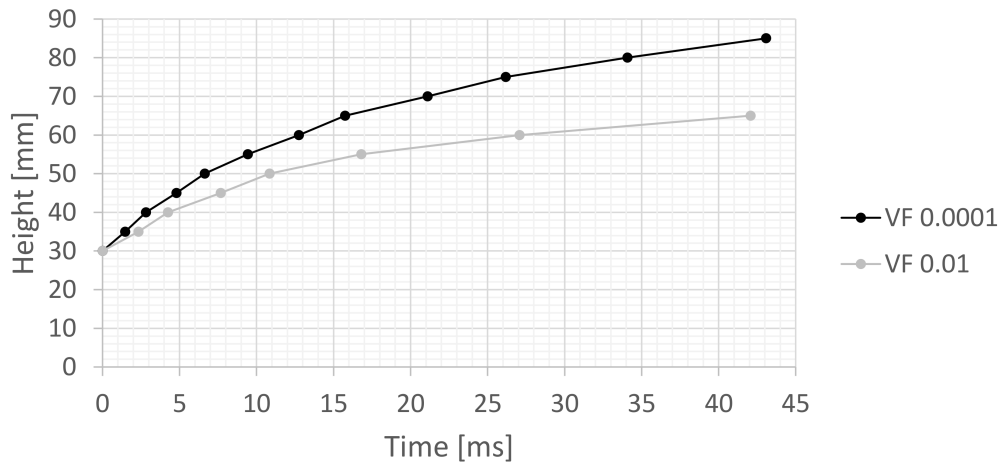
Figure 67: Dust lifting height above initial dust bed as a function of time for simulation 10.
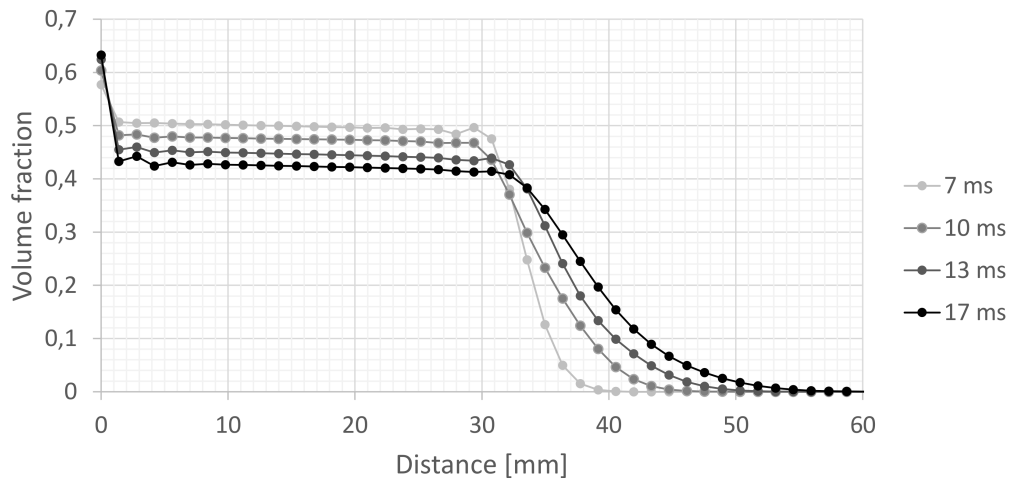
Figure 68: Volume fraction as a function of distance through the pressure chamber at different times for simulation 10.
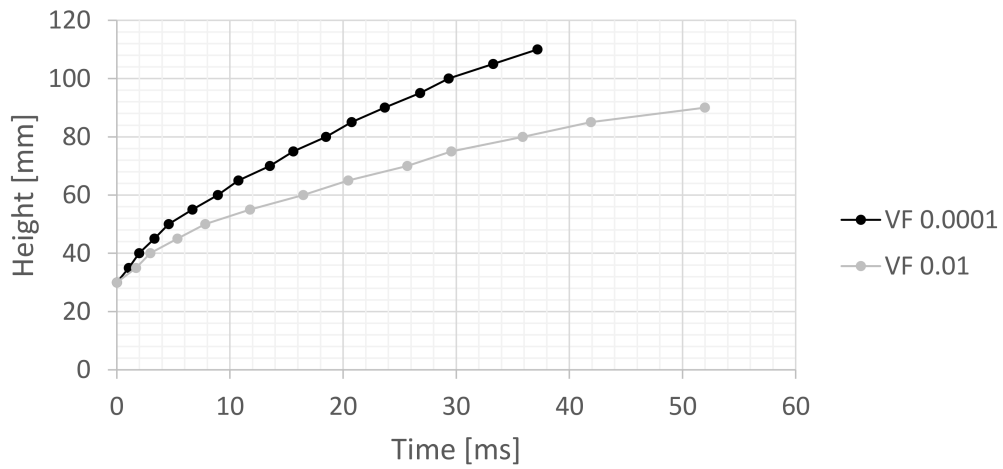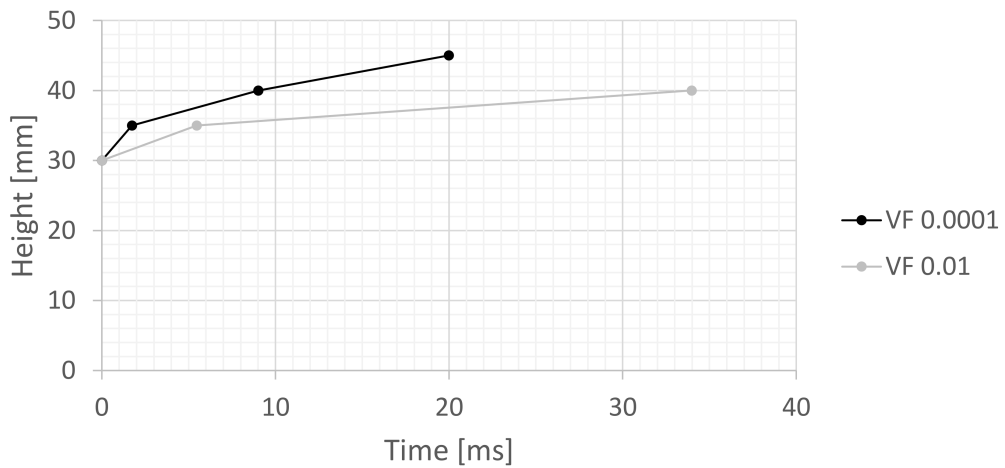

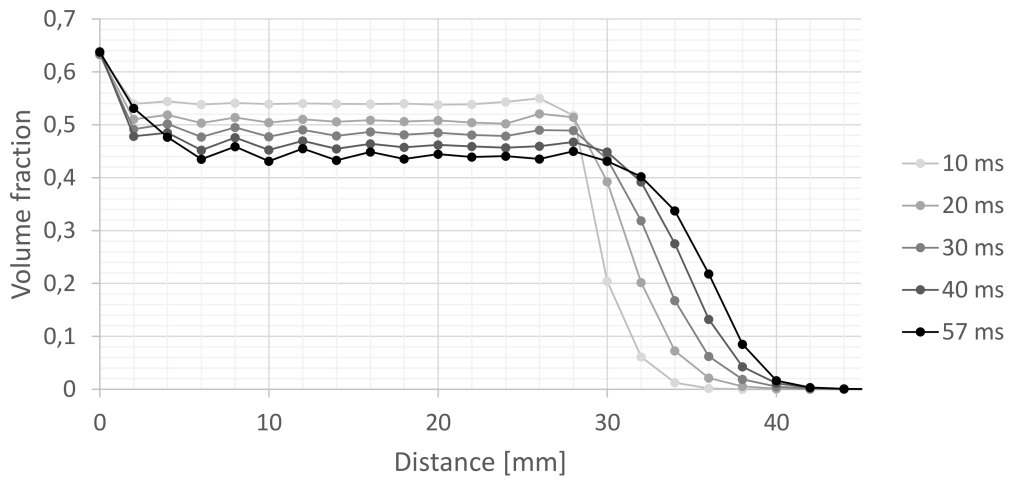**Figure 69:** Dust lifting height above initial dust bed as a function of time for simulation 11.
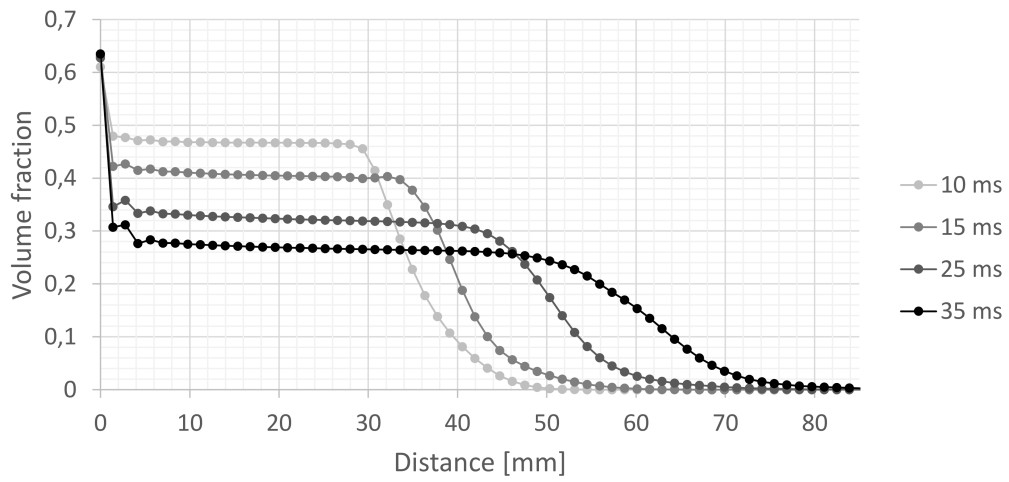
Figure 70: Volume fraction as a function of distance through the pressure chamber at different times for simulation 11.
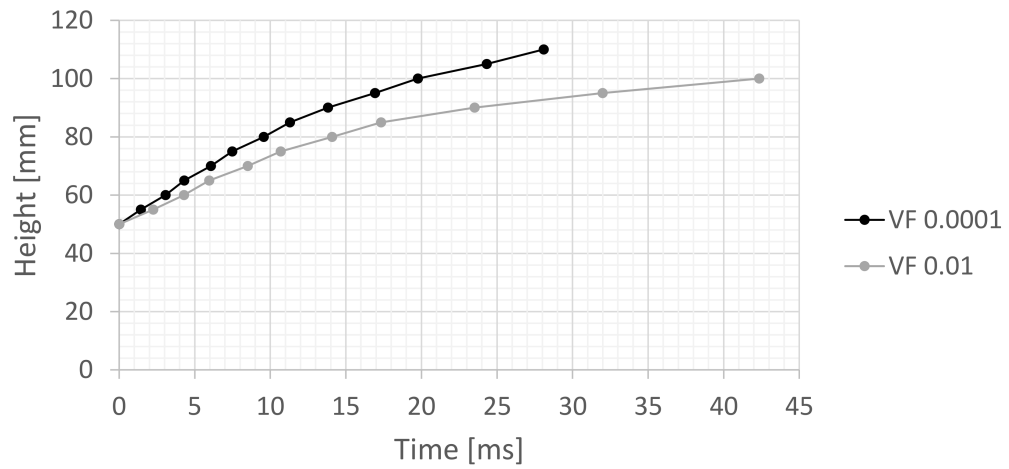
Figure 71: Dust lifting height above initial dust bed as a function of time for simulation 12.
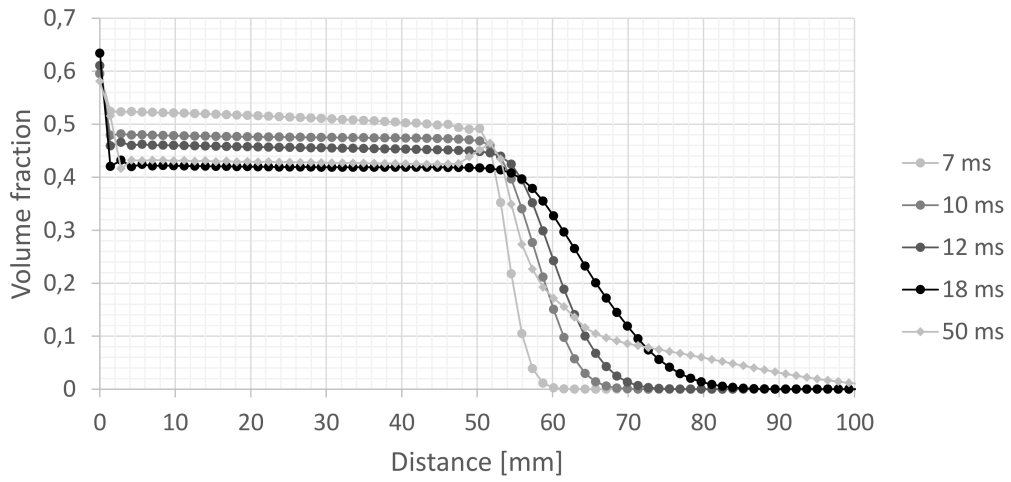
Figure 72: Volume fraction as a function of distance through the pressure chamber at different times for simulation 12.
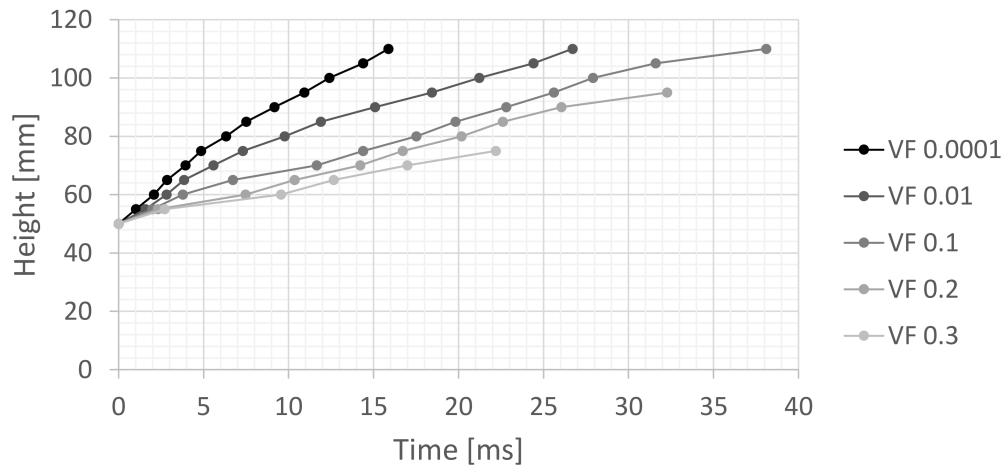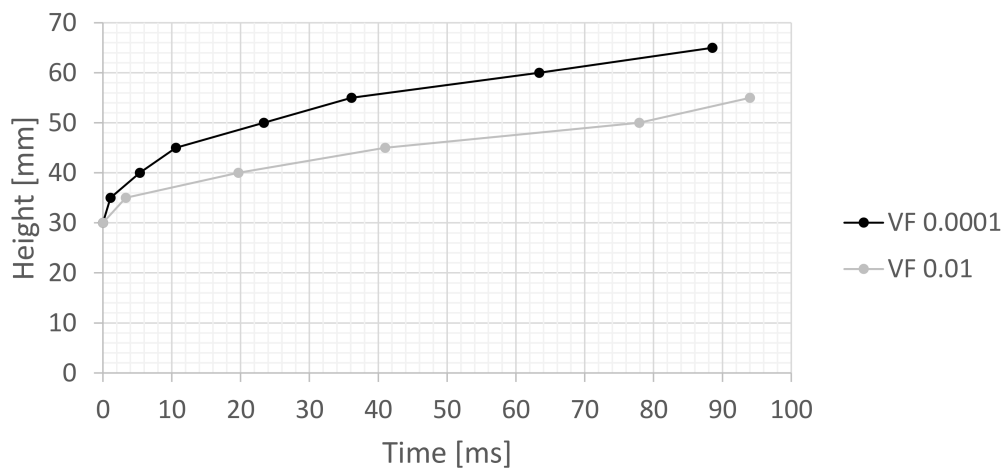

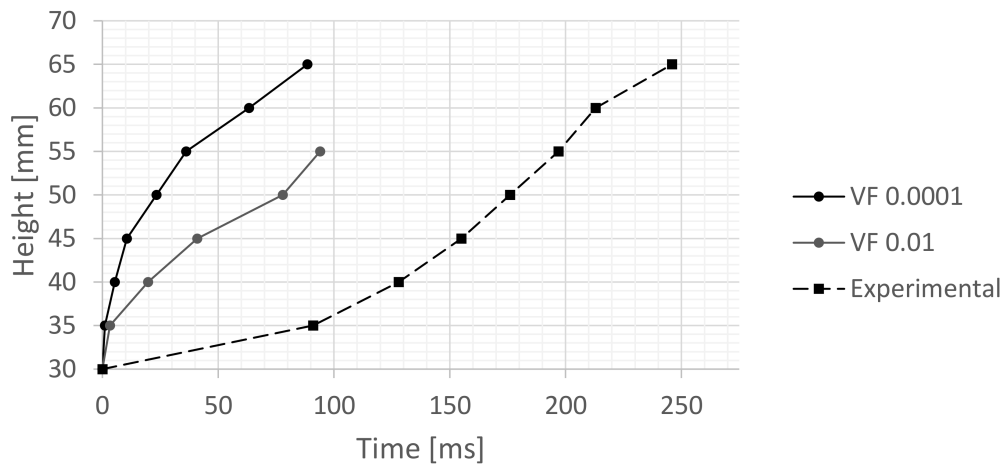**Figure 73:** Dust lifting height above initial dust bed as a function of time for simulation 13.
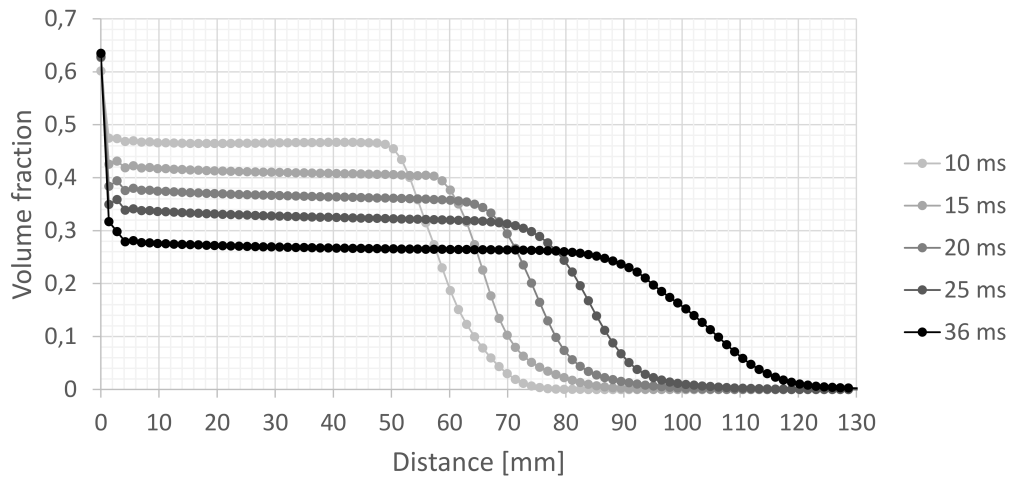
Figure 74: Volume fraction as a function of distance through the pressure chamber at different times for simulation 13.

Figure 75: Dust lifting height above initial dust bed as a function of time for simulation 14.
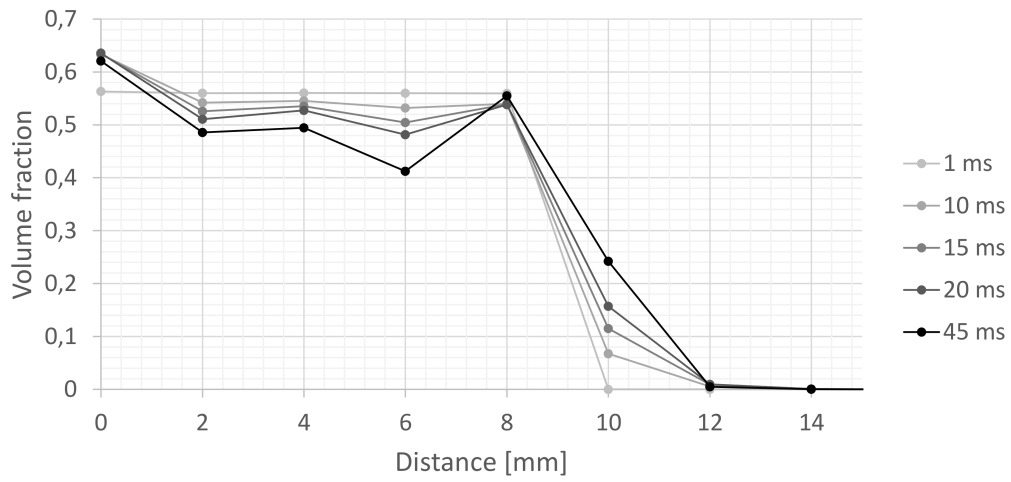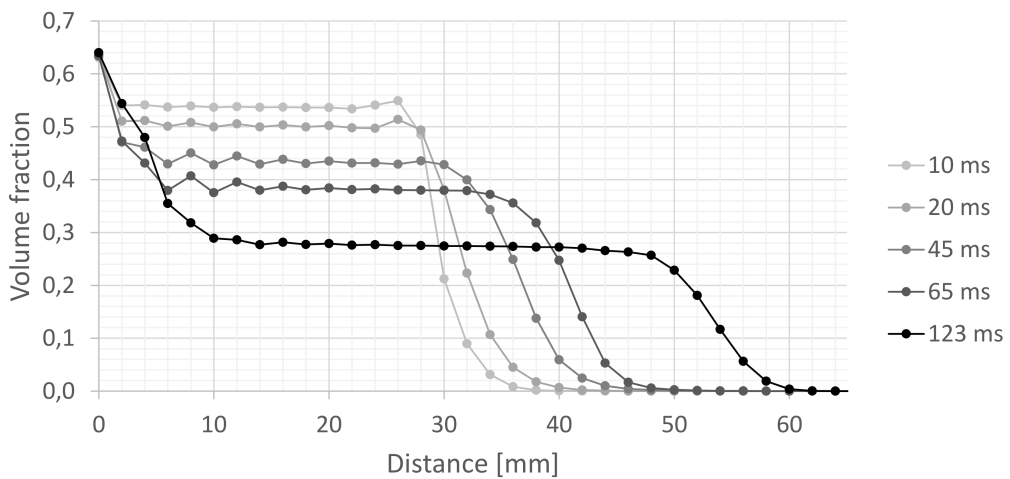
Figure 76: Volume fraction as a function of distance through the pressure chamber at different times for simulation 14.

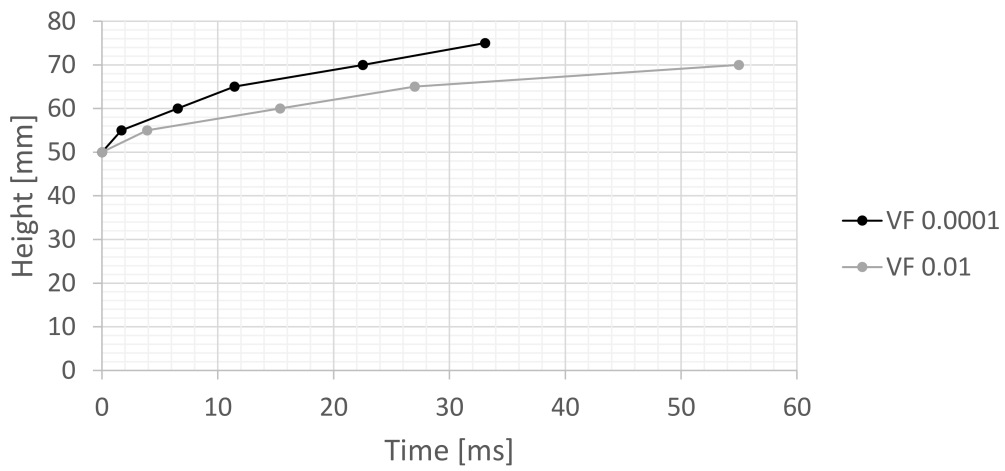**Figure 77:** Dust lifting height above initial dust bed as a function of time for simulation 15.

Figure 78: Volume fraction as a function of distance through the pressure chamber at different times for simulation 15.

Figure 79: Dust lifting height above initial dust bed as a function of time for simulation 16.

Figure 80: Volume fraction as a function of distance through the pressure chamber at different times for simulation 16.

Figure 81: Dust lifting height above initial dust bed as a function of time for simulation 17.
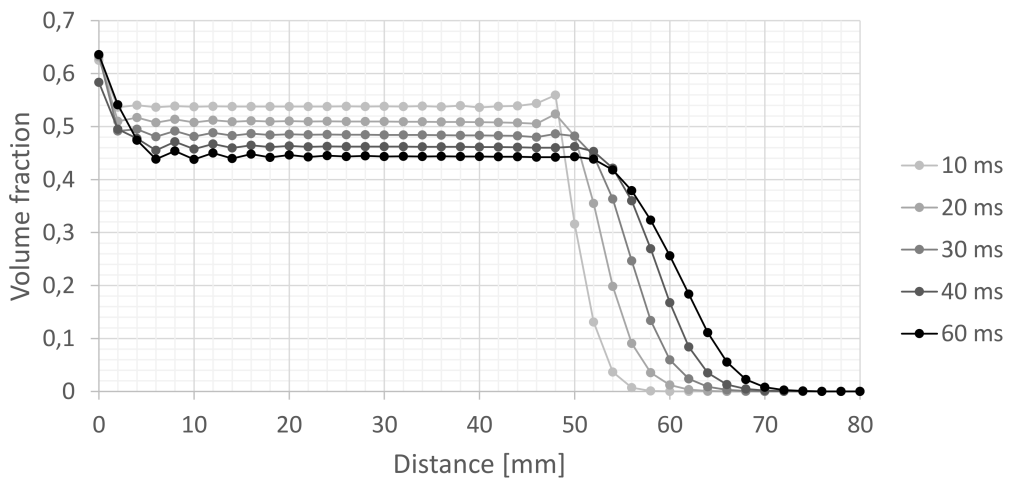
Figure 82: Height as a function of pressure for simulation 17 compared with experiment.

Figure 83: Volume fraction as a function of distance through the pressure chamber at different times for simulation 17.

Figure 84: Dust lifting height above initial dust bed as a function of time for simulation 18.

Figure 85: Volume fraction as a function of distance through the pressure chamber at different times for simulation 180.
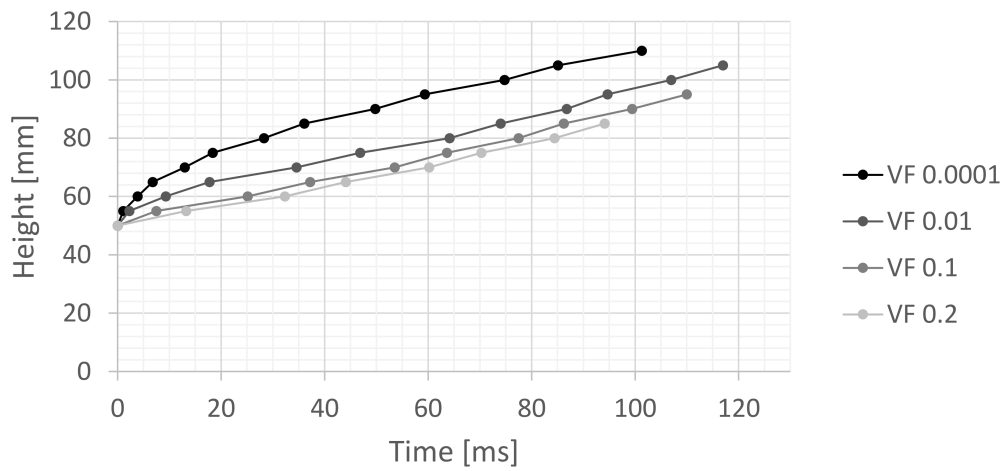
Figure 86: Dust lifting height above initial dust bed as a function of time for simulation 19.
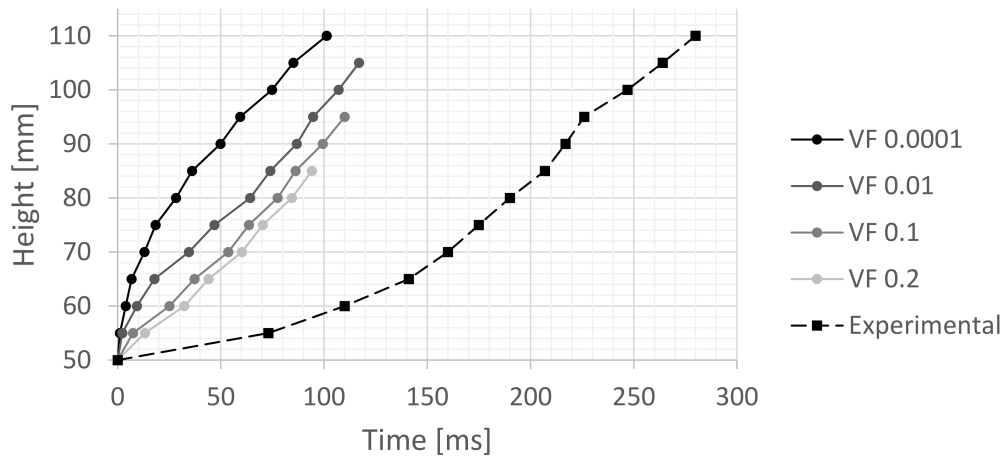

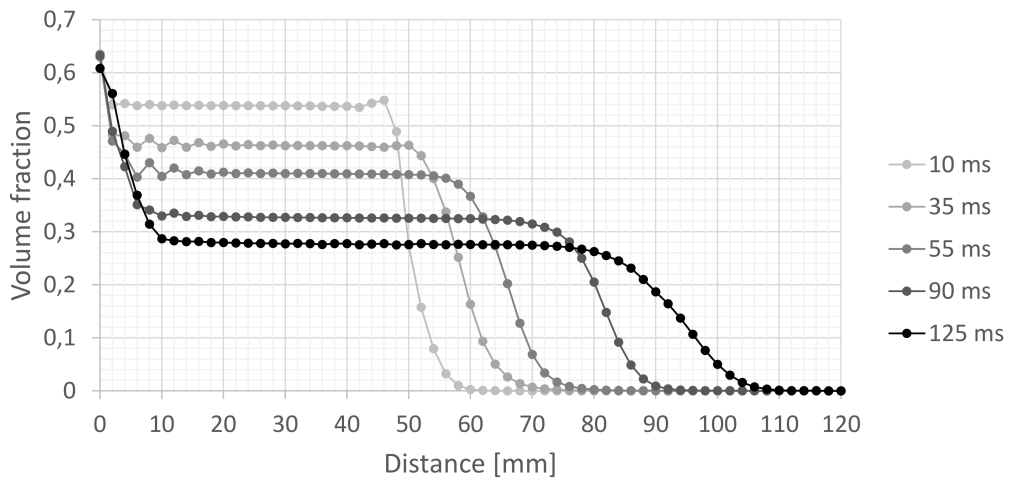**Figure 87:** Height as a function of pressure for simulation 19 compared with experiment.

Figure 88: Volume fraction as a function of distance through the pressure chamber at different times for simulation 19.